TEMPORAL AND LONGITUDINAL CLIMATOLOGICAL STUDIES OF THE EQUATORIAL IONIZATION ANOMALY AS OBSERVED BY GROUND-BASED GNSS RECEIVER NETWORKS OVER SOUTH AMERICA

Solomon Otoo Lomotey

Doctorate Thesis of the Graduate Course in Space Geophysics, guided by Drs. Jonas Rodrigues de Souza, and Cristiano Max Wrasse, approved in July 23, 2021.

URL of the original document:
<http://urlib.net/8JMKD3MGP3W34T/454URAL>

INPE

São José dos Campos

2021

TEMPORAL AND LONGITUDINAL CLIMATOLOGICAL STUDIES OF THE EQUATORIAL IONIZATION ANOMALY AS OBSERVED BY GROUND-BASED GNSS RECEIVER NETWORKS OVER SOUTH AMERICA

Solomon Otoo Lomotey

Doctorate Thesis of the Graduate Course in Space Geophysics, guided by Drs. Jonas Rodrigues de Souza, and Cristiano Max Wrasse, approved in July 23, 2021.

URL of the original document:
<http://urlib.net/8JMKD3MGP3W34T/454URAL>

INPE

São José dos Campos

2021

INSTITUTO NACIONAL DE PESQUISAS ESPACIAIS

AVALIAÇÃO DE BANCA FINAL

DEFESA FINAL DE TESE DE SOLOMON OTOO LOMOTEY
BANCA Nº 193/2021 REG 142603/2017

No dia 23 de julho de 2021, as 14h, por teleconferência, o(a) aluno(a) mencionado(a) acima defendeu seu trabalho final (apresentação oral seguida de arguição) perante uma Banca Examinadora, cujos membros estão listados abaixo. O(A) aluno(a) foi APROVADO(A) pela Banca Examinadora, por unanimidade, em cumprimento ao requisito exigido para obtenção do Título de Doutor em Geofísica Espacial. O trabalho precisa da incorporação das correções sugeridas pela Banca Examinadora e revisão final pelo(s) orientador(es).

Título: "Temporal and longitudinal climatological studies of the Equatorial Ionization Anomaly as observed by ground-based GNSS receiver networks over South America"

Dra. Inez Staciarini Batista - **Presidente** - INPE

Dr. Jonas Rodrigues de Souza - Orientador - INPE

Dr. Cristiano Max Wrasse - Orientador - INPE

Dr. Hisao Takahahsi – Membro INPE

Dr. Severino Luiz Guimarães Dutra - Membro– INPE

Dr. Babatunde Rabiu - Membro Externo (NASRDA)

Dr. Igo Paulino da Silva - Membro Externo - Membro Externo (UFCG)

Referência: Processo nº 01340.004801/2021-99   SEI nº 7974796

"If any of you lack wisdom, let him ask of God, that giveth to all men liberally, and upbraideth not; and it shall be given him'.

JAMES 1:5

*This thesis is dedicated to my parents, **James Kwaku Lomotey** and **Diana Ayivi**, and my love **Lidiane Trajano de Souza Lomotey***

ACKNOWLEDGEMENTS

ABSTRACT

In this research, maps of Total Electron Content (TEC) over the southern American continent have been used to carry out temporal and longitudinal climatological studies of Equatorial Ionization Anomaly (EIA). The EIA morphologies and evolutions were mapped using TEC at a resolution of 10 minutes. Their characteristics were investigated between 2014 and 2019 at different South American magnetic meridians separated by a distance of 555.0 km at an altitude of 300.0 km. The goal of this research was to investigate the EIA day-to-day, monthly-to-month, and annual variations at evenly spaced longitudinal sectors. A physics-based numerical model, Sheffield University Plasmasphere-Ionosphere model at Instituto Nacional de Pesquisas Espaciais (SUPIM-INPE), was used to study the factors responsible for the evolution of an asymmetry in equatorial TEC anomalies during the daytime. We find that the configuration parameters such as strength, shape, intensity, and latitudinal positions of the EIAs are affected by the eastward electric field (SCHERLIESS; FEJER, 1999) and effective meridional wind (HEDIN et al., 1996). The monthly variations in the EIA over the various magnetic meridian sectors demonstrate a semiannual variation. The EIA crests look more symmetric in equinox than in solstice seasons. The asymmetries of the EIA observed during the December solstice are intense than during the June solstice, whereas September equinox is less symmetric than March equinox seasons. Importantly, this study indicates that the vertical drift and the meridional neutral wind plays a very significant role in the development of the EIA asymmetry by transporting the plasma up the field lines. Aside from that, from February to April at most magnetic meridian sectors, the latitudinal distribution of TEC can be seen above the geographic equator. We suggest that the latitudinal distribution is due to the different motions caused by a wind dynamo. There was a notable contraction of the EIA southern hemispheric (SH) crests from the December solstice to the June solstice. Meanwhile, the EIA crest positions in the northern hemisphere (NH) expand from the December solstice to the June solstice. The intensities of the EIA crests decreased significantly with solar descending phases (i.e., 2014-2019), according to our observations at all sectors. At each magnetic meridian sector, we also found some evidence of packets of oscillations with periods ranging from 2 to 16 days in the SH crest positions. Interestingly, an oscillation with 3-4 days was noticed from July 19 to July 31 in 2014. Simultaneous measurements of thermospheric wind and maximum ionization height of the F layer (hmF2) from Fabry-Perot Interferometer (FPI) and digisonde installed at Cajazeiras (3.8°S, 38.6°W, dip angle: 11°S) and São Luís (2.33°S, 44.2°W, dip angle: 2.7°S), respectively, were investigated and revealed the same oscillation with a period of 3-4 days. These findings show that the 3-4 day oscillation is an Ultra-Fast Kelvin wave, and that its presence could alter the electric via the E region dynamo, altering the vertical height and horizontal distribution of electron densities via $\vec{E} \times \vec{B}$ drift.

Keywords: Equatorial and Low-latitude ionosphere. Equatorial ionization Anomaly (EIA). SUPIM-INPE model. Total Electronic Content (TEC). Spectral Analysis. Ultra-Fast Kelvin wave.

ANOMALIA EQUATORIAL DE IONIZAÇÃO EM TERMOS DE SUA VARIAÇÃO TEMPORAL E LONGITUDINAL SOBRE A AMÉRICA DO SUL

RESUMO

Nesta pesquisa, mapas de Conteúdo Eletrônico Total (TEC) sobre o continente sul-americano foram usados para realizar estudos climatológicos temporais e longitudinais de Anomalia de Ionização Equatorial (EIA). As morfologias e evolução do EIA foram mapeadas usando TEC a uma resolução de 10 minutos. Suas características foram investigadas entre 2014 e 2019 em diferentes meridianos magnéticos da América do Sul separados por uma distância de $555,0$ km a uma altitude de $300,0$ km. O objetivo desta pesquisa foi investigar as variaçãoes diárias, mensais e anuais do EIA em setores longitudinais uniformemente espaçados. Um modelo numérico baseado na física, modelo Plasmasfera-ionosfera da Sheffield University no Instituto Nacional de Pesquisas Espaciais (SUPIM-INPE) foi utilizado para estudar os fatores responsáveis pela evolução de uma assimetria nas anomalias do TEC equatorial durante o dia. Descobrimos que os parâmetros de configuração, como força, forma, intensidade e posições latitudinais dos EIAs são afetados pelo campo elétrico para o leste (SCHERLIESS; FEJER, 1999) e vento meridional efetivo (HEDIN et al., 1996). As variações mensais no EIA ao longó dos vários setores do meridiano magnético demonstram uma variação semestral. As cristas EIA parecem mais simétricas no equinócio do que nas estações do solstício. As assimetrias do EIA observadas durante o solstício de dezembro são mais intensas do que durante o solstício de junho, enquanto o equinócio de setembro é menos simétrico do que as estações do equinócio de março. É importante ressaltar que este estudo indica que a deriva vertical e o vento neutro meridional (HEDIN et al., 1996) desempenham um papel muito significativo no desenvolvimento da assimetria EIA, transportando o plasma pelas linhas de campo. Além disso, de fevereiro a abril, na maioria dos setores dos meridianos magnéticos, a distribuição latitudinal da TEC pode ser observada acima do equador geográfico. Sugerimos que a distribuição latitudinal se deve aos diferentes movimentos causados por um dínamo do vento. Houve uma contração notável das cristas hemisféricas sul (HS) da EIA do solstício de dezembro ao solstício de junho. Enquanto isso, as posições da crista EIA no hemisfério norte (HN) se expandem do solstício de dezembro ao solstício de junho. As intensidades das cristas EIA diminuíram significativamente com as fases de descida solar (ou seja, 2014-2019), de acordo com nossas observações em todos os setores. Em cada setor do meridiano magnético, também encontramos algumas evidências de pacotes de oscilações com períodos variando de 2 a 16 dias nas posições de crista no HS. Curiosamente, uma oscilação com 3-4 dias foi observada de julho 19 a julho 31 em 2014. Medições simultâneas de vento termosférico e altura máxima de ionização da camada F (hmF2) do interferômetro Fabry-Perot (FPI) e digisonda instalado em Cajazeiras (3.8°S, 38.6°W, ângulo dip: 11°S) e São Luí s ($2,33°$ S, $44,2°$ W, ângulo dip: $2,7°$ S), respectivamente, foram investigados e revelou a mesma oscilação com um período de 3-4 dias. Essas descobertas mostram que a oscilação de 3-4 por dia é uma onda Kelvin ultra rápida e que sua presença pode alterar a eletricidade por

meio do dínamo da região E, alterando a altura vertical e a distribuição horizontal das densidades de elétrons via $\vec{E} \times \vec{B}$ drift.

LIST OF FIGURES

xviii

LIST OF TABLES

CONTENTS

xxiii

1 INTRODUCTION

There is an eastward electric field and a northward magnetic field during the day in the equatorial ionosphere. The combination of these two fields transports plasma from the geomagnetic equator upward via $\vec{E} \times \vec{B}$ convection. The plasma, then, diffuses along the magnetic field lines due to the Earth's pressure gradient and gravitational forces down to higher latitudes (DUNCAN, 1960; STENING, 1992), where the plasma piles up and forms two crests at about $\pm 20°$ at the magnetic dip equator. This process is usually termed as the equatorial ionization anomaly (EIA) or simply "fountain effect" (APPLETON, 1946; MARTYN, 1947; KELLEY, 2012).

The EIA produced is widely known to have a regular behaviour (CHEN, 1992): it becomes stronger gradually after it appears in the morning, then reaches its maximum in the afternoon, and sometimes disappears in the night based on geophysical conditions. Additionally, the EIA depends on various geophysical conditions, such as solar flux, local time, season, longitudes, and magnetic activity (KIKUCHI et al., 2000; BALAN et al., 2018).

The ionosphere's electrodynamics in equatorial and low-latitude regions undergo sudden changes just before and after sunset, resulting in significant ionospheric phenomena. Among others, the EIA can be considered the most significant feature of the equatorial ionosphere.

The EIA's spatial and temporal variability has been increasingly recognized by the scientific community (BALAN et al., 2018). However, the morphology and mechanism that cause the EIA's day-to-day variability are still not well understood. This is of great interest to the scientific community to predict many ionospheric processes and improve regional ionospheric models at low latitudes (NAMGALADZE et al., 1991; SU et al., 1995; SCHUNK et al., 2005).

Since the EIA was discovered by Appleton in 1946, it has been studied by analysis of Total Electronic Content (TEC) obtained from Global Navigation Satellite System (GNSS) signals (RAY et al., 2006; CHEN et al., 2008; NOGUEIRA et al., 2013; GONCHARENKO et al., 2013; TAKAHASHI et al., 2014a; VENKATESH et al., 2015; BO-LAJI et al., 2017; MUNGUFENI et al., 2018), numerical simulations models (HANSON; MOFFETT, 1966; BALAN et al., 1996; BAILEY et al., 1997; SOUZA et al., 2003; BATISTA; ABDU, 2004; ANDERSON, 1973; ANDERSON et al., 2002) and ionosondes (WALKER, 1981; ABDU et al., 1983; ABDU et al., 1991a; JAYACHANDRAN et al., 1997; FAGUNDES et al., 2005). These studies have given considerable knowledge about the EIA mor-

phology in different seasons, longitudes, and solar activity periods. However, the relatively small changes in time and space of the EIA remain unresolved and, consequently, not fully understood. Globally, the EIA structure has been extensively studied at different longitudinal sectors based on various geophysical conditions at different altitudes and local times (SAGAWA et al., 2005; BAGIYA et al., 2009; TAKAHASHI et al., 2014a).

In the Asian sector, the morphology of EIA can be traced back to the work of Golton e Walker (1971), based on the recording of the Faraday rotational of signals from the geostationary satellite. Since then, subsequent studies have been performed to investigate EIA evolution structure related to the local time and season under different solar activity phases in reviews (WALKER, 1981; KUMAR; SINGH, 2009; ZHAO et al., 2009).

Zhao et al. (2009) investigated the characteristics of the TEC in the EIA region, and they found out that semiannual variations mainly control the EIA morphology. They also identified that the EIA's northern crest broadened during equinox while the southern crest is constrained all along June-August. On the other hand, solar activity dependency was higher in the crest region than in the EIA's trough.

Watthanasangmechai et al. (2015) studied the temporal variation of EIA asymmetry at stations close and outside the geomagnetic equator during magnetic storm days. An intensive electric field empowered by the neutral wind led to the EIA's asymmetry nature and had no strong interrelationship with the geomagnetic storm. However, they used few data, and the source of variation of EIA was not quantified. Mo e Zhang (2020a) recently reported the EIA's modulation during the Sudden Stratospheric Warming (SSW). The EIA's northern and southern crests were modulated by quasi-10 day periodic wave oscillation. However, their result did not show any strong correlation to solar and magnetic activities.

In African Sector, Bolaji et al. (2017) investigated the morphology of the EIA using GPS TEC and ground-based magnetometer data during quiet geomagnetic periods. According to them, the EIA crests had different structures compared to other sectors. The north crests have a greater magnitude of intensity (TEC level) than the south crests. During the early hours, the equatorial electrojet (EEJ) current and the EIA's hemispheric extent showed a weak correlation. However, the mechanisms surrounding the transport parameters resulting in the EIA's behavioural structure were not studied.

Oluwadare et al. (2019) recently studied the TEC characteristics over EIA regions during quiet geomagnetic conditions. From their observations, TEC's high and low values were registered during equinoctial months and June solstice, respectively. In addition, their estimated TEC values increase or decrease with solar activity. Nevertheless, their observations used just a few ground stations over the equatorial and low latitude regions. The EIA's responses by geomagnetic storm day on November, 13, 2012 were investigated by Joseph et al. (2015). Their observations revealed enhancement of TEC's during the recovery phase of the storm 4 days after the event. Furthermore, the EIA crests and latitudinal extent intensified, which was attributable to increasing electric fields caused by ionospheric dynamo disturbances. However, the ionospheric dynamo disturbance extent that led to the EIA intensification was not evaluated.

In the equatorial and low latitudes of South America, few studies have been reported concerning the longitudinal variation of the EIA using various observational techniques. Nogueira et al. (2011) investigated the magnitude of the EIA under a major geomagnetic storm situation using TEC and the critical layer frequency (F_2) from digisondes, at two stations, one at the geomagnetic dip equator and the other at the low-latitude region. They realized significant variations in the early morning development of the EIA and local time. These variations were attributed to prompt penetration of electric fields. Takahashi et al. (2014a) studied daytime EIA at the magnetic equator and crest regions using GPS TEC map at a fixed local time (15:00 LT). Their results revealed semiannual changes, with March-April and October-November having maximum TEC and a steady decrease throughout the year. The maximum TEC at the trough and south crest region showed some long and short periodic oscillations and presented strong correlations with solar activity at the magnetic equator. They also attributed the day-to-day variations of the EIA to the solar flux dependency and local dynamical effects such as planetary-scale wave oscillations (their study considered some fixed positions and time).

Takahashi et al. (2016) used TEC maps to analyze the temporal and spatial variation of EIA. Their findings demonstrated a high TEC spatial gradient from trough to crest, which could result in a large ionospheric range delay in the Global Navigation Satellite System (GNSS) and have an impact on ionospheric space weather forecasting (SAGAWA et al., 2005; AKALA et al., 2012). Recently, Dias et al. (2020) investigated day-to-day and month-to-month characteristics of the EIA in 3 closely spaced longitudinal sectors during the year 2016 in the descending phase of the solar activity using GPS TEC. EIA showed a semiannual variation in all sectors,

according to the authors, with a main maximum in the summer, a minimum in the winter, and a secondary maximum in the spring. The EIA also showed a structural behaviour with a trough around the magnetic equator and crests at low latitudes.

Furthermore, the EIA crests shape, strength, extent, and lifetimes showed a significant variation between the three sectors during different seasons. However, the studies considered just a year of data. The dynamics responsible for the semiannual variation of the EIA crests at those sectors were not discussed.

1.1 Motivation of the research

The Southern American sector is well known for its high variability of electrodynamics processes, particularly prominent in the equatorial and low latitude regions. In addition, the magnetic field lines in the Brazilian region have the highest declination, and the gradient between the anomaly trough and the crest is extremely steep (JONAH et al., 2015). It causes enormous latitudinal and longitudinal changes in the equatorial/low-latitude ionosphere, which are what define the EIA and other ionospheric irregularities (JONAH et al., 2015; DASGUPTA et al., 2007). This has been a topic in space weather study for decades since it is a critical feature of ionospheric variability and has significant consequences on navigation, communication, and ionospheric forecasting systems, all of which are not well understood (EASTES et al., 2019).

On the other hand, the need to anticipate the study of day-to-day variation of the EIA crests is vital for ionospheric modeling predictions and to improve the applications using mainly GNSS systems.

The equatorial electrodynamics processes control the equatorial ionization anomaly variability (YEH et al., 2001; HEELIS, 2004; KELLEY, 2012). Another school of thought suggests that the EIA's morphology, based on the magnitude of the crests, crest-trough positions, interhemispheric asymmetry, and the time of occurrences, varies with several geophysical conditions (ABDU et al., 1991a; GU et al., 2018; BALAN et al., 2018).

Besides, the coupling between thermosphere and ionosphere systems is well-known to be driven by upward propagating wave oscillations which causes changes in the ionospheric parameters (FORBES; LEVERONI, 1992; ABDU et al., 1995; ZOU et al., 2000; FAGUNDES et al., 2005; CHEN et al., 2008; TAKAHASHI, 2012; GAN et al., 2016; YAMAZAKI et al., 2018; MO; ZHANG, 2020a). These changes lead to variations of the

ionospheric dynamo processes in the E and F regions responsible for forming the EIA.

However, EIA's variation features may differ in different sectors, and the relative importance of the factors mentioned above is still not thoroughly understood. Moreover, over the Brazilian sector, the latitudinal and longitudinal extent of the EIA crests its magnitudes and dynamics (for example, effects due to tides and planetary waves) that might influence the day-to-day variation are still not well known.

Therefore, the current study will use TEC map data from South America and simulations from the SUPIM-INPE model to investigate daytime temporal, morphology, dynamics, and longitudinal change of the Equatorial Ionization Anomaly.

1.1.1 Objectives of the research

The main objective of this work is to investigate the temporal, longitudinal and latitudinal variability of the EIA crest, using TEC data from ground-based GNSS receivers. To accomplish the research goal, the following specific objectives were set:

a) To characterize the EIA morphology along the South America magnetic meridians.

b) To investigate spatial, seasonal and solar activity dependences of the EIA.

1.1.2 Thesis structure

The structure of the thesis is presented as follows:

The Earth's ionosphere, as well as the equatorial electrodynamic processes and ionospheric dynamic processes that lead to the formation of the EIA, are discussed in Chapter 2, as well as a global review of the EIA.

Chapter 3 describes the methodology, detailed information concerning the construction TEC maps in geographic longitude and latitude coordinates from GNSS receivers, transformation of geographic longitudes to geomagnetic longitudes using the International Geomagnetic Reference Field (IGRF) model, the algorithm for estimation of the EIA parameters and also the spectral analysis procedures employed in the EIA crest position.

Chapter 4 presents the results for the diurnal, seasonal and annual variations of the morphology of the EIA crests based on different magnetic longitudes. Additionally,

5

a monthly analysis of the southern hemispheric EIA crest positions and observed oscillations, analyzed using spectral analysis, will be elaborated.

Chapter 5 presents the physical interpretations and discussion of the result provided in Chapter 4. Firstly, the characteristics of the diurnal variation of anomaly development will be discussed with comparison to SUPIM-INPE model. The monthly EIA crests variations will be discussed and compared to previous works done over the Southern American, African and Asian sectors. The possible dynamic that might be responsible for the Southern hemispheric crest positions will be discussed and compared to recent works. The variations of the observed EIA crest intensities (TEC level) with the solar cycle phases will be explained.

Chapter 6 will present the conclusion of this current work based on our findings and considerations for future works.

2 THE EARTH IONOSPHERE AND THE REVIEW OF EQUATORIAL IONIZATION ANOMALY (EIA)

This chapter discusses the Earth's ionosphere, including its formation, a brief mathematical description, and the equatorial electrodynamics that leads to the EIA formation. Furthermore, an EIA global review is presented.

2.1 Structure and formation of the Ionosphere

The Earth's ionosphere is a partially ionized gas surrounding the planet and acts as an interface between space and the atmosphere. This area is electrically conductive and can support strong electric currents. It is often found between 60 and 1000 km altitude and is characterized by a significant number of free electrons and positive ions (density $\sim 10^3 - \sim 10^6$ cm^{-3}) (KELLEY, 2012).

It is a region of great interest in telecommunications because it is the means of transmission and propagation of radio waves (RATCLIFFE et al., 1972). Besides, its dynamic behavior and physical-chemical properties provide essential information about phenomena related to the Sun-Earth system's interaction with substantial Space Weather implications.

The ionosphere formation is essentially governed by solar radiation's action on atmospheric constituents (TAYLOR, 1903) through some processes such as photoionization and recombination. High energy particles can also penetrate the atmosphere promoting ionization of its constituents, although this process is typical of regions with high magnetic latitudes.

Atmospheric density decreases with increasing altitude, while the intensity of extreme ultraviolet (EUV) radiation from the sun decreases with decreasing altitude due to the partial absorption of radiation by atmospheric constituents. These factors promote the formation of a region where the ionization rate is maximum at a certain altitude, decreasing above and below it. Chapman developed a theory in 1931, which predicts this ionospheric region's formation, as shown in Figure 2.1.

Figure 2.1 - Illustration of the production of ionization in the atmosphere, showing the interaction of solar radiation with atmospheric gases, whose density decreases exponentially with altitude, giving rise to the Chapman layer.
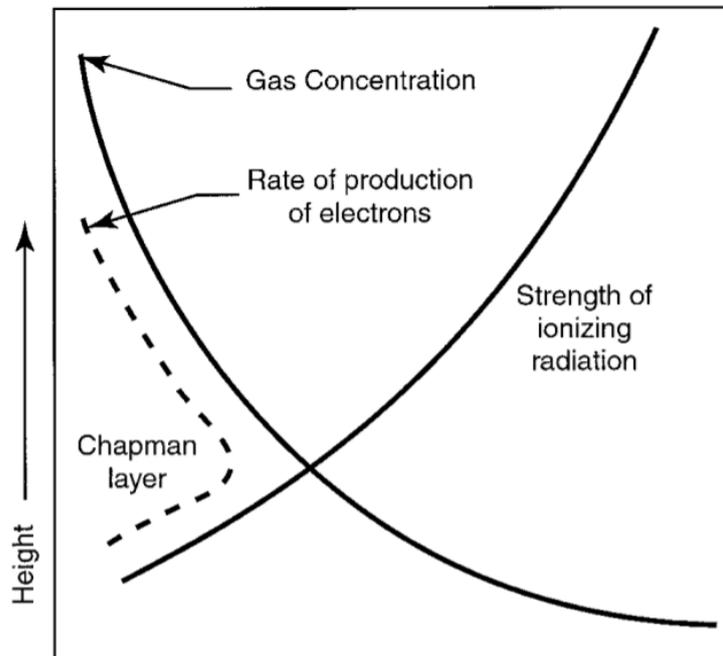
Source: Goodman (2001).

Experimental observations with sounding instruments based on the transmission and reception of radio waves showed the nature and structure of the ionospheric layers, historically called regions D, E, F_1 and F_2. The occurrence of a diurnal F_3 layer, between 450 and 600 km in altitude, has already been reported by Balan et al. (1997). The explanation for the formation in ionospheric layers is due to the following factors:

a) the fact that the intensity of solar radiation is not constant at all wavelengths, and may be more intense at a particular wavelength, and

b) the composition of the neutral atmosphere is highly varied, containing atoms and molecules such as oxygen, nitrogen, nitric oxide, which can be photoionized by radiation of different wavelengths.

The description of the different ionospheric regions is made based on the electronic density profile as a function of altitude, as illustrated in Figure 2.2. The different ionospheric layers have peculiar characteristics. Region D is the lower region of the

ionosphere between 70 and 90 km. Its formation occurs due to the incidence of solar X-rays and ultraviolet radiation that ionize gases such as O_2, N_2, and NO.

It is characterized by the presence of positive and negative ions, agglomerated ions, and electrons. At the upper limit, molecular ions such as NO^+ and O_2^+ predominate, and with also O^+ ions, albeit in lesser quantity (HARGREAVES, 1992).

Figure 2.2 - Typical profile of the ionospheric plasma density showing various layers and constituents.
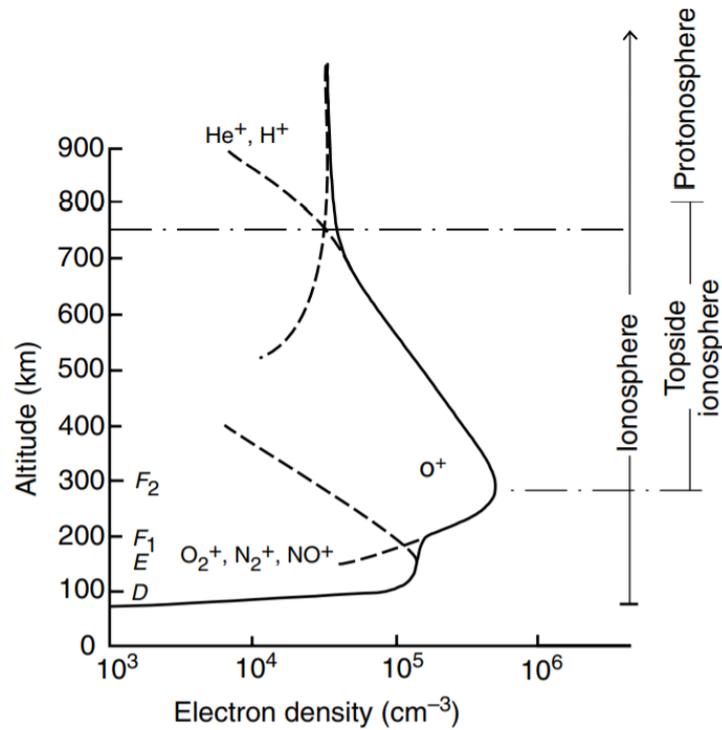
Source: Schunk e Nagy (2009).

In region E, above 90 km, chemical reactions are not so complex, with NO^+ and O_2^+ being the major ions constituents. The maximum electronic density ($< 10^6$ cm^{-3}) is related to the proportion between NO^+ and O_2^+, with the predominance of NO^+ at altitudes close to 130 km. The total ionic density is of the order of 10^5 cm^{-3}, while the neutral density is greater than 10^{11} cm^{-3}.

Eventually, significant increases in ionization of the E region are observed (approximately an order of magnitude greater than the usual density) at altitudes between 90 and 130 km. This layer occurs sporadically and is, therefore, termed the E-Sporadic layer and can be observed in all latitudes (KOPP, 1997; HALDOUPIS, 2011).

The F_1 region is the lower part of the F region, where photochemical processes predominate, and the major element is the atomic oxygen ion, O^+. Important reactions are the photoionization of atomic oxygen and loss processes in reactions with N_2 and O_2. During the night, when the photoionization process does not exist, the F_1 region disappears.

The F_2 region is characterized by the importance of the processes of transport such as diffusion and drifts along field lines (induced by neutral winds) and in the direction perpendicular to them ($\vec{E} \times \vec{B}$). The ionic density of the F_2 region is ten times greater than the E region. The neutral density is one hundred times greater than the ionic one, so that the plasma is partially ionized. The upper region of the ionosphere, where diffusive processes dominate, is termed the upper ionosphere.

2.2 Mathematical description of the Ionosphere

Physical-chemical processes influence the dynamics that determine the ionic distribution profile. These mechanisms are responsible for the generation and loss of ionization as well as the transport of ionospheric plasma in perpendicular and parallel directions to the geomagnetic field. Like any other gas, ionospheric plasma is subject to gravitational and collisional forces, but it also suffers electric and magnetic forces because it is ionized.

Due to these forces, separate equations of motion for ions and electrons can be constructed. The continuity equation expresses the influence of several processes that alter electronic concentration distribution, such as physical-chemical and transport processes.

In this present work, a full mathematical representation to calculate the main ionospheric parameters is shown in the Subsection 3.4, as described by the Sheffield University Plasmasphere-Ionosphere Model at INPE (BAILEY; BALAN, 1996; SOUZA, 1997; SEPULVEDA, 2015).

2.3 Electrodynamics of equatorial and low latitude Ionosphere

The electric field ($\vec{E}$), plasma drifts, and the neutral winds are important because they provide the necessary physical conditions to understand the equatorial ionosphere's electrodynamics. The combination of electric fields and the geomagnetic field ($\vec{B}$) are the main factors needed for the initiation of the ionospheric drifts.

To understand how these fields are generated, leading to the drifts of the ions, a brief

review will be done on the electrical conductivities, ionospheric dynamo processes, and the equatorial ionization anomaly formation.

2.3.1 Conductivity of the Ionosphere

The ionospheric conductivity depends directly on the electronic density and the relative magnitudes between the collision frequency and the frequency of rotation of the charged particles (ions and electrons) around the magnetic field. Due to the presence of the Earth's magnetic field, the ionosphere becomes an anisotropic medium.

Thus, the electrical conductivity in the ionosphere can be obtained as a function of three components due to the presence of simultaneous magnetic and electric fields. Usually, the ionospheric conductivity is presented in a 3-direction format: along the magnetic field vector ($\vec{B}$ direction); along the electric field vector component perpendicular to the magnetic field ($E_\perp$); and simultaneously perpendicular to both ($\vec{E} \times \vec{B}$ direction) (RISHBETH; GARRIOTT, 1969; HARGREAVES, 1992).

Equation 2.1 represents longitudinal or parallel conductivity (σ_o). This component of conductivity is parallel to the geomagnetic field vector and is given by (RISHBETH, 1997):

$$\sigma_o = ne^2 \left(\frac{1}{m_e \nu_e} + \frac{1}{m_i \nu_i} \right) \tag{2.1}$$

The Pedersen or transversal conductivity is referred to the component in the $E_\perp$ direction. This conductivity component is perpendicular to the direction of the geomagnetic field vector and parallel to the direction of the electric field vector and is given by:

$$\sigma_p = ne^2 \left(\frac{\nu_e}{m_e \left(\nu_e^2 + \Omega_e^2 \right)} + \frac{\nu_i}{m_i \left(\nu_i^2 + \Omega_i^2 \right)} \right) \tag{2.2}$$

The Hall conductivity component is orthogonal to the directions of the geomagnetic field vector and the direction of the vector electric field:

$$\sigma_H = ne^2 \left(\frac{\Omega_e}{m_e \left(\nu_e^2 + \Omega_e^2 \right)} - \frac{\Omega_i}{m_i \left(\nu_i^2 + \Omega_i^2 \right)} \right) \tag{2.3}$$

Where m_e represents the mass of the electron, m_i the average mass of the ion, $\Omega_{e,i}$

11

are the gyrofrequencies, $\nu_{e,i}$ are the collision frequencies between neutral and charged particles, e is the electron charge, and n the plasma density. The subscript e and i in the above equations represent the electron and ion terms, respectively.

In the E-region, electrons collide mainly with neutral particles, and, therefore, ν_e is taken to equal to the frequency of electron-neutral collision ν_{en}. However, in the F-region electrons also collide with ions and the electron-ion collision frequency (ν_{ei}) should be included.

Based on a simple gas kinetic theory, below is the formula for $\tilde{\sigma}$. Although this is simply a first-order approximation, it has shown to be helpful in various applications. If we adopt a cartesian coordinate system and run the x-axis along $\vec{B}_0$, we get

$$\tilde{\sigma} = \begin{bmatrix} \sigma_0 & 0 & 0 \\ 0 & \sigma_p & -\sigma_H \\ 0 & \sigma_H & \sigma_p \end{bmatrix} \tag{2.4}$$

In this expression σ_0, σ_p, σ_H are parallel, Pedersen and Hall conductivities and given as in emu. The x-axis runs horizontally southward while the z-axis runs vertically upward. Then, starting with Equation 2.4, the standard tensor transformation is applied as follows:

$$\tilde{\sigma} = \begin{bmatrix} \sigma_{xx} & \sigma_{xy} & \sigma_{xz} \\ \sigma_{yx} & \sigma_{yy} & \sigma_{yz} \\ \sigma_{zx} & \sigma_{zy} & \sigma_{zz} \end{bmatrix} \tag{2.5}$$

A general expression of the tensor elements is given elsewhere (MAEDA; KATO, 1966). If the geomagnetic coordinates are used i.e., the east-west component of $\vec{B}_0$, vanishes. The tensor form of the conductivity can be expressed in the matrix form as (MAEDA; KATO, 1966):

$$\tilde{\sigma} = \begin{pmatrix} \sigma_0 \cos^2 I + \sigma_P \sin^2 I & \sigma_H \sin I & -(\sigma_0 - \sigma_p) \sin I \cos I \\ -\sigma_H \sin I & \sigma_p & -\sigma_H \cos I \\ -(\sigma_o - \sigma_p) \sin I \cos I & \sigma_H \cos I & \sigma_P \cos^2 I + \sigma_o \sin^2 I \end{pmatrix} \tag{2.6}$$

where $\tilde{\sigma}$ represents the conductivity tensor and I represents the angle of inclination of the geomagnetic field $\vec{B}$ (positive in the northern hemisphere). Further details on

these conductivities can be found in literature (BAKER; MARTYN, 1952; RISHBETH; GARRIOTT, 1969; KELLEY, 2012). In addition, all the ionospheric conductivities vary with height.

In Figure 2.3 we can see that the Pedersen and Hall conductivities have a maximum at the heights of E region, rapidly decaying to heights below and above the maximum. This peak is around 140 km for Pedersen conductivity and 125 km for Hall conductivity at the magnetic equator.

Figure 2.3 - Conductivity profile showing the variation of longitudinal conductivities, σ_0, Pedersen (σ_p) and Hall (σ_H) with height. The dashed curve is a typical nighttime profile of σ_p.
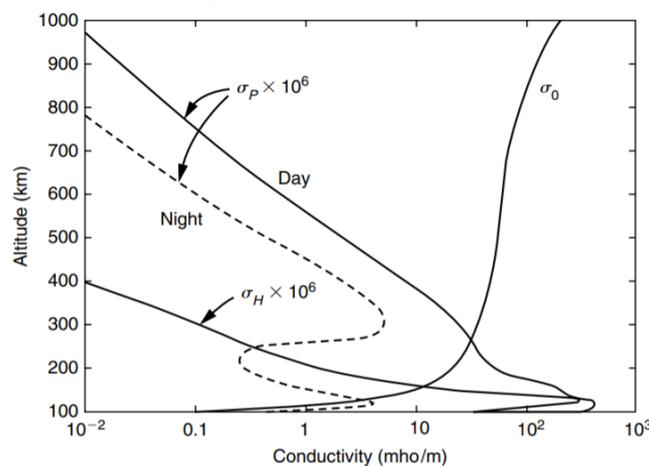
Source: Kelley (2012).

2.3.2 E-region dynamo

All components in geomagnetic records (magnetograms in regular sensitivity) occasionally show very smooth traces that indicate clear patterns of daily variations regarding local solar time. This occasion is termed a "geomagnetically quiet period," and the pattern is named "solar quiet daily variation" and is commonly shown by Sq.

The E region dynamo, commonly known as an ionospheric dynamo, is responsible for the Sq electric current system's generation mechanism. Electric fields and electric currents are described in terms of particles' movement through the neutral winds of the atmosphere.

The ionospheric dynamo usually refers to the dynamo processes at the height of

13

E region. The ionosphere is characterized by neutral wind motions driven by tidal oscillations propagating from below and in situ heating. Tidal oscillations are driven by solar radiation absorption that dominates the neutral atmosphere motions in the E-region (HEELIS, 2004). The dynamo action can be described in terms of either "induced electric fields" or "wind-driven currents" (RISHBETH; GARRIOTT, 1969).

Figure 2.4 - Electrodynamics of E region.
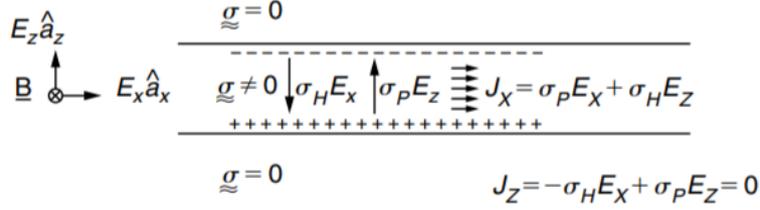
A thin conductive layer will be considered to understand better the physics of the E region dynamics, where the current flow is confined between 90 and 140 km in height. Also, vertical currents can be negligible. Figure 2.4 illustrates the E dynamo mechanism, where the thin layer is subject to a constant zonal electrical field (E_x).

The electric field perpendicular to $\vec{B}$, E_x, creates an electric current in its own direction termed as the Pedersen current ($\sigma_p E_x$). In addition, E_x also creates a current perpendicular to the plane ($E_x,\vec{B}$), in the $-\hat{z}$ direction, known as the Hall current ($\sigma_H E_x$). Since Hall current cannot flow across limits, charges accumulate at its borders, and this generates an electric polarization field directed upwards ($E_z\hat{z}$).

In the initial state of this layer model, there is no vertical current that can flow. The Pedersen current (generated by the polarization field $\sigma_p E_z$) in the direction $+\hat{z}$ cancels the current Hall ($\sigma_H E_z$). In addition, the $E_z\hat{z}$ electric field also generates a Hall current in the direction $+\hat{x}$ which is added to the Pedersen current ($\sigma_p E_x$). As already explained, the sum of the two vertical currents leads to (KELLEY, 2012):

$$J_z = -\sigma_H E_x + \sigma_p E_z = 0 \tag{2.7}$$

this implies that

$$E_z = \frac{\sigma_H}{\sigma_p} E_x \tag{2.8}$$

Since $\sigma_H > \sigma_p$, the vertical electric field component considerably exceeds the zonal electric field component. In summary, E_z has the same dependence on z as the function $\sigma_p(z)/\sigma_H(z)$. In the horizontal direction ($\hat{x}$) the sum of the two zonal currents leads to the result:

$$J_x = \sigma_H E_z + \sigma_p E_x \tag{2.9}$$

Using the result of Equation 2.7 the resulting zonal current is:

$$J_x = \left[\frac{\sigma_H^2}{\sigma_p^2} + 1\right]\sigma_p E_x = \sigma_c E_x \tag{2.10}$$

This result shows that the zonal conductivity of the region is increased above the Pedersen conductivity by a factor $\sigma_H^2/\sigma_p^2 + 1$. The magnitude $\left(\sigma_H^2/\sigma_p^2 + 1\right)\sigma_p$ is known as Cowling conductivity, which points perpendicular to the Earth's magnetic field.

Thus, the sum of these effects generates an electric current to the east in the daytime hemisphere and to the west in the nighttime hemisphere at approximately 105 km of altitude in the E equatorial region. It covers a range of $\pm 3^o$ latitude around the dip equator and is called Equatorial Electrojet (FORBES, 1981).

2.3.3 F-region dynamo

In F region, thermospheric winds are generated due to the absorption of solar radiation. These winds are horizontal and drive the plasma along the magnetic field lines. The main movement induced by thermospheric winds is the drift of ions and electrons along the magnetic field lines, proportional to the wind component in the field's direction. Additionally, there is a smaller scale movement in the direction perpendicular to both the field and the wind (BATISTA et al., 1986), given by:

$$\vec{V} = \frac{v\omega}{v^2 + \omega^2}\frac{\vec{U} \times \vec{B}}{B} \tag{2.11}$$

where the speed of the charged particles is represented by $\vec{V}$, $\vec{U}$ is the neutral wind speed, $\vec{B}$ is the terrestrial magnetic induction vector, v is the frequency of collision between neutral particles and charged particles and $\omega = q\vec{B}/m$ is the gyrofrequency

of the particles, q being the charge and m the mass of the particle.

Due to the dependence on the charge q, the ions will move in the $\vec{U} \times \vec{B}$ direction, and the electrons will move in the opposite direction, generating an electric current. Any divergence in the flow of this current tends to establish an electric polarization field.

However, as previously mentioned, the highly conductive diurnal E region, coupled to the F region through magnetic field lines, discharges this polarizing electric field. This circuit does not close during the night, and, therefore, the electric field of polarization of F region can be established (BATISTA et al., 1986; RISHBETH, 1971). This field is vertical and produces the plasma's zonal (eastward) movement at night in F region. A schematic representation of such a situation is shown in Figure 2.5.

Figure 2.5 - Schematic representation of the dynamo produced by winds in the equatorial F region. The $\vec{U}$ wind is perpendicular to the plane of the figure and points east, producing the ionic drift $V_{i\perp} = Uv/\omega$ (dashed arrows) normal to field lines. The circuit is closed by the current parallel to the field lines, $j_\parallel$ and the E-region current (short circuit).
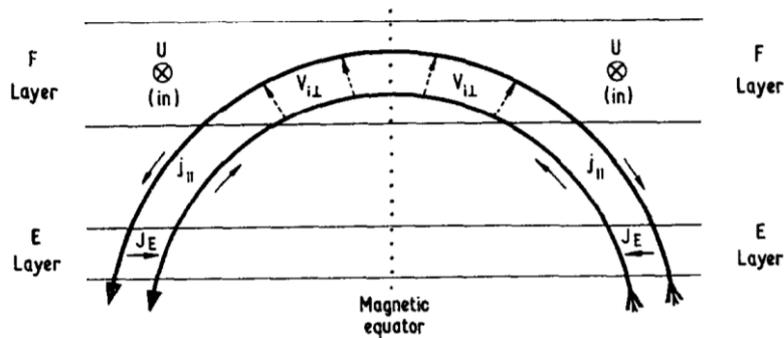
Source: Rishbeth (1971).

The pattern of zonal drifts in F region is shown in Figure 2.6, obtained in Jicamarca for the period between 1970 and 1988. According to (FEJER et al., 1991), the zonal drifts of F region do not show significant seasonal variations and with solar activity, showing slight variation with solar flux during the equinoxes.

Figure 2.6 - Seasonal variation of average zonal drifts during periods of high and low solar flux is shown on the left. Average zonal drifts during periods of equinox for low, moderate and high solar flux (right).
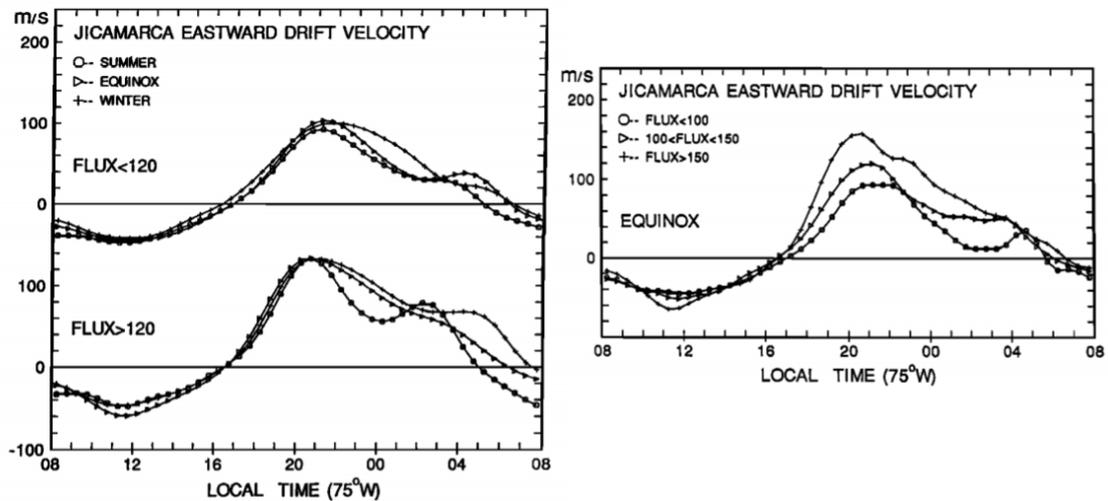
Source: Fejer et al. (1991).

The F region dynamo current is less intense than the currents generated by the E region dynamo. However, it becomes crucial in situations such as those which occur after sunset. The electric field of polarization of the F region's dynamo is vertical. It is responsible for intensifying the vertical drift upward in F region at dusk, termed Pre-Reversal Enhancement (PRE).

The pre-reversion peak results from the interaction of the zonal thermospheric wind (towards the east at dusk) with the longitudinal gradient/local time of the integrated Pedersen conductivity of E layer existing through the solar terminator (RISHBETH, 1971; HEELIS, 2004; BATISTA et al., 1986; FEJER et al., 1991; ABDU et al., 2003; FARLEY et al., 1986).

The characteristics of vertical drifts in the F region are shown in Figure 2.7, obtained from radar measurements in Jicamarca (Peru) in magnetically calm periods (FEJER et al., 1991). In the figure, the diurnal ascending pattern of drifts and the nocturnal descending pattern can be seen. A significant seasonal dependence on the PRE can also be seen, which is more significant in the equinox and summer months than in winter.

The electric fields and currents generated by the ionospheric dynamo are relatively weak at high latitudes than those generated by the influence of changes in the solar wind/magnetospheric dynamo. Further details on the complex systems of generation

17

of electric fields and the influence currents in the global ionosphere can be found in (RISHBETH, 1971; HEELIS, 2004).

Figure 2.7 - Vertical plasma drifts from F region over Jicamarca (Peru) based on incoherent scattering radar measurements for different solar fluxes and seasons.
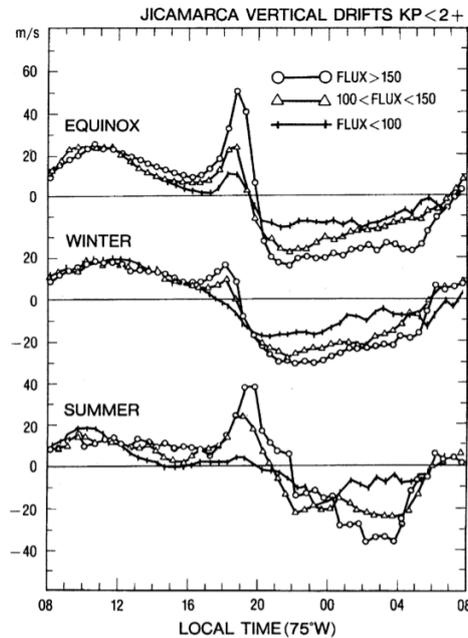
Source: Fejer et al. (1991).

2.3.4 Equatorial Ionization Anomaly (EIA)

The equatorial and low latitude ionosphere/thermosphere system has some plasma and neutral processes, which are distinctive to this region due to the unique geomagnetic field configuration. An example of such processes are Equatorial Electroject and Equatorial Ionization Anomaly (EIA) (HEELIS; HANSON, 1980; BALAN; BAILEY, 1995; HANSON; MOFFETT, 1966; MARTYN, 1947; APPLETON, 1946; ENGLAND et al., 2006).

The EIA has an essential role in the spatio-temporal distribution of ionization over low and equatorial latitudes. The spatial distribution of ionization density, primarily during daytime over low and equatorial latitudes, is characterized by two crests of ionization over low latitudes and troughs at the dip equator.

In fact, in regions close to the geomagnetic equator, there is a plasma depletion, with peaks of electronic concentration around approximately $\pm 20°$ of magnetic latitude.

The zonal diurnal electric field directed east combined with the north-south geomagnetic field (both parallel to the Earth's surface at the equator) generates a plasma source that extends hundreds of kilometers away from the equator (BALAN et al., 1997). During the day, the upward drift $\vec{E} \times \vec{B}$ raises the plasma to high altitudes.

The plasma that was carried up by the upward movement diffuses downwards along the magnetic field lines (MITRA, 1946; HANSON; MOFFETT, 1966) due to gravity and pressure gradients to the regions away from the equator. This movement of the plasma, upward and downward along the field lines, is termed the fountain effect.

Therefore, the peaks in the electronic concentration in the regions far from the equator are maintained by the plasma diffusion from the regions over the equator. A schematic representation of such a situation is shown in Figure 2.8.

Figure 2.8 - Illustration of the equatorial electrodynamics and the formation of the equatorial anomaly in F_2 ionization density.
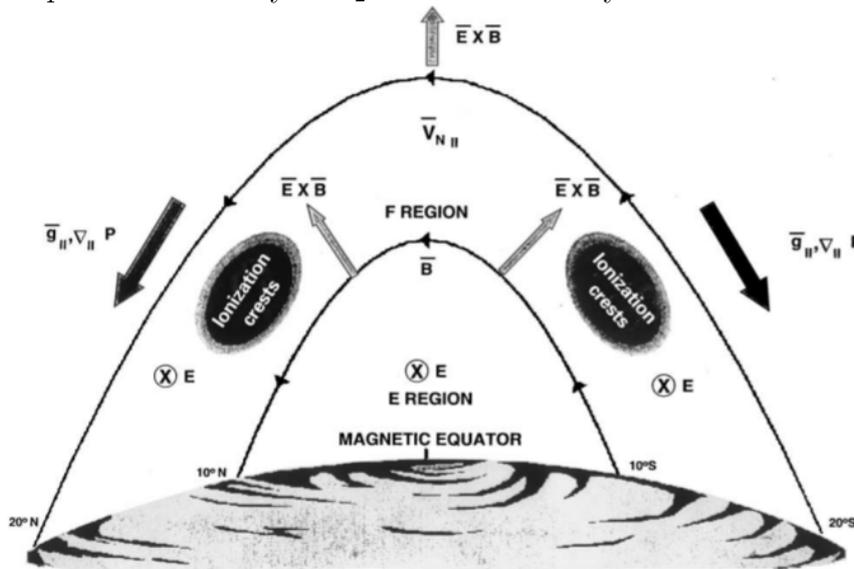
Source: Basu et al. (2002).

The morphology and variation mechanism of EIA have been extensively studied in different sectors of the equatorial and low latitude ionosphere using different kinds of data source, such as ionosonde data, total electron content (TEC) from satellite beacons, in situ satellite measurement and numerical models (YEH et al., 2001; ZHAO et al., 2009; NOGUEIRA et al., 2013; PAES et al., 2014; TAKAHASHI et al., 2014a; KHADKA et al., 2018; WATTHANASANGMECHAI et al., 2015; ABDU et al., 1991b; ANDERSON et

al., 2002; CHEN et al., 2008; NOGUEIRA et al., 2011; VENKATESH et al., 2015; BOLAJI et al., 2016; BATISTA et al., 1986; BATISTA; ABDU, 2004; SOUZA et al., 2003; ABDU et al., 2008; FAGUNDES et al., 2005; CHEN et al., 2008; NOGUEIRA et al., 2011; FEJER et al., 1991).

EIA also exhibits diurnal, seasonal, and solar cycle variations (UNNIKRISHNAN et al., 2002), and it is suggested that these features are influenced by several factors, such as the thermospheric wind, ionospheric electric field, local geomagnetic configuration, and subsolar point location (HEELIS; HANSON, 1980; BALAN; BAILEY, 1995). The following section will extensively center on global observations of the EIA using various observational instruments and techniques.

2.3.5   The observation of EIA over the Southern American sector

In equatorial and low-latitude of Brazil, Nogueira et al. (2011) investigated the effect of geomagnetic storms on the intensity of EIA using the critical frequency layer (f_0F_2) and TEC measurements collected from digisondes and GPS receivers, respectively.

The EIA was calculated using the differences between the F layers equatorial and low latitude peak density at these locations. The meridional wind component, on the other hand, was calculated using the difference between the genuine heights (h_F) of the locations. During the storm phases depicted in Figure 2.9, they found an exceptionally early morning enhancement of the EIA. On the other hand, the observed changes were linked to rapid electric field penetration.

Figure 2.9 - Magnetic storm effects during November 23-27, 2001, on the EIA development. From top to bottom, the geomagnetic Dst index, the convection electric field ($\vec{E}_y$), the interplanetary magnetic field B_z and the AE index. The last two panels refer to the EIA development, where the red and the black lines represent the quiet and disturbed periods of the EIA development during the storm. The fourth panel was obtained from digisondes (f_0F_2) and the bottom panel from GPS receivers (VTEC).
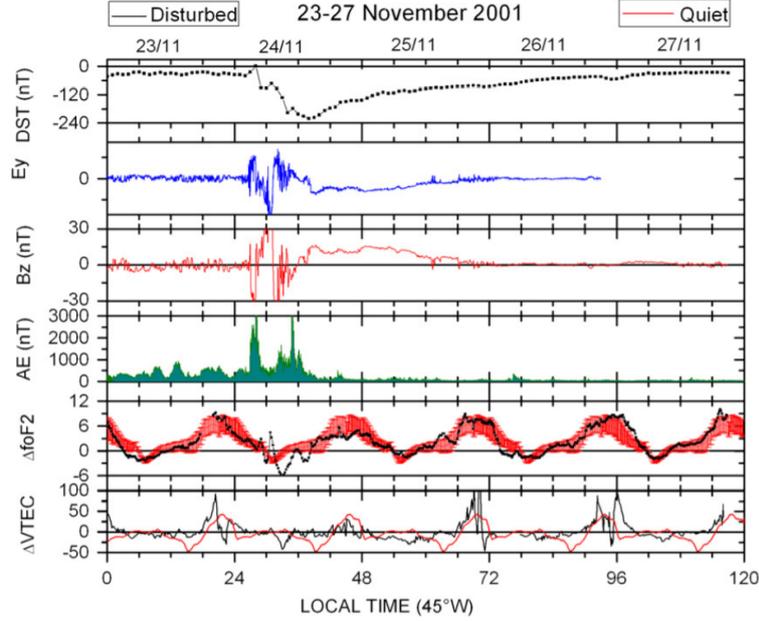
Source: Nogueira et al. (2011).

Using TEC maps calculated from GNSS receivers over Brazil, Takahashi et al. (2014a) also studied the daytime of the EIA crest to trough variation at a fixed local time (15:00). Their results revealed a larger amplitude of TEC values at the crest (18°S) as compared to the trough (longitude 50°W) regions. Also, they reported a semimonthly variation of TEC throughout the year from January to December. In addition, they observed significant TEC values in the months of March-April and October-November.

On the western side of Southern America, Khadka et al. (2018) investigated the effects of meridional neutral winds on the development of the EIA crests asymmetry structure. The authors used daytime data obtained by GPS TEC and Low Latitude IOnospheric Sector numerical model (LLIONS). They realized that the EIA crest parameters, such as strength, shape, amplitude, and latitudinal width, were affected by the eastward electric field associated with EEJ during calm conditions. The EIA crest asymmetries observed were found mainly during solstices, September equinox,

and March equinox seasons.

Dias et al. (2020) also studied day-to-day and month-to-month characteristics of the EIA longitudinally in closely spaced sectors (i.e., eastern, middle, and western) during the year 2016 in the descending phase of the solar activity, using GPS TEC. The EIA crests intensities showed a semi-annual variation in all sectors, having a minimum in winter and maximum during the summer and spring seasons. Also, notable variations were observed from the EIA based on the shape, strength, extent, and evolution.

Romero-Hernandez et al. (2018) studied solar activity influences, seasonal variations, and hemispheric asymmetries of TEC. It was done using daytime ionospheric variation using TEC data collected by four ground-based GNSS networks. The measurements covered entire Latin America, from Patagonia to the north of Mexico, during two periods of different solar activity conditions: 2011 (ascending phase) and 2014 (maximum).

Their results revealed an equinoctial asymmetry with an opposite configuration in the TEC variation in high and moderate solar activity. Besides, they attributed the changes observed in 2011 to solar flux change. The annual TEC variations for 2011 and 2014 is shown in Figure 2.10. The same figure shows TEC variation, characterized by two crests related to the maximum ionization occurring during equinoxes. A minimum of TEC is observed in the June-July months for both phases of the solar cycle.

Figure 2.10 - Annual TEC variations at noontime during 2011 (up) and 2014 (down) for two GNSS stations located in the northern (MANA) and southern (SMAR) hemispheres.
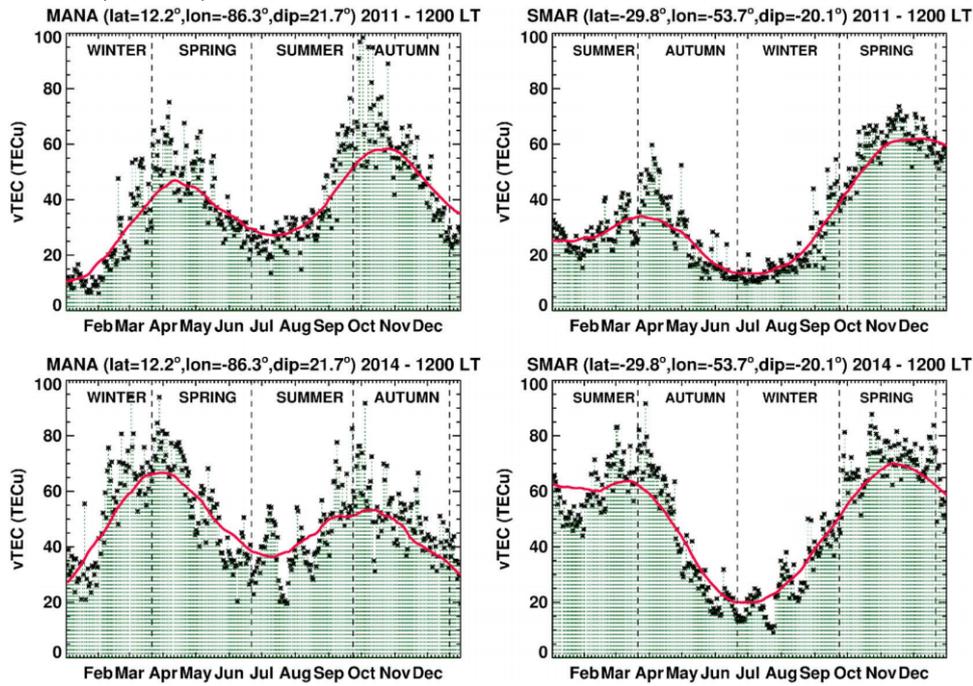
Source: Romero-Hernandez et al. (2018).

By comparing both years of observation, it also can be noted that the TEC trend, especially at the crests, exhibits a different configuration, and the electron density level changed, especially when looking from crest to crest. Also, from the months of June-July minimum, TEC levels can be noticed. However, TEC during 2014 is higher than 2011. A comparative analysis was done using the wind model (HWM-14) to explain the TEC variation in 2014, but it could not interpret the observed variations.

2.3.6   Observations of EIA over the African sector

In the African sector, the EIA has been investigated using numerous techniques amidst others, and this section will elaborate on the studies done by Bolaji et al. (2017), Mungufeni et al. (2018) and Amaechi et al. (2019).

Bolaji et al. (2017) investigated the morphology of the EIA using ground-based magnetometers and GPS TEC over Africa-Middle East during a year of deep minimum. The authors reported that the EIA crests extended latitudinally to both hemispheres showing different structures than those in other sectors. In addition, they observed

23

twin EIA crests over higher latitudes produced in the early morning hours, which were attributed to weak equatorial electrojet (EEJ) measurements.

Furthermore, an EIA crest pattern was observed in February, with reduced TEC magnitude at the stations above the magnetic equator. Also, well-developed EIA crests were noticed in the northern and southern hemispheres in March, with a steady increase in the magnitude of TEC values in both hemispheres. More importantly, they observed a higher magnitude of TEC values of the EIA in the northern hemisphere than those in the southern, over the four months of observations. They attributed these variations to the equatorial electrojet (EEJ) currents. However, they further suggested that more analysis is needed to explain the dynamic mechanisms responsible for EIA variations.

Mungufeni et al. (2018) also studied the correlation between the equatorial electrojet and the EIA occurrence over East Africa during quiet geomagnetic conditions. They used TEC measurements obtained from GNSS ground base receivers and magnetometers data. Their analysis quantified the TEC ratio over the crest to that over the trough region to characterize the EIA's morphology. They found out that the trough lay slightly south of the magnetic equator $(0 - 4°S)$.

Additionally, they observed high, prominent EIA occurrence in equinoctial and December solstice seasons. Generally, the EIA strengths observed in the June solstice were weaker compared to other seasons. Figure 2.11 illustrates the monthly mean TEC as a function of magnetic latitude and local time.

Figure 2.11 - Contour plots of monthly mean TEC as a function of latitude and LT. (a-j) are for November and January-September.
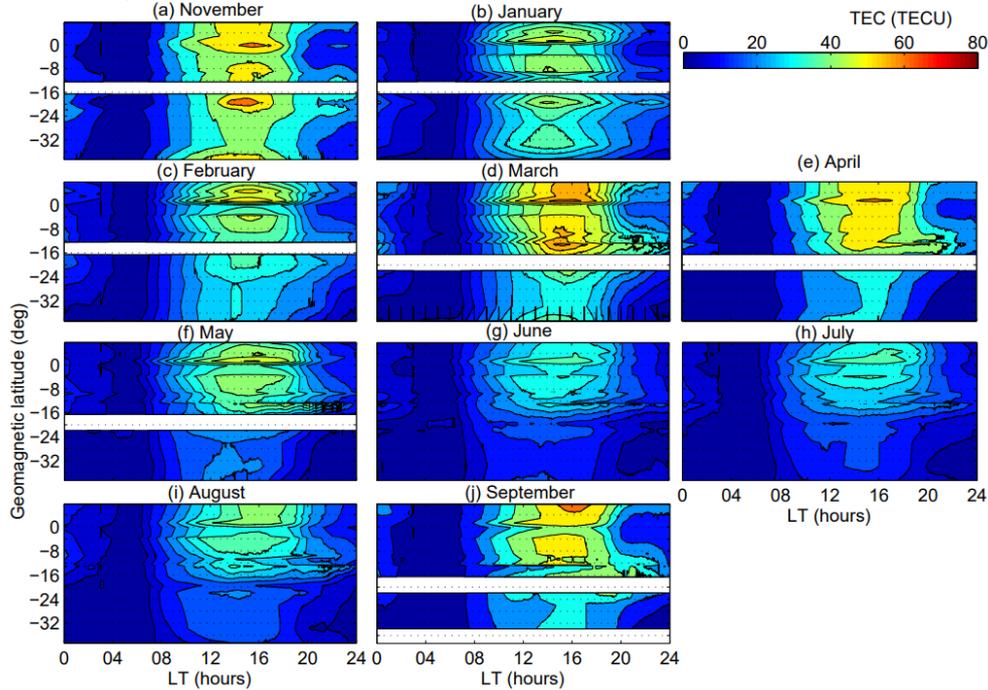
Source: Mungufeni et al. (2018).

The figure shows that the occurrence of the EIA during equinoctial months (February-April, August, September) and November persisted beyond 20:00 LT. EEJ strengths were compared to seasonal variation of the EIA magnitudes, and it revealed that daytime EIA strengths mainly were positively correlated with daytime EEJ strengths.

According to the authors, their observations were done during the high solar activity period. Further analysis is needed during the solar minimum period, which they believe might show significant EIA variation. However, their studies only used few GNSS receiver stations.

Amaechi et al. (2019) investigated the variation of the magnitude and positions of the EIA crest during noon and post-sunset periods using GPS TEC and magnetometer data. Their observations revealed the formation of the EIA crests varying from 14:00-17:00 LT, and there was asymmetry of the anomaly crests regarding the geomagnetic equator. Figure 2.12 shows contour maps of the monthly mean diurnal variation of TEC for the year 2013 over the African EIA.

From Figure 2.12, the time of occurrence of the crests was found to vary from 14:00

LT to 17:00 LT. However, in March and August, both crests formed at the same time (17:00 LT), as well as in April and October (16:00 LT) and December (15:00 LT). In January, February, and November the northern crest formed earlier than the southern crest, while the reverse happened in May, June, and September.

It can also be seen that the position of the southern crest varied from $-12.62°$ to $-9.17°$ dip latitude while that of the northern crest varied from $4.91°$ to $7.36°$ dip latitude. The EIA was compared using estimated vertical drift velocity from ΔH parameter measured from local magnetometer data. They found out that ΔH was the crucial parameter driving the dynamics of the position and magnitude of the EIA crests on a monthly and seasonal basis.

Figure 2.12 - Monthly variations of the position and magnitude of the African EIA crests for year 2013.
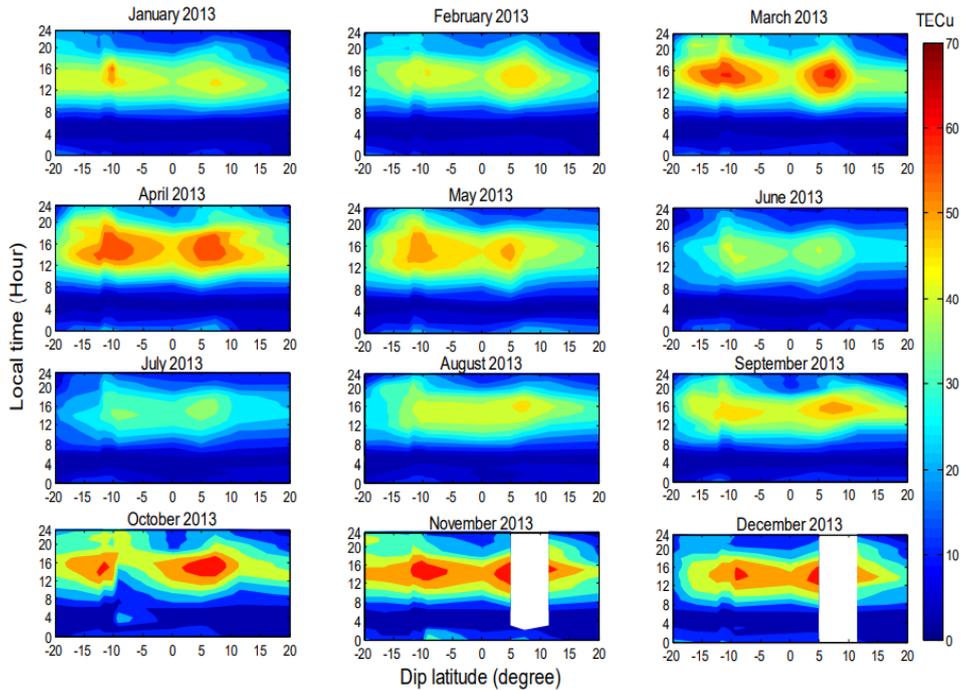
Source: Amaechi et al. (2019).

Also, the time response of the formation of the EIA noon crests was about 3 hours after the minimum ΔH. More importantly, the authors found out poleward and equatorward movement of the crests during equinoxes and winter/summer, respectively, which has not been reported in that sector. The movement of the crest positions might result from thermospheric meridional wind that modulates the African EIA morphology. They suggested that wind patterns and transport processes are

mechanisms that still require investigation over Africa.

2.3.7 Observations of EIA over the Asian sector

The structure of EIA has been extensively studied using various observational instruments and techniques, among others, this section will discuss the works done by Ram et al. (2009), Huy et al. (2014),Yue et al. (2015) and Mo et al. (2018) which used GPS TEC to study EIA over the Asian sector.

In the Asian sector, the structure of EIA can be traced back to the work of Golton e Walker (1971) based on the recording of the Faraday rotational of signals from the geostationary satellite. Since then, subsequent studies have investigated EIA evolution structure related to the local time and season under different solar activity phases.

Ram et al. (2009) studied the seasonal, longitudinal, and temporal variations in the interhemispheric asymmetry variations of EIA during the low solar activity period, from November 2006 to October 2007. They noticed that the EIA crest in the winter hemisphere appears stronger from morning to noon in the solstice.

Figure 2.13 - Latitudinal cross-section plots depicting the time evolution of EIA during the northern winter period of January to February 2007 along (a) 120°±5° and (b) 80°±5°. The plots correspond to the peak (Figure 2.13 a) and valley (Figure 2.13 b) regions of the four-peaked longitudinal structure of EIA.
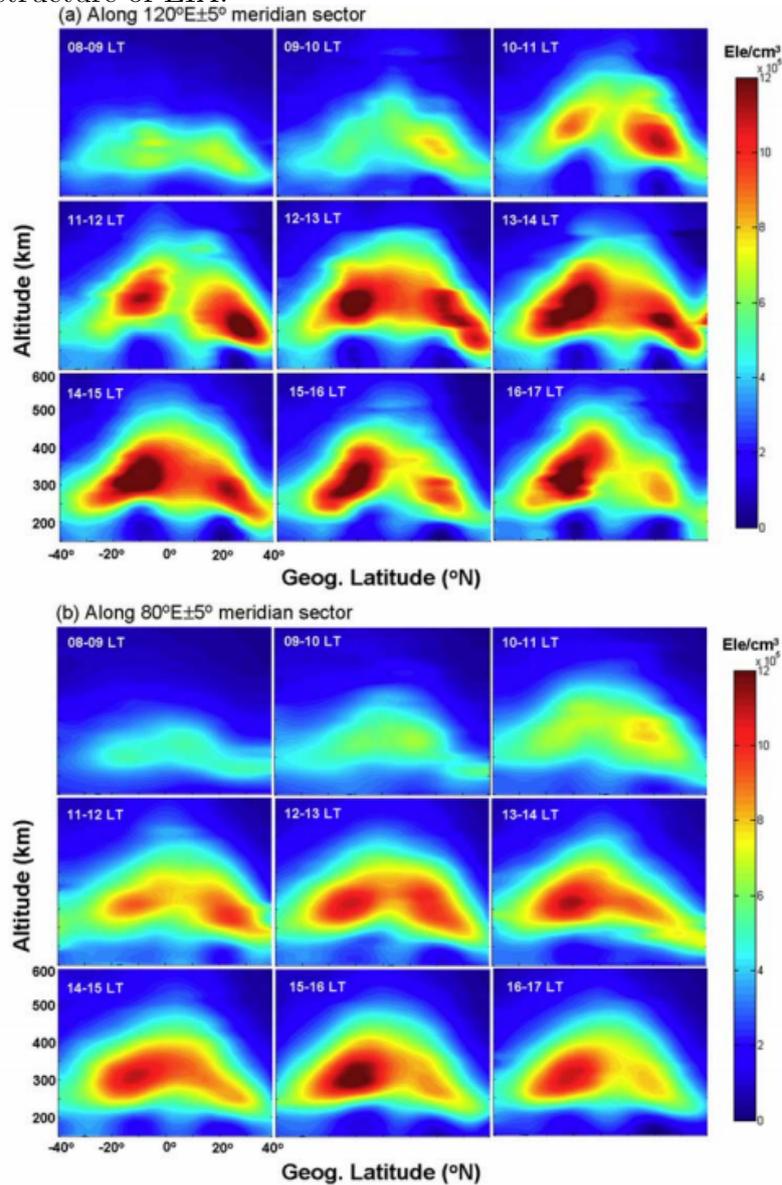
Source: Ram et al. (2009).

From Figure 2.13a, the two crests of equatorial ionization anomaly can be seen at 08:00-09:00 LT, but they become more prominent at 10:00-11:00 LT. Furthermore, it can also be seen from Figure 2.13a that the EIA crest in the northern/winter hemisphere is stronger than the crest in the southern/summer hemisphere at 09:00-10:00 LT. As the electron density continues to pile up, both crests are further intensified,

and the winter crest continues to be stronger than the summer crest up to 12:00 LT.

On the other hand, similar local-time EIA crests variation can be seen at the valley region at $80°E \pm 5°$ meridian sector (Figure 2.13b). However, the magnitude of EIA crests observed in this sector is smaller than those found at $120°E \pm 5°$ sector. The EIA crests behavior was compared with a low latitude to midlatitude ionospheric model SAMI2. The authors reported that the SAMI2 model simulation results exhibit similar EIA crests local-time-dependent variation.

In addition, EIA crests hemispheric asymmetry was observed, having intense crests in winter months at morning to noon and summer months at afternoon hours. It was attributed to the intensified equatorial fountain process that dominates the transequatorial neutral wind during these local hours and reduces the field-aligned plasma transport from summer to winter hemisphere. Their survey also showed a distinct four-peaked longitudinal variance in the EIA across the western American and western Africa. It was attributed to large oppositely declined magnetic field lines on either side of the South American continent.

Also, Huy et al. (2014) investigated the time variations of TEC in the South East Asian EIA during the period 2006-2011 using a latitudinal chain of GPS stations in the northern and southern hemispheres. A semi-annual TEC pattern was observed in all stations with the maximum at the equinox.

Furthermore, in both hemispheres, the crests intensities were more prominent in spring than autumn from 2006 to 2008, and smaller in spring than in autumn from 2009 to 2011. The amplitude and position of the two crests in both hemispheres exhibited an asymmetry nature. Figure 2.14 illustrates an example of the TEC latitudinal variations for each month of the years 2006 and 2007, respectively.

Figure 2.14 - Time and latitudinal monthly average TEC map for the (a) 2006 and (b) 2007.
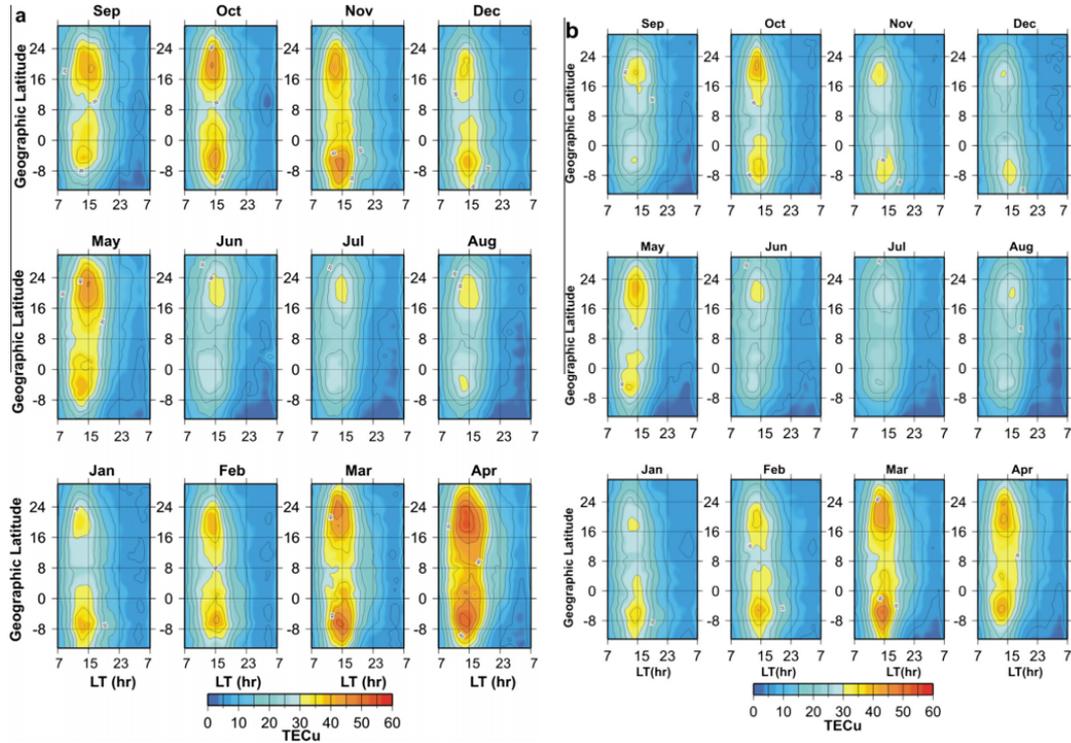
It can be seen in Figure 2.14a an interhemispheric asymmetry of the EIA crests during November 2006. In addition, TEC levels of the EIA crests are more intense in the southern hemisphere than in the northern one. A similar trend can be seen from June-July, but in this case, the TEC level of the crests is more intense in the northern hemisphere.

Moreover, the authors revealed that the observed EIA crests move equatorward in winter than in other seasons. Also, a high correlation between the TEC intensities at both crests and the sunspot number was noticed. However, they suggested that further analysis is needed to understand the factors responsible for such observed EIA crests variations.

Yue et al. (2015) also studied the EIA morphology throughout the years of 2006 to 2014. The authors used ionospheric peak density (NmF2) and peak height (hmF2) derived from electron density profiles obtained by GPS radio occultation measurements. Their result revealed a decrease in the TEC level of EIA crests during the years of observations. Also, semi-annual variations of TEC were observed in all sea-

sons, with NmF2 and hmF2 having more intense EIA crests in equinox than those observed in the solstice.

An evident solar cycle variation of the anomaly crests TEC level was observed over the years. However, the authors also suggested that electrodynamics processes responsible for the interhemispheric variations of the EIA crests need to be further investigated.

Also, Mo et al. (2018), made a comprehensive study on the morphological characteristics of EIA crest at Nanning (22.84°N, dip latitude $\sim$ 12.14°N) using GPS TEC over station situated near the daytime EIA crests region. Their observations revealed that the TEC and the magnetic latitude location of the EIA crest experienced an ascendant and descendant process with the daytime EIA crest evolution. In addition, the TEC and MLAT location of the EIA crest was stronger and higher in equinoctial months than in solstice.

Figure 2.15 - The MLAT location of EIA crest as a function of local time for four seasonal months in the solar minimum (2009) and maximum (2012) years, respectively.
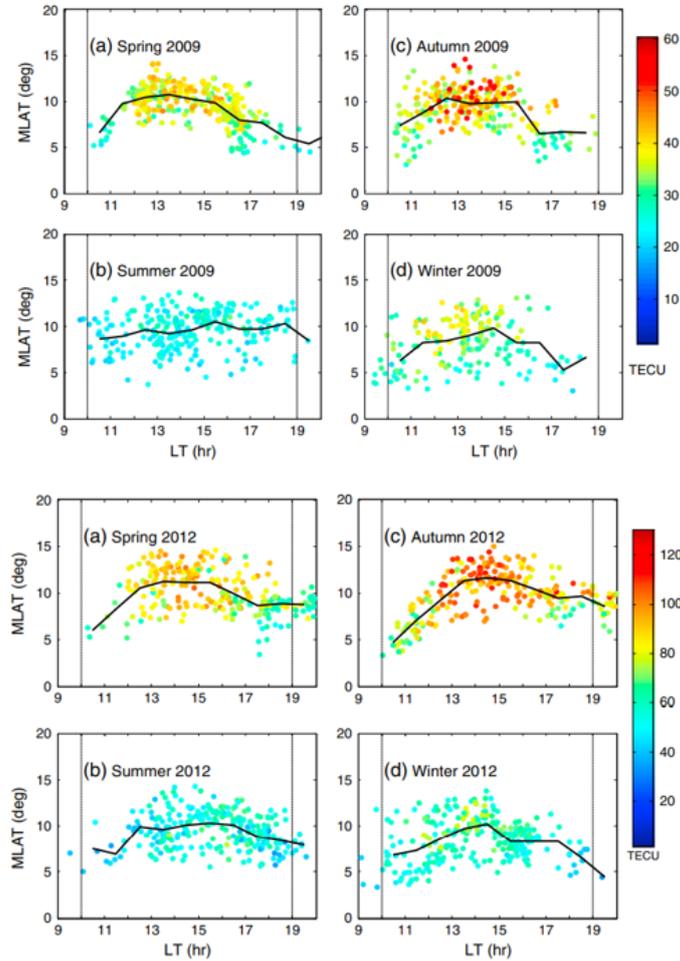
Source: Mo et al. (2018).

Figure 2.15 gives the variation of the magnetic latitude locations of daytime EIA crest with local time for spring, summer, autumn, and winter months during solar minimum (2009) and maximum (2012) period. Each point in the Figure 2.15 represents the EIA crest obtained from one effective continuous pass of ionospheric pierce point across the EIA crest.

The corresponding EIA TEC values are marked with the color scale. The black line is the monthly average of the EIA crest's magnetic latitude location for each hour. Considering the limitation of their method to obtain the EIA crests location, the EIA crests local time variations were focused on the time interval between 10: 00 and 19:00 LT. On the whole, the EIA crest exhibits the local time variation.

Furthermore, in Figure 2.15a, it can be seen that EIA crests exhibit clear diurnal evolution in spring months during solar minimum period. The crests of the EIA are found near magnetic latitudes 5°N at about 10:00 LT. Subsequently, the EIA crests start to move poleward, with having high intensity at about 14:00 LT, near magnetic latitudes 11°N. A sudden shift of the EIA crests can be seen in equatorward near magnetic latitudes 5°N, around 18:00 LT.

As reported by the authors, the variation of EIA crest locations and TEC level above suggest that the EIA crest diurnal variation exhibits some seasonal dependence concerning local time. A similar trend of the EIA crests behavior can also be seen during 2012, solar maximum period, but with some slight variations in the shape and latitudinal locations of the crests.

A comparison of the EIA crests observed pattern was made using EEJ intensity measured from ground-based magnetometers. The authors found a strong correlation of the EIA crest locations with the EEJ intensity measured. They revealed that the EIA crests intensities show some dependence on solar activity. However, the dynamic processes and mechanisms responsible for these observed variations of the EIA crests and magnetic latitude locations were suggested to be investigated.

Although the EIA development in various longitudinal sectors is driven by the $\vec{E} \times \vec{B}$ convection, its morphology, latitudinal positions of the crests, and intensities show some variations, according to the studies mentioned above. Furthermore, the Earth's magnetic field is tilted, offset, and distorted at these distinct sectors (i.e., South American, African, and Asian). The locations and intensities of the EIA's two crests are likewise affected by differences in electric fields and neutral. Geographic and seasonal interdependence can be found in the EIA in these sectors.

3 METHODOLOGY AND DATA ANALYSIS

This chapter will present the methodology used to determine the main characteristics of the Equatorial Ionization Anomaly (EIA). Data from Global Navigation Satellite System (GNSS) network receivers over the Southern American continent were used to observe the EIA crests. Some fundamentals of spectral analysis will also be presented.

The Sheffield University Plasmasphere Ionosphere Model at Instituto Nacional de Pesquisas Espaciais (SUPIM-INPE) is a tool used to study and understand the physical and chemical processes of the ionospheric regions, and some ionospheric phenomena. The primary mathematical equations and the input parameters of the SUPIM-INPE model will be briefly described. In this thesis, the SUPIM-INPE is used to explain some dynamics of the EIA.

3.1 Global Navigation Satelite System (GNSS)

Global Positioning System (GPS) was the first of a new generation of navigation satellite systems to become operational. Similar systems and satellite-based augmentation are being developed and deployed by governments, international consortia, and commercial interests. The generic name given to these systems is the Global Navigation Satellite System (GNSS).

In 1960s, the United States of America department of defense developed a navigation system based on the Global Positioning Systems (GPS), which went into full operation in 1993, offering an excellent study opportunity of the Earth ionosphere on a global scale. GPS is made up of a constellation of 32 satellites with global coverage.

In 1980s, the Russian positioning system called GLONASS (Globalnaya Navigazionnaya Sputnikovaya Sistema, in Russain) emerged, composed of 24 satellites. They were developed during the Cold War for communication, but the government conserved its satellites as a multi-purpose platform with the end of it.

Another well-known satellite navigation system is Galileo, which was conceived as a joint public-private enterprise under civilian control, financed and managed by the European Commission (EC), the European Space Agency (ESA), and currently comprises 18 satellites.

Also, the Chinese developed regional satellite navigation called "BeiDou Navigation

Satellite System". They launched their first two GEO satellites late in 2000 and another in May 2003, but currently has 22 satellites in orbit with global coverage, which provides positioning capability over China and neighboring areas. BeiDou is an active system that, unlike GPS, GLONASS and Galileo, interacts with the users.

Besides, in conjunction with an industry consortium, the Japanese government developed the Quasi-Zenith Satellite System (QZSS), a regional system to transmit differential corrections to GPS and other GNSS satellites launched in 2008. The Indians have also a similar system (ZARRAOA et al., 1995; PEREIRA; CAMARGO, 2017; SABZEHEE et al., 2018).

The navigation systems mentioned above are part of the GNSS network, used to describe the constellation of satellite positioning systems currently in operation. Each GPS satellite continuously transmits two radio frequencies in L-band, generally referred to as Link 1 (L1) and Link 2 (L2), respectively.

The L-band covers frequencies between 1 GHz and 2 GHz. It is a subset of ultra-high frequency (UFH) band, specially coded, allowing the receiver to compute positioning, speed, and time. It is worth mentioning that each of the constellations employs specific frequencies, different from the GPS. Nowadays, there is a new signal called L5 with a frequency of 1176 MHz and a wavelength of 24.48 (OGAJA, 2011).

When the signal for each satellite reaches the receiver, it is decoded, and, thus, it is possible to measure the time and phase between the satellite and the receiver, and this provides the pseudorange information (P1, P2) and the phase (Φ_1, Φ_2) of the signal (see Table 3.1 for more details). Only the GPS was considered to estimate Total Electronic Content (TEC) maps over South America in the present work.

Table 3.1 - Frequencies and their respective wavelengths for GPS system signals.

Frequency (MHz)	Wavelength (cm)
f1=1575.42	$\lambda_1 = 19.05$
f2=1227.60	$\lambda_2 = 24.45$

Source: Monico (2007).

From this information, if we use dual-frequency GPS receivers at two lower-band GPS frequencies f_1 (1575.42 MHz) and f_2 (1227.60 MHz), then the electron content of the ionosphere in each considered station will be known (HOFMANN-WELLENHOF et al., 2012a).

3.1.1 Calculation of Total Electron Content (TEC)

The ionosphere is a refractive medium for electromagnetic waves (DURMAZ; KARSLI-OGLU, 2015). Although it seems to be a hindrance for positioning and communication, it appears to be a valuable source of information related to the electron content of the ionosphere (SCHAER; NATURELLES., 1999).

Total Electron Content (TEC) is defined as the line integral of electron density on a given ray path (i.e., between the satellites and the receiver on the ground) (HOFMANN-WELLENHOF et al., 2012b). TEC corresponds to the total number of free electrons in a cylindrical path with a 1 m^2 cross-sectional area.

It is widely used in space weather studies for the investigation of ionospheric variability. TEC can be expressed as the integral of the electron density along the path between the satellite and the receiver (ABDULLAH et al., 2009), expressed as (SEEBER, 2008):

$$TEC = \int_{receiver}^{satellite} N_e ds \qquad (3.1)$$

The unit of TEC, is TECU, where 1 TECU is equal to 10^{16} electrons/m^2 (SEEBER, 2008). In Equation 3.1 N_e represents the electron density, and ds is an element of length between the satellite and the receiver.

However, Slant TEC (STEC) is usually used to designate the total number of electrons on a ray path other than the local zenith direction. The slant TEC (STEC) is also known as the TEC. Figure 3.1 displays the fundamental geometry representation of how STEC is estimated along the signal path.

Figure 3.1 - Schematic drawing of the definition of STEC.
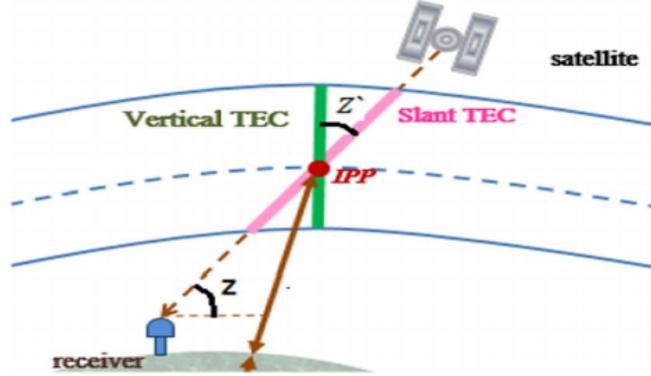
The ionosphere-free linear combination of two different frequencies helps calculate the slant TEC along the line of sight between the satellite and receiver, as illustrated Figure 3.1. The magnitude of the error due to the ionospheric effect on the GPS signals depends directly on the TEC present along the path traveled by the signal, which, in turn, is related to the ionization process in the ionosphere, and inversely proportional to the squared signal frequency (MATSUOKA; CAMARGO, 2007; SABZEHEE et al., 2018; PEREIRA; CAMARGO, 2017).

The error due to ionospheric delay ($I_{1,2}$) obtained by the pseudoranges is given in Equation 3.2 and its deduction is presented below (AFRAIMOVICH; PEREVALOVA, 2006; LEICK et al., 2015):

$$I_{1,2} = \frac{40.3}{f_{1,2}^2} STEC \qquad (3.2)$$

Indeed for a given station, dual frequency GPS receivers record carrier phases Φ_1, Φ_2 and codes P_1, P_2 observations on both the λ_1 and λ_2, two frequencies, as follows (SEEBER, 2008; GAO, 2002; SHARIFI; FARZANEH, 2017):

$$P_1 = \rho + c\,(dt - dT) + d_\rho + d_T + I_1 + b_{p1}^s - b_{p1}^r + \varepsilon\,(P_1) \qquad (3.3)$$

$$P_2 = \rho + c\,(dt - dT) + d_\rho + d_T + I_2 + b_{p2}^s - b_{p2}^r + \varepsilon\,(P_2) \qquad (3.4)$$

$$\Phi_1 = \rho + c\left(dt - dT\right) + d_\rho + d_T + \lambda_1 N_1 - I_1 + b_{\phi 1}^s - b_{\phi 1}^r + \varepsilon\left(\phi_1\right) \qquad (3.5)$$

$$\Phi_2 = \rho + c\left(dt - dT\right) + d_\rho + d_T + \lambda_2 N_2 - I_2 + b_{\phi 2}^s - b_{\phi 2}^r + \varepsilon\left(\phi_2\right) \qquad (3.6)$$

Where ρ is the true geometric range (m) between the satellite and the receiver; d_ρ is the orbital error (m); c is the speed of light (3.0×10^8 m/s); dt is the satellite clock error with respect to GPS time(s); dT is the receiver clock error with respect to GPS time(s); d_T is the tropospheric error(m); I_1 and I_2 are the pseudorange ionospheric delays(m) at λ_1 and λ_2, respectively; b_{p1}^s and b_{p2}^s are the pseudorange satellite delays (m) at λ_1 and λ_2, respectively; b_{p1}^r and b_{p2}^r are the pseudorange receiver delays (m) at λ_1 and λ_2, respectively; $\varepsilon\left(P_1\right)$ and $\varepsilon\left(P_2\right)$ are the pseudorange measurement noises which include multipath errors (m); λ_1 and λ_2 are the carrier signal wavelengths at f_1 and f_2 frequencies, respectively; N_1 and N_2 are the carrier phase integer ambiguities; I_1 and I_2 are the carrier phase ionospheric delays (m); $b_{\phi 1}^s$ and $b_{\phi 2}^s$ are the carrier phase satellite delays or interfrequency biases (m); $\varepsilon\left(\phi_1\right)$ and $\varepsilon\left(\phi_2\right)$ include the carrier phase measurement noises along with multipath errors with units of meters (m).

The "geometry-free" linear combination is determined using the difference between the pseudorange measurements or the carrier phase measurements as, follows:

$$P_2 - P_1 = I + b_p^s - b_p^r \qquad (3.7)$$

wherein

$$I = I_2 - I_1 = 40.3\frac{TEC}{f_i^2}, b_p^s = b_{p1}^s - b_{p2}^s \quad \text{and} \quad b_p^r = b_{p1}^r - b_{p2}^r \qquad (3.8)$$

where, 40.3 is the constant coefficient. Thus, TEC is extracted from the geometry-free linear combination as follows (SHARIFI; FARZANEH, 2017):

$$TEC = \frac{1}{40.3}\left(\frac{f_1^2 f_2^2}{f_1^2 - f_2^2}\right)\left\{\left(P_2 - P_1\right) - \left(b_p^s + b_p^r\right)\right\} \qquad (3.9)$$

From the above relations, the slant TEC (STEC) can, therefore, be calculated.

3.1.2 Estimation of VTEC

The Earth's ionosphere ranges in altitude from 60 to $\sim 1,000$ km and has a maximum electron density between 300-500 km (OTSUKA et al., 2002). It is assumed that all electrons in the ionosphere are concentrated in a thin shell at altitude h_l (see, Figure 3.2).

Figure 3.2 - A schematic diagram illustrating the geometry involved in calculating the VTEC.
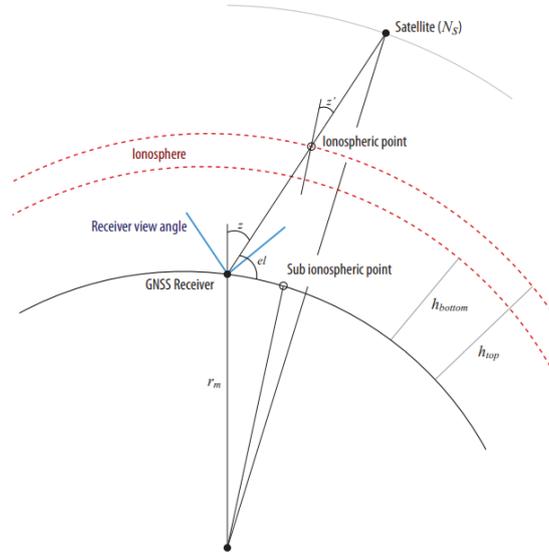
Source: Hofmann-Wellenhof et al. (2012a).

TEC measurements from both code (TEC_p) and phase (TEC_Φ) are considerably affected by instrumental delays, thermal noises, and the effects of multipath. However, the measurement of TEC from phase is more precise. Nevertheless, they contain some ambiguities (OTSUKA et al., 2002) which can be removed from the mean of the difference between the TEC_p and TEC_Φ. Hence, the relative TEC (TEC_R) can be calculated using Equation 3.10 (MANNUCCI et al., 1998):

$$TEC_R = TEC_\Phi + < TEC_p - TEC_\Phi > \tag{3.10}$$

The calculations of absolute TEC require the use of complex models to remove the instrumental biases. Some procedures can be found in (SARDÓN; ZARRAOA, 1997; DEAR; MITCHELL, 2006; OTSUKA et al., 2002). The VTEC is calculated by the TEC projection of the absolute TEC on the ionospheric piercing point (JAKOWSKI, 1996).

Therefore, VTEC is obtained by following relations:

$$VTEC = TEC \cos{(z')} \tag{3.11}$$

where

$$\cos z' = \left[1 - \left(\frac{r_m}{r_m + h_{top}} \cos z \right)^2 \right]^{\frac{1}{2}} \tag{3.12}$$

where z is the satellite elevation angle, r_m is the Earth's radius, and h_{top} is the altitude of the ionosphere thin shell, r_m is sometimes set to $6,371$ km. The present work results follow the methodology of calculating the VTEC by Otsuka et al. (2002). Henceforth, we refer to the Vertical TEC (VTEC) as TEC in our subsequent sections.

3.1.3 TEC maps

The TEC map is a two-dimensional (2-D) representation of the TEC distribution. In order to construct the TEC map, it is necessary to calculate the TEC for each satellite receiver that makes up the GNSS receiver networks over the sector. However, in this work, four main GPS receiver networks on the South American continent were utilized. The GNSS receivers, with dual-frequency, have been operated by Brazilian Continuous Monitoring Network (RBMC), the Brazilian Institute for Geography and Statistics (IBGE), the Low-latitude Ionospheric Sensor Network (LISN), and the Red Argentina de Monitoreo Satelital Continuo (RAMSAC) operated by Argentine and International GNSS Service (IGS) network.

Data from all of these receivers are collected and processed at Estudo e Monitoramento Brasileiro de Clima Espacial (EMBRACE) (ESTUDO..., 2017). The map in Figure 3.3 shows the geographic locations of the GNSS receiver sites used in the current work. It is worth noting that Brazil, Peru, Chile, and Argentina are engulfed in this manner, and many observation sites are available in South America's central region.

Figure 3.3 - Various GNSS receiver networks maintained by RAMSAC, LINS, RBMC and IGS, for the year 2014.
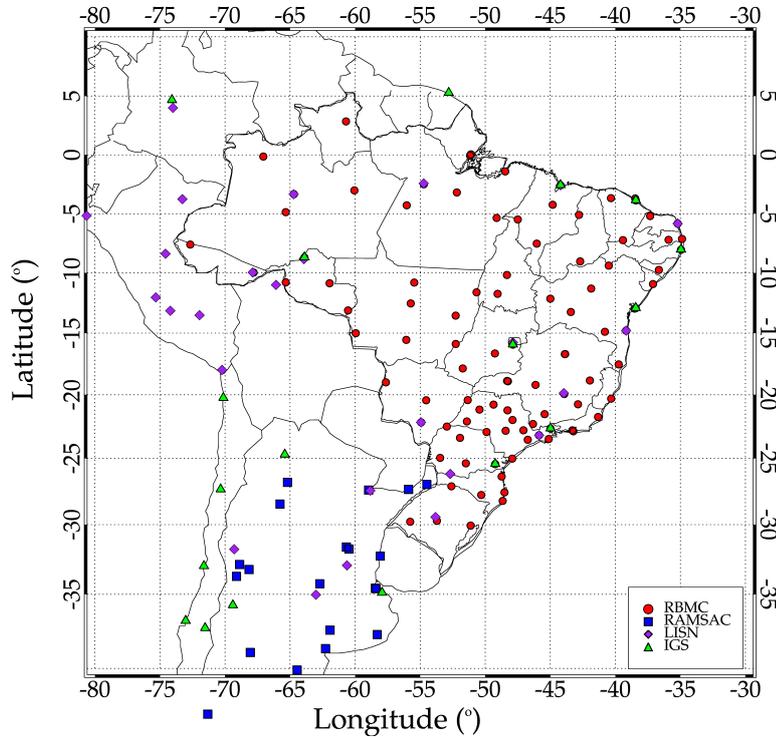
It is worth noting that the number of receiver stations has increased across the continent between 2014 and 2021. Thus, the RAMSAC network has around 129 stations, RBMC has 191 stations, LISN has 44 stations, and IGS has 30 stations. This work methodology calculated TEC using the updated number of receiver stations. In Table 3.2, the updated GNSS receiver stations over the South American continent from 2014 to 2021 are tabulated.

Table 3.2 - GNSS receiver networks over South America and their respective receiver numbers for 2014 and 2021.

Network	GNSS Receivers in 2014	GNSS Receivers in 2021
LINS	30	44
IGS	29	30
RAMSAC	67	129
RBMC	101	191
Total	**227**	**394**

After calculating the TEC for each satellite receiver, the TEC values are mapped

on the ionospheric shell at a piercing point of the line of sight. The pierce point is calculated by assuming that the ionospheric peak height is ~ 350 km altitude (OTSUKA et al., 2013). More information on TEC data mapping and data processing methods can be found in Takahashi et al. (2015).

An example of a 2D TEC map over the South American continent obtained from the methodology for February 18, 2015, at 15:50 (UT) is shown in Figure 3.4. The geomagnetic equator is depicted in this map by a continuous red line. The color bar depicts TEC levels ranging from 0 (blue) to 60 (red) TECU. On the map, ionization can be seen above and below the magnetic equator, approximately at latitude 5°N to 10°S and longitude 60°W to 35°W.

Figure 3.4 - GPS based TEC Map over South America on the daytime of February 18, 2015, at fixed time 15:50 UT. The colour shade present TECU from 0 (blue) to 60 (red). The red line indicates the geomagnetic equator.
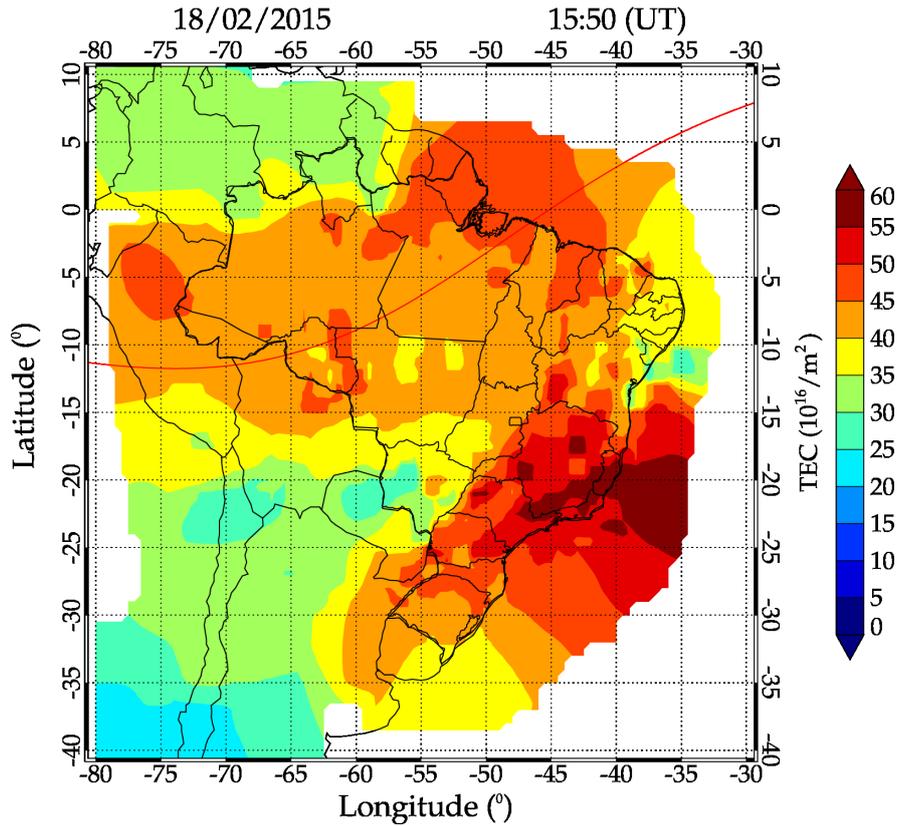
3.2 Keogram development from TEC maps

Using 2D TEC maps, the morphology and evolution of the equatorial ionization anomaly can be studied. On the other hand, maps always show the TEC distribution as a function of space and time. Since the main spatial ionospheric variations occur along the magnetic meridian, the keogram method is more appropriate for analyzing TEC time series as a function of magnetic meridian latitudes and fixed longitude.

In this regard, it is preferable to have TEC along geomagnetic meridians rather than in geographic coordinates. Some procedures and mathematical algorithms for calculating geomagnetic meridian lines were used to achieve these goals, as described in the following sections.

3.2.1 Conversion of geographic to geomagnetic coordinates

At low and middle latitudes, a magnetic dipole is a reasonable approximation for the geomagnetic field. The axial-centered dipole, for which the Earth's magnetic and rotational axes coincide, is the simplest approximation and expresses a geomagnetic vector. Figure 3.5 depicts the used angles and vector components of the geomagnetic field.

Figure 3.5 - A schematic of diagram showing the components of the geomagnetic field measurements $\vec{D}$: declination, $\vec{H}$: horizontal component, $\vec{Z}$: vertical component, $\vec{X}$: north-south component, $\vec{Y}$: east-west component, $\vec{F}$: total force, and $\vec{I}$: inclination.
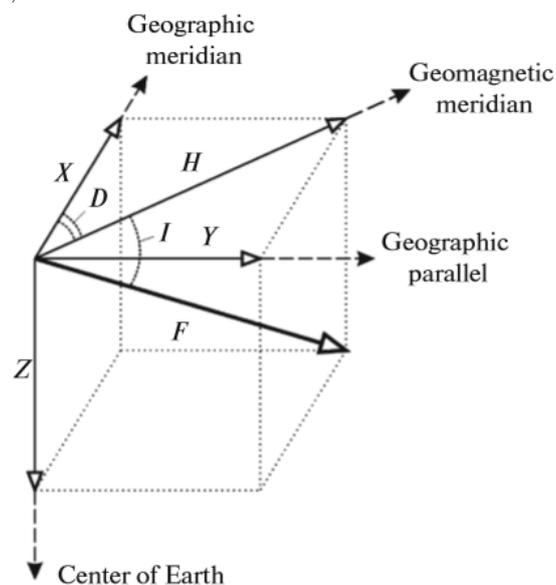
Source: Soloviev et al. (2012).

The relations between the different quantities, as presented in Figure 3.5, are given by (SCHUNK; NAGY, 2009):

$$H = \left(X^2 + Y^2\right)^{\frac{1}{2}} \tag{3.13}$$

$$D = \tan^{-1}\left(\frac{Y}{X}\right) \tag{3.14}$$

$$X = H\cos D \tag{3.15}$$

$$Y = H\sin D \tag{3.16}$$

$$F = \left(H^2 + Z^2\right)^{\frac{1}{2}} = \left(X^2 + Y^2 + Z^2\right)^{\frac{1}{2}} \tag{3.17}$$

$$I = \tan^{-1}\left(Z/H\right) = \tan^{-1}\left[Z/\left(X^2 + Y^2\right)^{\frac{1}{2}}\right] \tag{3.18}$$

F represents the magnitude of the geomagnetic field (the total field strength); H represents the magnitude of the horizontal field; and X, Y, and Z represent the cartesian components of F in the northward, eastward, and downward directions, respectively. The angle D is the declination, which is the deflection of the geomagnetic meridian from the geographic, and the angle I is the magnetic field's inclination or dip angle from the horizontal.

The magnetic dip latitude is calculated using the relation:

$$DipLat = atan\left(\left(\tan I\right)/2\right) \tag{3.19}$$

The International Geomagnetic Reference Model (IGRF) was used to convert geographic to magnetic coordinates (AERONAUTICS; (NASA)., 2019). Because the IGRF-Model computes the X, Y, and Z components of the F (geomagnetic field) for a given altitude, geographic latitude, and longitude, the corresponding declination and

dip latitude were calculated using Equation 3.14 and Equation 3.19, respectively.

The magnetic meridian lines, on the other hand, must be determined in order to interpolate the TEC values over them. By using spherical trigonometry formulas, the geographic longitude (ϕ) and latitude (θ) coordinates were employed as a reference location (as shown in Figure 3.6) for the magnetic meridian coordinates Λ and Θ, respectively.

Figure 3.6 - The magnetic meridian computation is depicted in a schematic diagram.
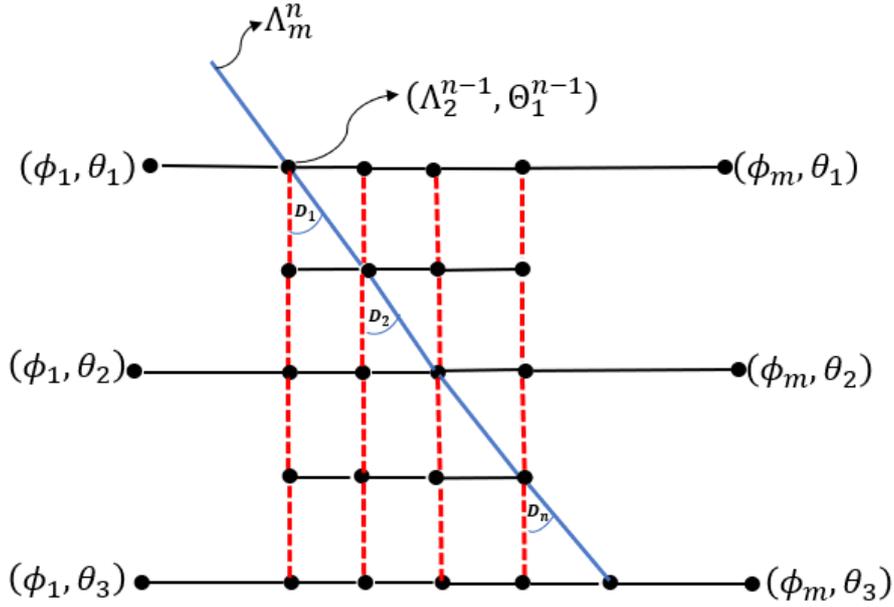
To calculate where the magnetic meridian crosses the map, the following equations were used:

$$\Lambda_m^n = \Lambda_m^{n-1} - \Delta\phi \tan\left(D\left(\Lambda_m^{n-1}, \Theta_m^{n-1}\right)\right) \tag{3.20}$$

where,

$$\Theta_m^n = \Theta_m^{n-1} - \Delta\theta \tag{3.21}$$

where Λ_m^n and Θ_m^n are the magnetic longitudes and latitudes ($n = 1,...,N$) across a given meridian ($m = 1,...,M$); $\Delta\theta$ is the latitude step; and $D\left(\Lambda_m^{n-1}, \Theta_m^{n-1}\right)$ is the

magnetic declination determined by the IGRF model.

Equation 3.20 and Equation 3.21 were used to determine the magnetic meridian line, which is illustrated in Figure 3.6. Using a $\Delta\theta = 1°$ and a 300 km altitude, each magnetic meridian line in Figure 3.7 was calculated.

Figure 3.7 - Geomagnetic meridian line (in blue) having an interval of 5°, over the South American continent. The red continuous line indicates the magnetic equator.
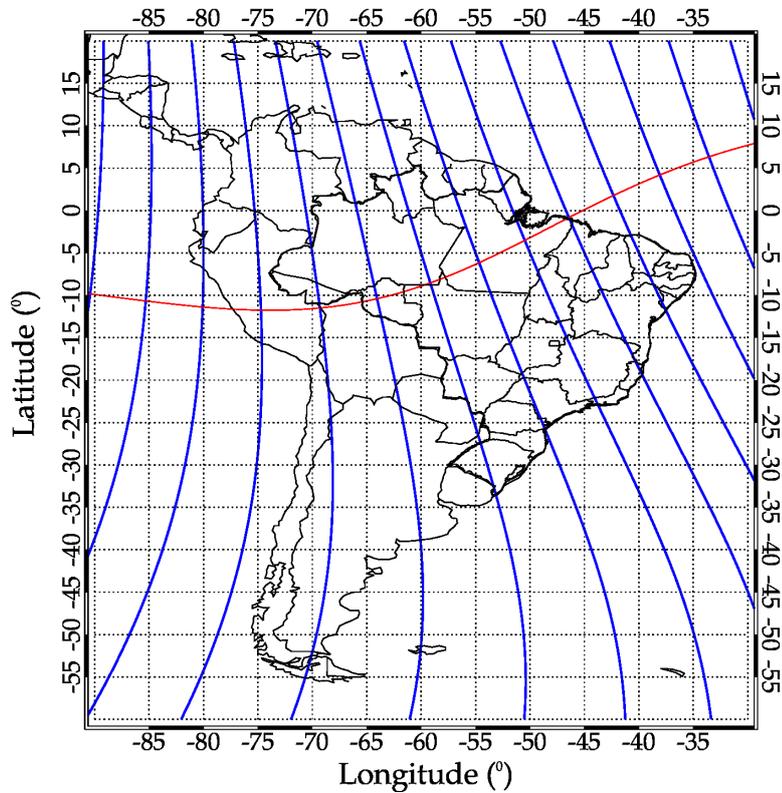
A bilinear interpolation approach was used to acquire TEC data along the magnetic meridian line, as illustrated in Figure 3.8 for a geomagnetic longitude of 7.58°E.

Figure 3.8 - GPS based TEC Map over South America in the night of November 01, 2014, at fixed time 00:00 UT. The continuos black line passing across map represents magnetic meridian line.
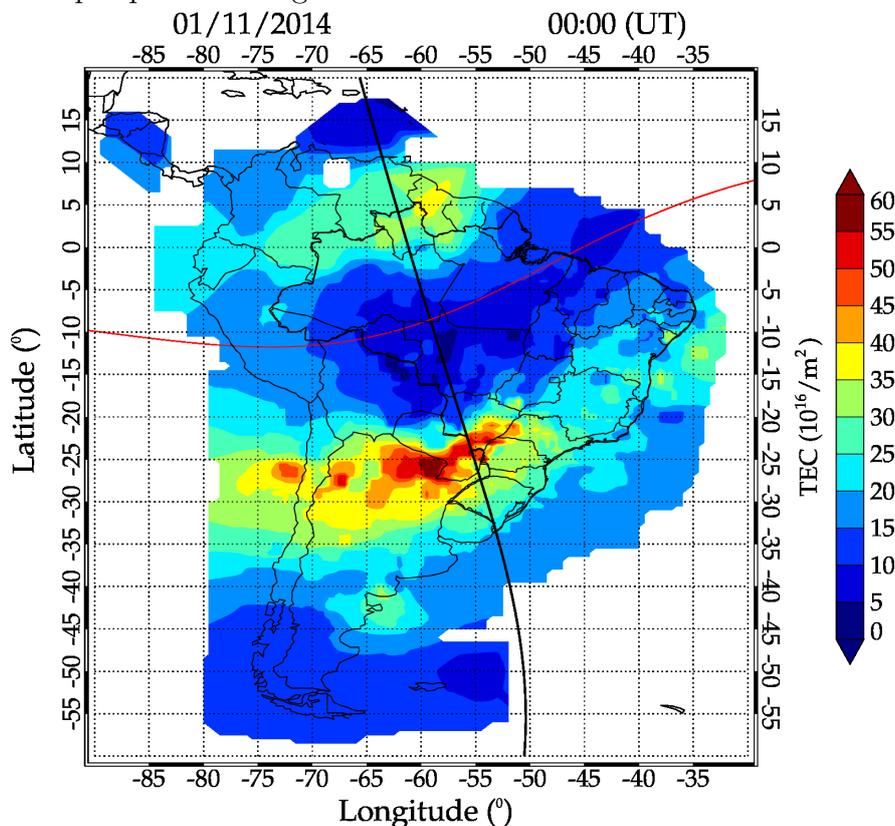
As a result, the cell size for the TEC grid map has an interval of 0.5°. The algorithm calculates the output TEC value based on where the meridian passes concerning the center of the grid pattern of the cells and the values associated with these cells. The output value is determined by interpolating the TEC values of the four closest input cell centers. The magnetic meridian, which runs through 293.5° in geographic longitude and 0.0° in geographic latitude (meaning Local Time (LT)= Universal Time (UT)-4.43), respectively. This meridian is located at magnetic longitude 7.58°E, according to the IGRF model.

Thus, the output cell's new TEC value is a weighted average of these four TEC values, adjusted for their distance from the center. The TEC map for November 1st, 2014 at 00:00 UT is depicted in Figure 3.8. The magnetic meridian, which is positioned at 7.58°E, is represented by the black line that runs across the map.

The bilinear approach is used to extract and interpolate TEC values from these line points traversing over the TEC map, and the result is displayed in Figure 3.9. The

48

plotted data demonstrate that the output agrees well with the points in Figure 3.8 where the magnetic meridian line of 7.58°E passes.

Figure 3.9 - TEC data from Figure 3.7 interpolated along the magnetic meridian line.
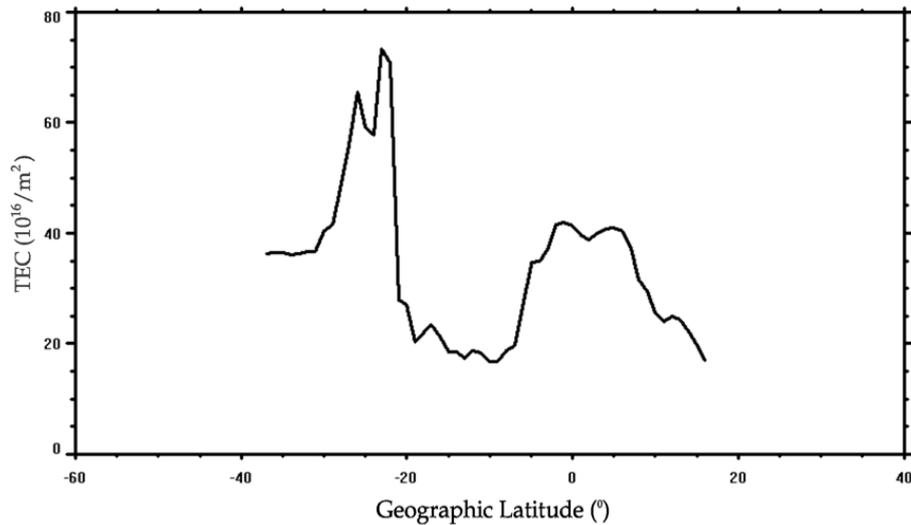
3.2.2 Construction of keogram from the TEC maps

Using the geomagnetic meridian line, keograms provide a well-organized way for finding the equatorial ionization anomaly crests (Figure 3.7). TEC data obtained along various magnetic meridian lines are used to create the keograms. An example of how the keogram is constructed using consecutive TEC maps in geographic coordinates is presented in Figure 3.10.

Figure 3.10 - Consecutive TEC maps used to construct a keogram.
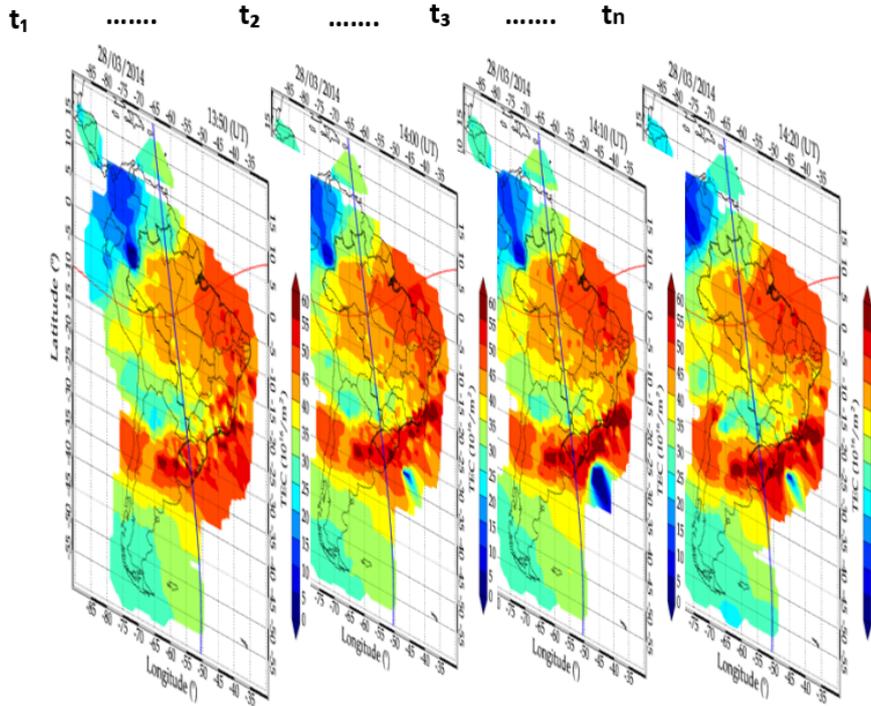
The morphology of the equatorial ionization anomaly crest in the northern and southern hemispheres can be observed using the keogram representation. For geomagnetic longitude 7.58°E and for the 28th of March, 2014, Figure 3.11 depicts one example of a keogram that is a function of geographic latitude and universal time (UT). Two prominent crests can be seen in the same figure, one above and one below the magnetic equator (red dash line).

Figure 3.11 - A Keogram for geomagnetic longitude 7.58°E and for the day 28th of March, 2014. The red dash line depicts the magentic equator.
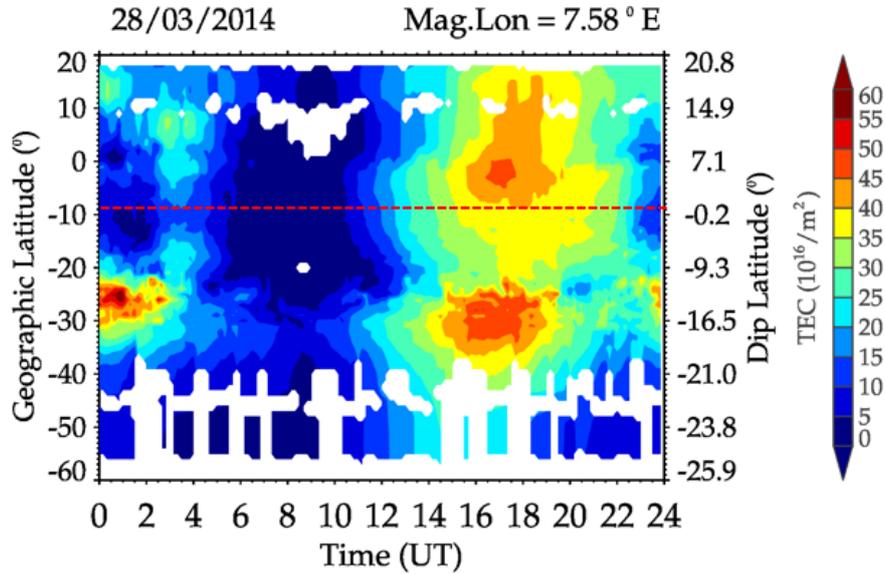
3.2.3 Keogram analysis to estimate EIA crest parameters

A keogram, as previously stated, is a helpful tool for estimating latitude positions, TEC values at crests, and EIA time occurrence within a day, month, or year. The anomaly start and end time formations and the equatorial ionization crests in both hemispheres can also be seen.

The basic information needed to characterize the EIA crests, such as intensity (in TECU), latitudinal positions, and occurrence times, were determined using an algorithm. The developed procedure uses two approaches to estimate the EIA crest positions. The first uses a 2D-Gaussian fit, whereas the second uses a method called the centroid function, which may be found online at (NATIONAL..., 2019). The following criteria were used to apply both methods:

a) Define the EIA crest position using the geomagnetic equator as a reference point.

b) In the keogram, define a Region of Interest (ROI) to look for EIA crests.

c) Calculate the EIA crests parameters.

The simulation shown in Figure 3.12 was used to assess the efficiency of two functions that were used to compute the EIA crest position, time of occurrence, and TEC

51

values. The blue and white stars indicate the 2D-Gaussian fit and the centroid function, respectively, and the results are the same for both methods.

Figure 3.12 - Comparison of Gaussian (blue star) and the Centroid functions (white star).
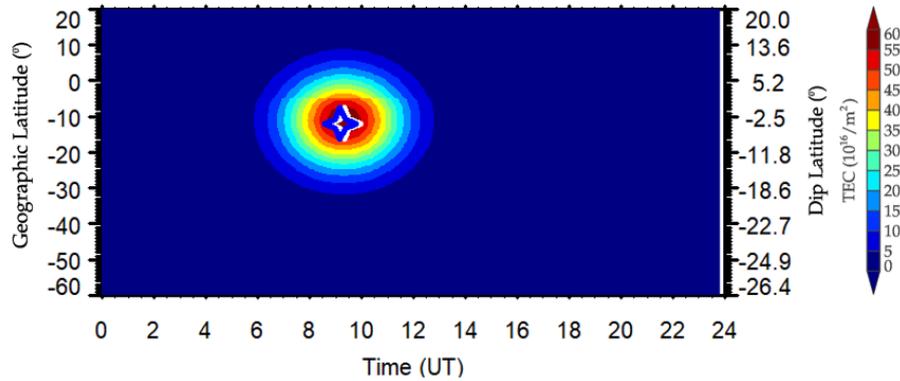
The procedure for locating the EIA crests positions at 7.58°E magnetic longitude is shown in Figure 3.13. The regions of interest in the keograms are chosen to locate both the northern and southern crest positions when they are available. The 2D Gaussian fit and centroid functions were then used, and the locations and EIA intensity were saved.

Figure 3.13 - An example of the analysis carried out on the keogram of March, 28, 2014 to obtain the northern and southern crests positions and intensity of the EIA, using the 2D-Gaussian fit (blue) and the Centroid (white) function.

52
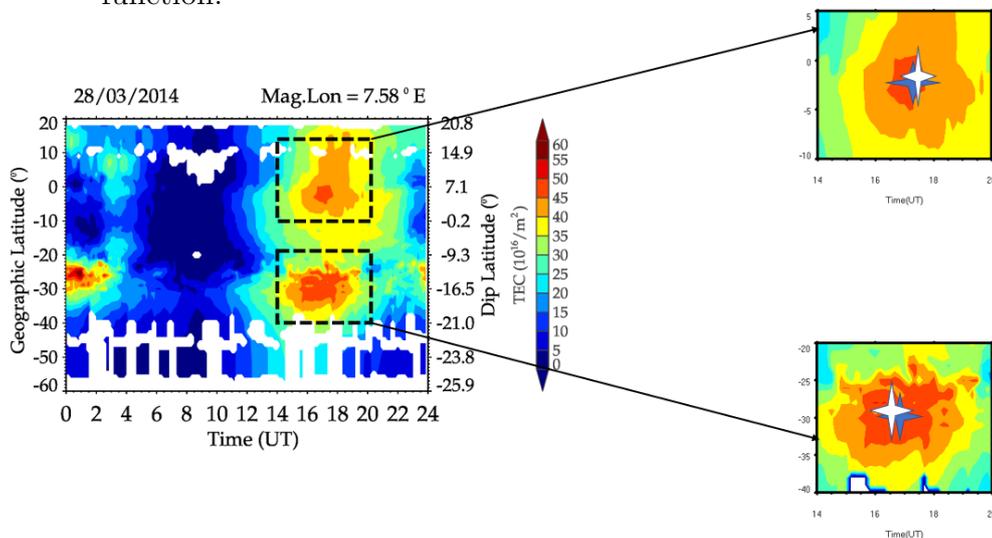
After that, the data is used to construct a time series of the EIA crest position at each magnetic longitude. In Figure 3.14, the positions of the EIA north and south crests as estimated by the two functions are displayed. The vertical bars reflect the error margins, while the blue and black dots represent the positions calculated by the 2D Gaussian fit and centroid functions, respectively.

Figure 3.14 - Northern and southern hemispheres EIA crests positions for March, 2014 calculated by the two different funtions.
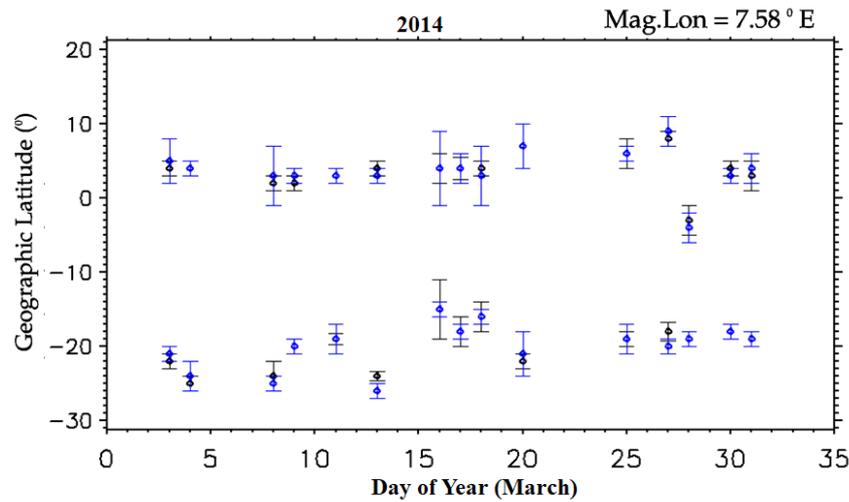
The crest shape of Figure 3.12 is perfect Gaussian; however, the crest shape of Figure 3.13 is not. As a result, as seen in Figure 3.13, the two functions did not define the same position. After a series of testing with both functions, the centroid function was chosen to represent the EIA crests parameters because it offered a more precise position crests compared to data than the 2D Gaussian fit. Because the Northern Hemisphere has fewer GNSS receivers, the data for such locations is less representative. As a result, the north crest analysis is less precise than the south crest analysis, with a broader receiver range. Thus, the north crest parameters were omitted during the analysis.

Figure 3.15 shows an example of the south crest positions, intensities, and the time occurrences calculated using the Centroid function for the magnetic meridian 7.58°E for the year 2014. The black scatter cross represents the original data and the continuous red line depicted the 5 points (i.e.,5 days) smoothed data.

Figure 3.15 - (a) Latitudinal (b) intensity and the (c) time of occurrences of the south EIA crest obtained by Centriod function.
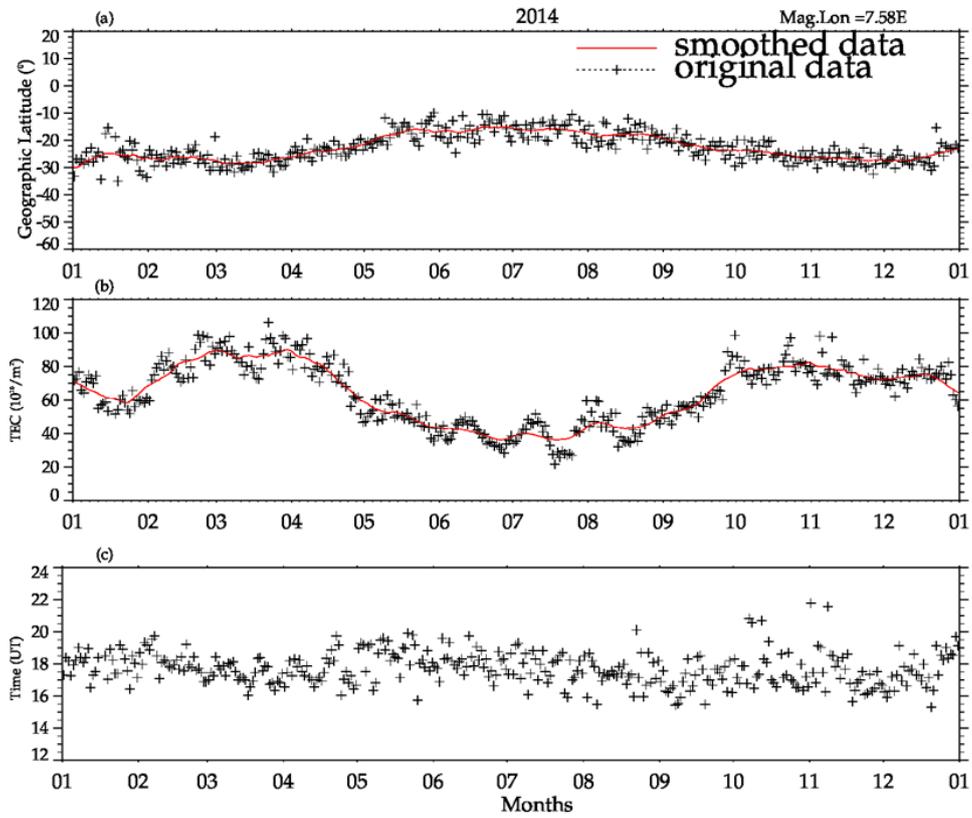
All of the procedures required to construct the TEC maps, keograms, and EIA crests parameters are depicted in the flowchart in Figure 3.16.

Figure 3.16 - The key steps for obtaining the EIA crests parameters are depicted in a flowchart.
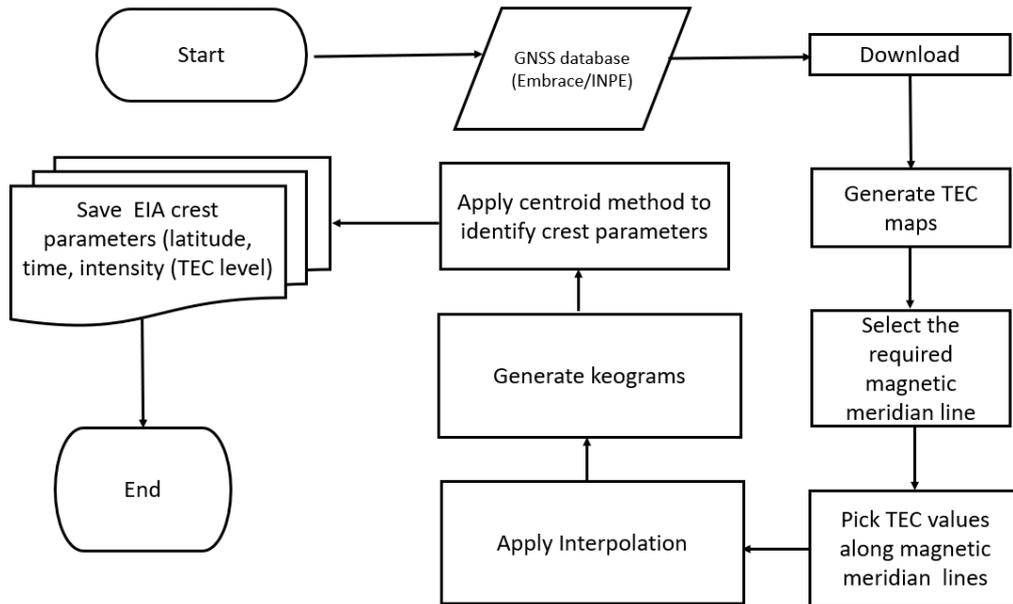
The top panel of Figure 3.17 depicts a typical monthly variation of EIA TEC intensities as a function the month and geographic/Dip latitude (left/right y-axis) at magnetic meridian (7.58°E) in the year 2014. The result was obtained by taking daily keograms (diurnal variation of TEC) and averaging the TEC between the time intervals 12:00-24:00 UT (the study was limited to daytime hours). Following that, a smoothing procedure was carried out for the entire year using 5 points (i.e., 5 days). The same procedure was used to determine the time of observation of the EIA crests. As shown in the bottom panel of Figure 3.17, the mean of the observation time was integrated over the latitudinal interval from 20°N to 60°S.

Figure 3.17 - Monthly averaged TEC along the magnetic meridian as a function of the month and geographic/Dip latitude (left/right y-axis) from January (1) to December (12) in 2014, along the magnetic meridian 7.58°E.
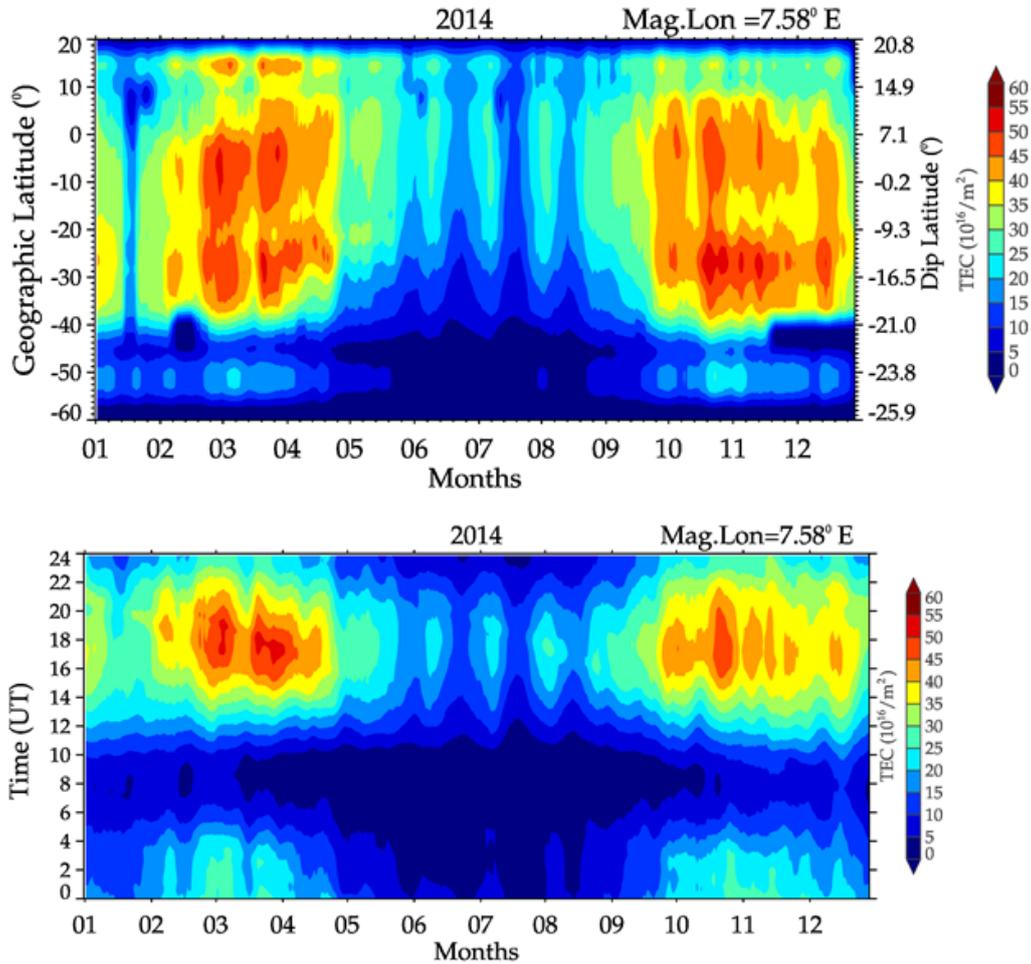
3.3 Spectral analysis technique

Using Lomb-Scargle periodogram or wavelet transform techniques, oscillations in the day-to-day variability of the southern EIA crest position can be identified. This section will provide a brief overview of these two time series methods.

3.3.1 Lomb-Scargle periodogram

The Lomb-Scargle technique is widely used in science, particularly in the analysis of astronomical data. It is typically used to identify periodicities in time series that are not sampled at constant time intervals and is based on the work of Lomb (1976), Scargle (1982) and Horne e Baliunas (1986).

The Lomb-Scargle (L-S) periodogram, which is used to estimate the contribution of a specific frequency ω to composing the entire signal for a time series $X(t_j)$, where $j = 1, 2, ..., N_0$ is the number of data samples, is defined as follows:

$$P_x = \frac{1}{2} \left\{ \frac{\left[\sum_{j=1}^{N_0} X_j \cos \omega(t_j - \tau) \right]^2}{\sum_{j=1}^{N_0} \cos^2 \omega(t_j - \tau)} + \frac{\left[\sum_{j=1}^{N_0} X_j \sin \omega(t_j - \tau) \right]^2}{\sum_{j=1}^{N_0} \sin^2 \omega(t_j - \tau)} \right\} \quad (3.22)$$

where the term τ is defined as :

$$\tan(2\omega\tau) = \frac{\left(\sum_{j=1}^{N_0} \sin 2\omega t_j \right)}{\left(\sum_{j=1}^{N_0} \cos 2\omega t_j \right)} \quad (3.23)$$

The definition of τ makes the periodogram equivalent to adjusting sine and cosine functions of a data set for a given frequency ω, using the least-squares method. In addition, the constant τ makes the periodogram invariant to a shift in the origin of time (LOMB, 1976). The main difference between L-S periodogram and Fourier analysis is that, while the latter weighs the data based on the interval between samples, the former weighs the data based on the points, estimating the sine and cosine components only when the data are sampled.

Although it is an advantageous method, given that many time series in science are not sampled at equal time intervals, there are some problems that, however, can be minimized. One is spectral leakage, which occurs when the spectral energy associated with a specific frequency ω_0 escapes to other frequencies due to the finite length of the data window and irregularities in data spacing (HORNE; BALIUNAS, 1986).

The spectral leakage that occurs from high to low frequencies is called aliasing. Horne e Baliunas (1986) suggested a procedure to minimize the problems due to spectral leakage in the L-S periodogram by subtracting a sinusoid from the original data, corresponding to the most significant peak in the periodogram. Then, a new periodogram is recalculated in which both peaks for the adjusted frequency and those due to spectral leakage should disappear. Thus, the remaining peaks must be due to signals present in the data.

As important as identifying the periodic variations in time series is assessing the confidence of the results obtained. In the case of the Lomb-Scargle periodogram, the confidence of the results can be assessed through the False Alarm Probability

(FAP) test. The application of the FAP tests the hypothesis that the analyzed signal consists of pure Gaussian noise and, therefore, no peak in the spectrum has energy above a certain level z_c. The FAP is defined by:

$$FAP = 1 - (1 - e^{z_c})^{n_i} \tag{3.24}$$

where n_i is the number of points in the analyzed series.

A peak is significant, with a level of confidence greater than P $(P = 1 - FAP)$, if the spectral energy exceeds a certain critical value z_c, is given by:

$$z_c = -\ln\left(1 - (1 - FAP)^{\frac{1}{n_i}}\right) \tag{3.25}$$

Lomb-Scargle periodogram analysis was used in the day-to-day measurements of the EIA southern crest position. A time series was constructed using the EIA crest position for each magnetic meridian shown in Figure 3.6 that crosses the South America continent. Figure 3.18 shows an example of the day-to-day southern crest positions of the EIA and the respective periodogram. The spectrum reveals the presence of oscillations around 2.5, 3, 5, and 9 days in the southern crest positions at 3.36°E (magnetic longitude). The short red dash line represents the significant level.

Figure 3.18 - (a) Time series generated from the daily EIA southern crests positions. (b) Lomb-Scargle periodogram of the EIA at 3.36°E (magnetic longitude) during 2015. The short red dash line indicates 90% of significance level.
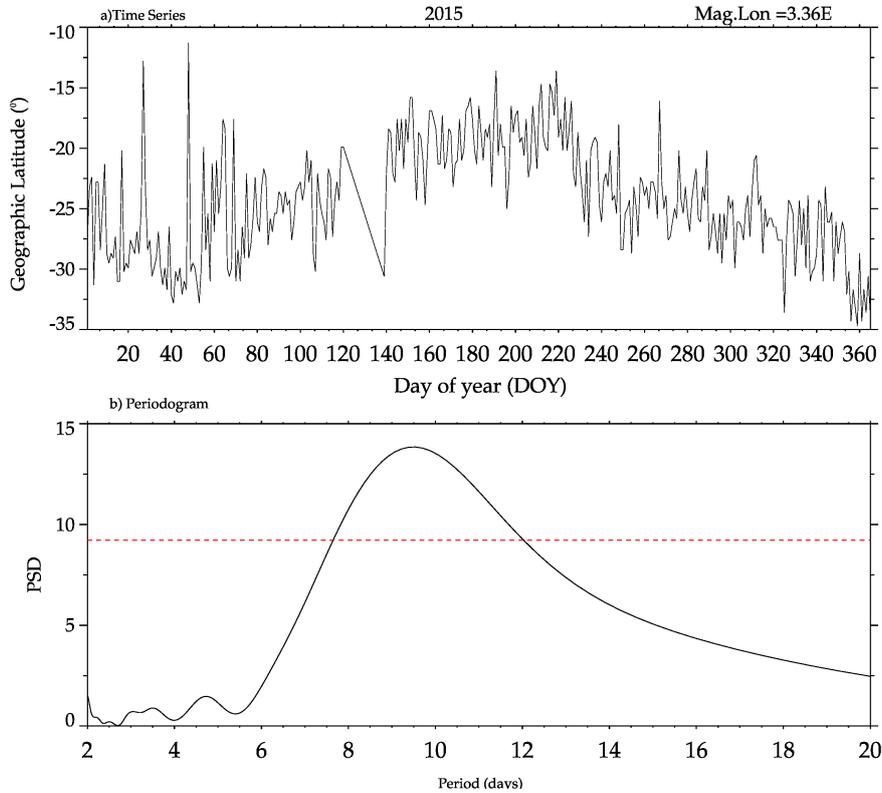
3.3.2 Wavelet Transform

The wavelet transform is an essential spectral analysis tool and is widely used in several branches of knowledge. The wavelet transform emerged from obtaining information about a time series that the traditional Fourier transform could not provide.

The windowed Fourier transform contains three parameters (position, scale, frequency), while the wavelet contains only two. However, the wavelet family is generated from a mother wavelet function $\psi(t)$ by translation and dilatations, and given by (FRICK et al., 1997):

$$\psi_{a,b}(t) = a^{-\frac{1}{2}} \psi\left(\frac{t-b}{a}\right) \tag{3.26}$$

where a and b represent the dilatation and the translation parameter, respectively. More importantly, there are specific requirements for the function $\psi(t)$ to be con-

sidered as a wavelet. For this reason, firstly the function must have a zero mean (i.e., the admissibility condition) defined as:

$$\int_{-\infty}^{\infty} \psi(t)\, dt = 0 \tag{3.27}$$

Secondly, the function should be localized in both physical and Fourier spaces (time and frequency), i.e., its time spread Δt, and its frequency spread $\Delta \omega$ must satisfy the $\Delta t \Delta \omega = const > 2\pi$. Additionally, at least one reconstruction formula is required to reconstruct the signal from its wavelet coefficients and deduce the energy.

The continuous wavelet transform $w(a,t)$ of signal $f(t)$ is defined as:

$$w(a,t) = C_\psi^{-1/2} a^{-1/2} \int_{-\infty}^{\infty} \psi^* \left(\frac{t'-t}{a} \right) f(t')\, dt', \tag{3.28}$$

where $\psi(t)$ is a real or complex-valued analyzing wavelet, satisfying condition of stated in Equation 3.27 and * indicate the complex conjugate.

$$C_\psi = \int_{-\infty}^{\infty} |\omega|^{-1} \left| \widehat{\psi}(\omega) \right|^2 d\omega \tag{3.29}$$

and $\widehat{\psi}(\omega)$ is the Fourier Transform of $\psi(t)$

$$\widehat{\psi}(\omega) = \int_{-\infty}^{\infty} \psi(t)\, e^{i\omega t} dt \tag{3.30}$$

One important property is the global wavelet spectrums. The energy contained in all wavelet coefficients of the same scale a is a function of a given as:

$$M(a) = \int |w(a,t)|^2\, dt, \tag{3.31}$$

which is related with Fourier spectrum $E(\omega) = \left| \widehat{f}(\omega) \right|^2$ as:

$$M(a) \sim \int E(\omega) \frac{\left| \widehat{\psi}(a\omega) \right|^2}{a}\, d\omega \tag{3.32}$$

60

and is a smoothed version of the Fourier Spectrum. However, due to the normalization defined in Equation 3.28, if the Fourier spectrum follows a power law $E(\omega) \sim \omega^{\alpha}$, the global power spectrum displays the same power-law ($M(a) \sim a^{\alpha}$), as long as the wavelet presents enough cancellation (PERRIER et al., 1995).

There are currently several routines available for working with wavelet transform analysis. For example, the Interactive Data Language (IDL) software used in this work generates routines that allow data analysis using the wavelet transform.

The wavelet transform, on the other hand, was computed using the package of routines developed by Torrence e Compo (1998a). The package's routines are freely available on the internet (TORRENCE; COMPO, 1998b) and were developed to study ocean temperature variations associated with the El Niño phenomenon.

The routine package allows you to compute the wavelet transform with various types of mother wavelets. The analyses in this paper made use of Morlet's mother wavelet, which has the shape of a plane wave modulated by an exponential and is defined by (TORRENCE; COMPO, 1998a):

$$\psi_0(\eta) = \pi^{-\frac{1}{4}} e^{i\omega_0 \eta} e^{-\frac{\eta^2}{2}} \tag{3.33}$$

where ω_0 represents a dimensionless frequency and η represents a dimensionless time parameter This function should be normalized, as indicated by the superscript (ψ_0). Normalization ensures that the transformed values in each scale s are directly comparable with each other and the transformed values in other series (TORRENCE; COMPO, 1998a).

The normalization details can be found in Torrence e Compo (1998a). Once the wavelet has been selected, the scales to be analyzed must be chosen. The scales can be written as fractions of powers of 2 (TORRENCE; COMPO, 1998a). As a result, we have:

$$s_j = s_0 2^{j\delta_j}, ...j = 0, 1, ..J \tag{3.34}$$

$$J = \delta^j_{-1} log_2 (N\delta t/s_0) \tag{3.35}$$

where s_0 is the smallest resolvable scale, J determines the largest scale and δ_j is the spacing between the scales. The smaller δ_j, the better the resolution of the analysis. However, this will occur at the expense of more computing time. For Morlet's mother wavelet, the highest δ_j which still provides a good analysis resolution is $\delta_j = 0.5$ (TORRENCE; COMPO, 1998a).

The day-to-day estimation of the south hemispheric EIA crest positions allowed to identify signatures of oscillations with periods ranging from 2 and 16 days. These signatures are identified by submitting the time series to a Morlet wavelet spectral analysis. It is important to mention some advantages and disadvantages of using the wavelet transform to identify the oscillations in the EIA southern crest daily geographical latitude positions.

Since all data over a year is represented in the same spectrum, the primary advantage is identifying the oscillation's temporal locations. On the other hand, the wavelet application requires that the analyzed data and time series be spaced regularly. As a result, the time gap between days when no data is found must be filled; in this case, a linear interpolation procedure was used.

Figure 3.19 and Figure 3.19 show the day-to-day variation of southern EIA crest positions (top), (middle) Morlet wavelet power spectrum, and (bottom) amplitude of a 3-16 day filtered signal for a period of 2 to 16 days of the southern EIA crest in 2014 for the magnetic meridian (7.58°) and magnetic meridian (11.99°E) as a function of day of the year (DOY).

Figure 3.19 - Time series, wavelet power spectrum and amplitude of a 3-16 day filtered signal of the southern EIA crest positions at the magnetic meridian (7.58°E) (top) from January (DOY 1) to December (DOY 365) in 2014. The color shade shows spectral power density. The regions enclosed with the black lines depicts the 90% confidence levels.
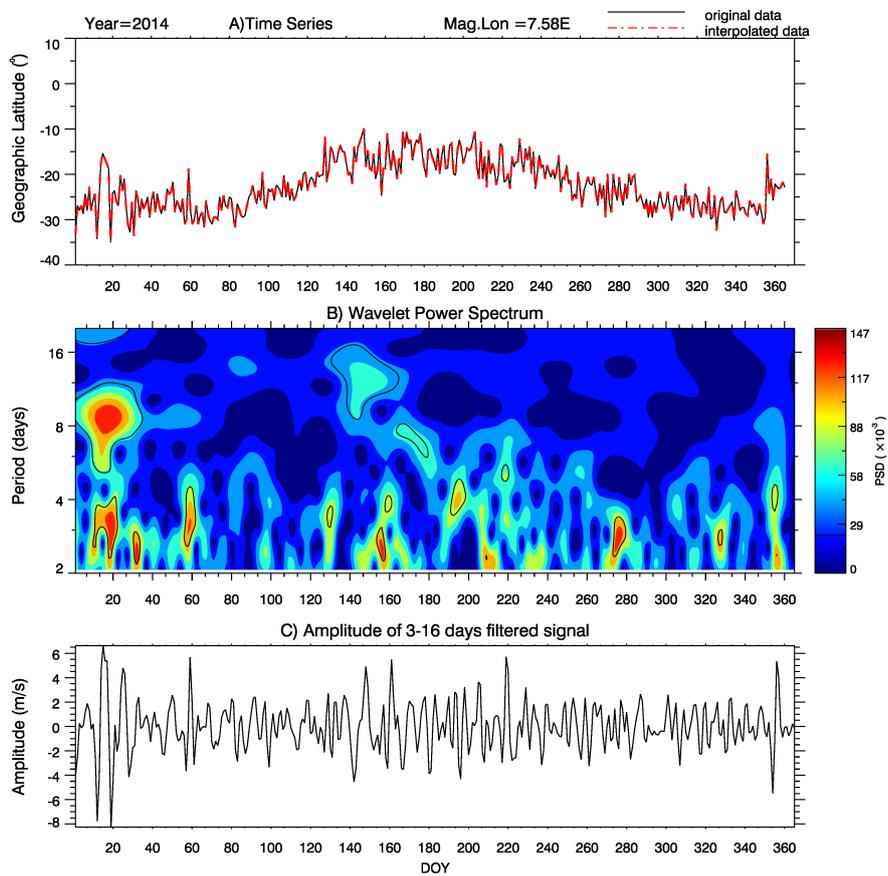
Figure 3.20 - Time series, wavelet power spectrum and amplitude of a 3-16 day filtered signal of the southern EIA crest positions at the magnetic meridian (11.99°E) in 2014. The color shade shows spectral power density. The regions enclosed with the black lines depicts the 90% confidence levels.
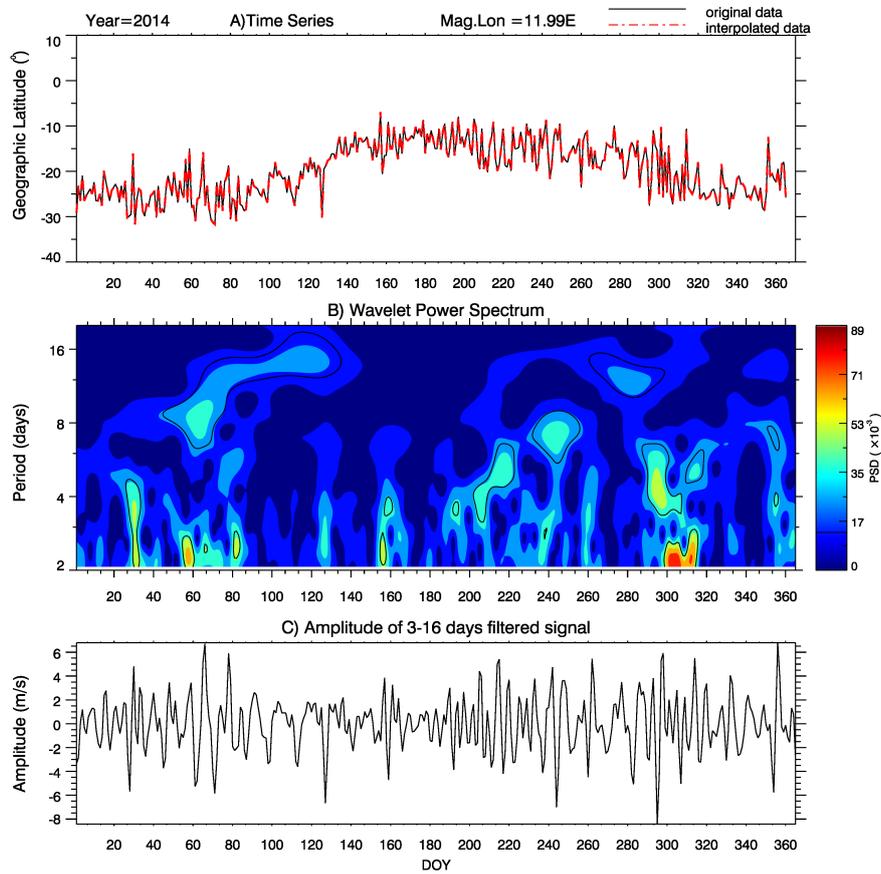
The power spectrum for the magnetic meridian (7.58°) shows several types of wave packets ranging from 2 to 16 days. Around days 0-20, the strongest oscillation with a period of 8 day can be seen. Besides, for the power spectrum for the magnetic meridian (11.99°E) in Figure 3.20, the most prominent oscillations have periods of 2-4 day occuring at day of the year 60, 135 and 4-6 day at days 220.

3.3.3 Cross-wavelet transform

A cross-wavelet transform is used to look for common period oscillations between two time series. The cross wavelet transform of two time series X and Y with wavelet transforms $W_n^X(s)$ and $W_n^Y(s)$, where n is the time index and s is the scale, the cross spectrum is defined as (TORRENCE; COMPO, 1998a):

$$W_n^{XY}(s) = W_n^X(s) W_n^{Y*}(s) \qquad (3.36)$$

where $(*)$ represents the complex conjugate. The cross-wavelet spectrum accurately decomposes the Fourier co- and quadrature-spectra into time scale space.

The wavelet squared coherency is defined as the absolute value squared of the smoothed cross-wavelet spectrum, normalized by the smoothed wavelet power spectra as:

$$R_n^2 = \frac{\left| < s^{-1} W_n^{XY}(s) > \right|^2}{< s^{-1} |W_n^X(s)|^2 > < s^{-1} |W_n^Y(s)|^2 >}, \qquad (3.37)$$

where $<>$ indicates smoothing in both time and scale; in the numerator, both real and imaginary parts of the cross-wavelet spectrum are smoothed separately before taking the absolute value. In the denominator, it is the wavelet power spectra (after squaring) that are smoothed. Finally, it is noted that because the wavelet transform conserves variance, the wavelet coherency is an accurate representation of the (normalized) covariance between the two series.

The wavelet-coherency phase difference is given by:

$$\phi_n(s) = \tan^{-1} \left(\frac{\Im\left\{ < s^{-1} W_n^{XY}(s) > \right\}}{\Re\left\{ < s^{-1} W_n^{XY}(s) > \right\}} \right). \qquad (3.38)$$

Where the smoothed real ($\Re$) and imaginary ($\Im$) are calculated in Equation 3.36. Both R_n^2 and ϕ_n are functions of the time index n and the scale s. The smoothing in Equation 3.36 and Equation 3.37 is done using a weighted running average (or convolution) in both the time and scale directions.

As a result, these algorithms were applied to the two time series (i.e., X and Y), which are represented by magnetic meridians of 11.9°E and 7.58°E, respectively.

Figure 3.21 depicts (A-C) time series plots with some common periods using the cross wavelet and coherence transform techniques. Common oscillations between both meridians can be seen in the cross wavelet spectrum.

A band-pass filter procedure can be used to estimate the amplitudes of the observed oscillations. The amplitude of the oscillations between 2-8-days is shown in Figure 3.21 (C). Furthermore, amplitude variations from the filtered oscillations can be seen. Also, the magnetic meridian 7.58°E lags behind the 11.9°E line, indicating a phase difference between the common oscillation detected at both meridians illustrated in Figure 3.21(D).

Figure 3.21 - (A) Time series, cross wavelet transform (B), Amplitudes (C) and (D) the phase differences of the latitudinal southern crest positions of the EIA for the magnetic meridians 7.58°E and 11.99°E during 2014.
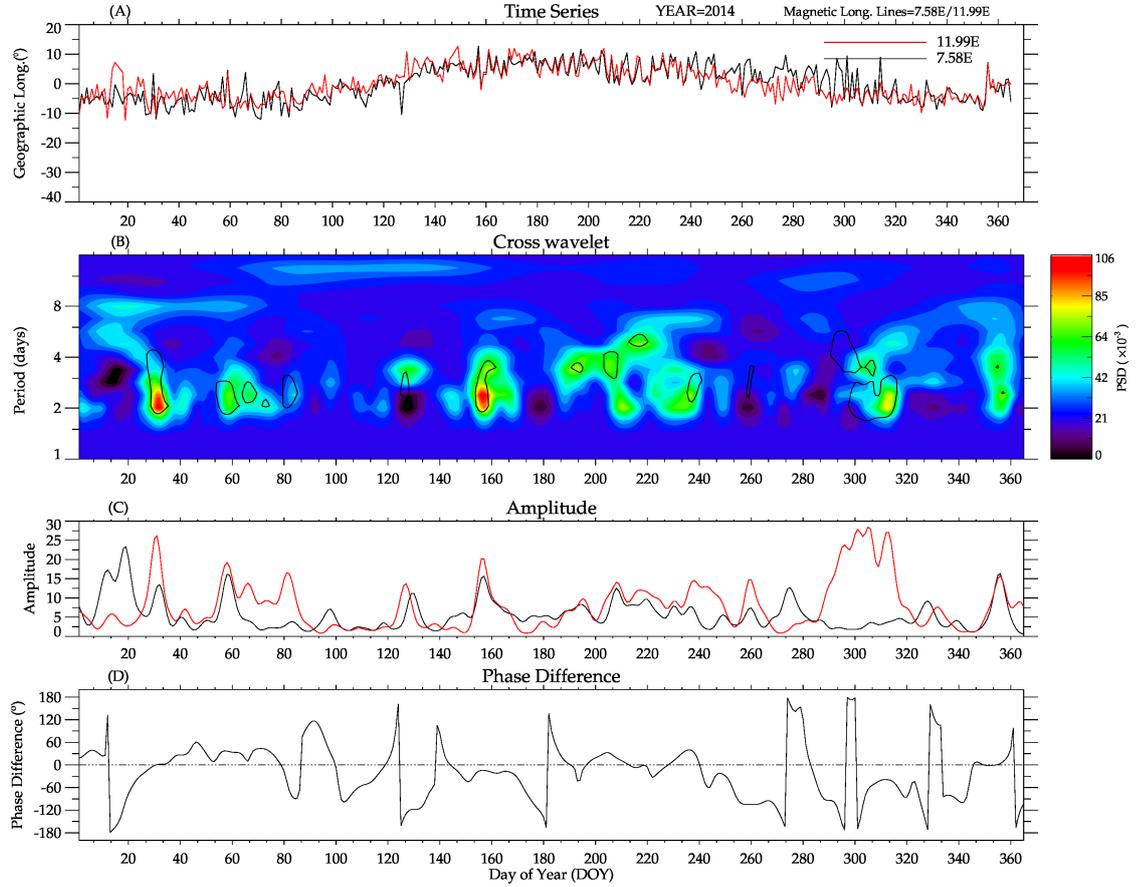
In addition, Table 3.2 displays common periods estimated using the Cross wavelet and coherency transform.

Table 3.3 - Main common periods and their occurrences estimated using the Cross wavelet and coherency transform techniques.

Period (day)	DOY
2-3	20-40
2-3	60-80
3	120-130
4	180-200
2	200-220
2	220-240
2,3	300-320
2-4	340-360

67

3.4 The SUPIM-INPE model

This section will briefly describe the Sheffield University Plasmasphere Ionosphere Model at Instituto Nacional de Pesquisas Espaciais (SUPIM-INPE).

In the 1960s, the first mathematical models appeared. Because of advances in computational capacity, these models have improved since then. As a result, more detailed studies on the variable nature of the equatorial and low-latitude ionosphere-thermosphere systems have been conducted. The SUPIM-INPE model was used for this work to quantify the physical and chemical processes of the upper terrestrial ionosphere required to develop the proposed study. It should be noted that the SUPIM-INPE model version differs from the SUPIM version in some ways, such as the calculations for region E (SANTOS, 2005) that were not included in the original version.

The SUPIM-INPE model realistically reproduces the behavior of the equatorial region and low latitude regions. Along the closed magnetic field lines, the equations of continuity, movement, and energy balance are solved. Thus, the values of electron and ion concentration, velocity aligned with the field, and temperature can be obtained (BAILEY; BALAN, 1996). In this model, the magnetic field is represented by an eccentric dipole, which is defined mathematically by the first eight non-zero terms of expanding the harmonics of the geomagnetic scalar potential, with coefficients obtained from the International Geomagnetic Reference Field (IGRF) geomagnetic field model. This model can be adapted for a dipole centered on the Earth's rotation axis or a centered dipole whose axis is tilted, respectively, truncating the expansion of spherical harmonics after the first or third non-zero term.

3.4.1 Equations solved by SUPIM-INPE

According to Bailey et al. (1997), the main dynamic and photochemical processes considered in SUPIM, which were maintained in the SUPIM-INPE version. It includes ionic production due to solar radiation, production and losses caused by chemical reactions between ions and neutral constituents, thermal and ambipolar diffusions, ion-ion and ion-neutral collisions, thermospheric winds, plasma drift, photoelectric conduction, friction heating, and local heating and cooling.

In this way, several equations are introduced in the model to represent all these chemical and physical processes. These equations will be presented below following the same description made by Bailey e Balan (1996).

- **Continuity equation**

The continuity equation for the i-th ion is given by:

$$\frac{dN_i}{dt} = P_i - L_i - \nabla \cdot (N_i \vec{\nu}_i),$$

(3.39)

where N_i is the concentration of the ions, t is the time, i is ion velocity, P_i is ion production rate, and L_i is ion loss rate. Considering the variations along the field lines, Equation 3.39 can be rewritten as:

$$\frac{dN_i}{dt} + \frac{1}{A}\frac{\partial \left(AN_i\nu_i^{\parallel}\right)}{\partial s} = P_i - \beta_i N_i - N_i \nabla \left(\vec{\nu}_{em}\right),$$

(3.40)

where A is the cross-sectional area of the plasma tube, $\nu_i^{\parallel}$ is the velocity of the ions aligned to the field, s is the distance along the magnetic field line, β_i is the coefficient of the ionic loss rate and in ν_{em} is the drift velocity.

- **Equation of motion**

The equation of motion for the i-th ion is solved separately for atomic and molecular ions. The equation for ions O^+, H^+ and He^+ includes the terms of thermal diffusion as stated in the equation below:

$$
\begin{aligned}
0 = -g\sin I &- \frac{kT_i}{m_i N_i}\frac{\partial N_i}{\partial s} - \frac{KT_e}{m_i N_e}\frac{\partial N_e}{\partial s} - \frac{k}{m_i}\frac{\partial (T_e + T_i)}{\partial s} \\
&+ \frac{k}{m_i}\left[-\beta\frac{\partial T_i}{\partial s} + \beta_{ij}^*\frac{\partial T_j}{\partial s} + \beta_{ik}^*\frac{\partial T_k}{\partial s}\right] \\
&- [v_{ij}(1-\Delta_{ij}) - R_{ijk} + R_{ikj}]\left(v_i^{\parallel} - v_j^{\parallel}\right) \\
&- [v_{ik}(1-\Delta_{ik}) - R_{ikj} + R_{ijk}]\left(v_i^{\parallel} - v_k^{\parallel}\right) \\
- \sum_m v_{im}\left(v_i^{\parallel} - v_m^{\parallel}\right) &- \sum_n v_{in}\left(v_i^{\parallel} - u_\theta\cos D\cos I + u_\phi\sin D\cos I\right),
\end{aligned}
$$

(3.41)

where g is the acceleration due to gravity; k is the Boltzmann constant; m_i is the mass of the ion; T_i is the ion temperature; T_e is the temperature of the electrons; N_e is the electronic concentration; v_{im} is the collision frequency for moment transfer

between the i-th ion and the m-th molecular ion; ν_{in} is the collision frequency for moment transfer between the i-th ion and the n-th neutral gas; u_θ is the meridional component of the neutral wind (positive from north to south) in the geographic coordinate system; u_ϕ is the zonal component of the neutral wind (positive from west to east) in the geographic coordinate system; $v_i^\parallel$ is the speed of the i-th ion aligned to the field; D is the magnetic declination angle (positive to the east); I is the angle of magnetic inclination; $\beta_i, \beta_{ij}^*, \beta_{ik}^*$ are the thermal diffusion coefficients; $\Delta_{ij}, \Delta_{ik}, R_{ijk}, R_{ikj}$ are the correction factors for the diffusion coefficient of the i-th ion.

The values of these coefficients can be found in Quegan et al. (1981). The sum $\sum_m$ is performed over all ions and the sum $\sum_n$ is performed over all neutral gases. When, $i = O^+$, then $j = H^+$ and $k = He^+$; When $i = H^+$, then $j = O^+$ and $k = He^+$ and finally when $i = He^+$, then $j = H^+$ and $k = O^+$.

The equation of motion for molecular ions (NO^+, O_2^+ and N_2^+) is given by:

$$
\begin{aligned}
0 = {} & -g \sin I - \frac{kT_i}{m_i N_i} \frac{\partial N_i}{\partial s} - \frac{kT_e}{m_i N_e} \frac{\partial N_e}{\partial s} - \frac{k}{m_i} \frac{\partial (T_e + T_i)}{\partial s} \\
& - \sum_{j \neq 1} \left(v_i^\parallel - v_j^\parallel \right) - \sum_n v_{in} \left(v_i^\parallel - u_\theta \cos D \cos I + u_\phi \sin D \cos I \right),
\end{aligned}
\tag{3.42}
$$

where the sum $\sum_{j \neq i}$ is calculated on all ions except the i-th.

For electrons, it is assumed that charge neutrality is preserved, that is:

$$
N_e = \sum_i N_i,
\tag{3.43}
$$

and that there are no currents aligned to the field, that is:

$$
N_e v_e = \sum_i N_i v_i^\parallel,
\tag{3.44}
$$

In Equation 3.44, v_e refers to the speed of electrons aligned to the field, and $\sum_i$ denotes the sum for all ions.

- **Energy balance equation**

The energy conservation equation solved by SUPIM-INPE for ions and electrons is given by:

$$\frac{3}{2}kN_i\left(\frac{\partial T_i}{\partial t} + v_i^{\|}\frac{\partial T_i}{\partial s}\right) = Q - KN_iT_i\left(\frac{1}{A}\frac{\partial Av_i^{\|}}{\partial s}\nabla\cdot\vec{v}_{em}\right)$$
$$+\frac{1}{A}\frac{\partial}{\partial s}\left(Ak_i\frac{\partial T_i}{\partial s}\right) + F_{in} \tag{3.45}$$

where index i refers to ions and electrons, Q_i is the collisional rate heating, k_i is the thermal conductivity. F_{in} is the frictional heating rate due to the relative movement between the i-th ion and the neutral constituents and can be calculated with the following expression:

$$F_{in} = \sum_n \frac{m_i m_n}{m_i + m_n}\nu_{in}N[\left(v_i^{\|} - u_\theta\cos D\cos I + u_\phi\sin D\cos I\right)^2$$
$$+\left(\nu^\perp - u_\theta\sin D\sin I + u_\phi\cos D\sin I\right)^2 + \left(\nu^\phi\right)^2] \tag{3.46}$$

In Equation 3.46, m_n is the mass of the n-th neutral constituent, and the sum is made for all neutral constituents. The heating term referring to the relative movement between ions and neutrals was neglected since its value is negligible compared to the other terms in the equation. The energy conservation equation for molecular ions is not included in the model, and its temperatures are considered equal to that of the ion O^+.

3.4.2 Solution of model equations

The SUPIM-INPE model equations are solved numerically for each ion, considering that the movement of the ionospheric plasma follows an ambipolar diffusion in the direction parallel to the magnetic field lines, and with an additional drift $\vec{E}\times\vec{B}$ perpendicular to these lines.

Such equations were formulated for a dipole magnetic field line in terms of the coordinates L, s and t, where s is the distance along the magnetic field line, t the time, and $L = R_{eq}/a$ being R_{eq} the equatorial radial distance of the geomagnetic field line

and a the radius of the Earth. However, these coordinates are not orthogonal, and working with them when $\vec{\nu}_{em}$ and $\vec{E} \times \vec{B}$ non-zero introduces unnecessary mathematical complications. Therefore, to facilitate the calculations, it is necessary that the coordinates (L, s, t) are transformed to the coordinates (p, q, t) according to Kendall (1962), where p and q are given by:

$$p = \frac{R}{a \sin^2 \Theta} \tag{3.47}$$

and

$$q = \frac{a^2 \cos \Theta}{R} \tag{3.48}$$

In Equation 3.47 and Equation 3.48, the coordinates R and Θ are the radial distance from the center of the Earth and the colatitude, respectively. This transformation has two key properties: 1) The coordinate p is constant along the line of the dipole magnetic field $(P = L)$, and 2) the constant q is orthogonal to the field lines for a certain length. In addition, for a dipole magnetic field line, (BAILEY; SELLEK, 1990):

$$R = R_{eq} \sin^2 \Theta \tag{3.49}$$

and

$$\frac{\partial}{\partial s} = -\frac{(1 + 3 \cos^2 \Theta)^{0.5}}{a} \left(\frac{a}{R}\right)^3 \frac{\partial}{\partial q} = \eta \frac{\partial}{\partial q} \tag{3.50}$$

Applying this transformation of coordinates to the equations of continuity, movement, and energy balance and using the finite difference method, the SUPIM-INPE model equations are numerically solved. More information on the solution of the equations applied to SUPIM-INPE can be found in (BAILEY; BALAN, 1996; SOUZA, 1997).

3.4.3 Model input and output parameters

The main input parameters used by the SUPIM-INPE model are solar flow, information about the neutral atmosphere, neutral winds, and electromagnetic drift speed. Moreover, additional information must be given, such as the day, year, Ap index, latitude, and geographic longitude.

The solar flow data used in the SUPIM-INPE version for this study were obtained

from the Extreme Ultra Violet flux model for Aeronomic Calculations (EUVAC) (FENNELLY et al., 1994). The flux for the x-rays and lyman-α were taken from the model SOLAR2000 (TOBISKA et al., 2000). This model has a good representation for photoionization of region E and region F, thus, accurately characterizing the variability of solar radiation across the ionizing spectrum. To represent the neutral atmosphere, the model NRLMSISE-00 (PICONE et al., 2002) was used so that the concentrations of neutral gases O, H, He, O_2, N_2, and temperature (T_n) could be obtained. The concentration of nitric oxide (NO) is calculated separately according to Mitra (1968):

$$n\left(NO\right) = 0.4 exp\left(\frac{-3700}{T_n}\right) n\left(O_2\right) + 5.10^{-7} n\left(O\right). \tag{3.51}$$

The neutral wind speed, also used as an input for the SUPIM-INPE model, is obtained by the thermospheric wind model HWM93 (HEDIN et al., 1996). This model is based on satellites and radar observations and provides the meridional and zonal components of the neutral wind as a function of local time, altitude, latitude, longitude, and solar activity.

Finally, another input parameter of great importance in the SUPIM-INPE model is the ionospheric vertical drift. This study simulated the events based on the day and night drift data registered at Jicamarca Radio Observatory near Lima, Peru. In the absence of data obtained, the vertical drift used was that obtained by the empirical model proposed by Scherliess e Fejer (1999).

Once the model is prepared to simulate the ionospheric parameters for a given day, the user can obtain and choose several outputs. For example, the concentrations and temperatures of electrons and ions as a function of time, latitude, and altitude; the densities of the E and F regions, the height of the peak of the F region, and the Pedersen and Hall conductivities of the E and F regions integrated along the field lines.

4 RESULTS

This chapter will describe the current work's results for day-to-day, month-to-month, and annual variations of the EIA along different magnetic meridians from 2014 to 2019. The map of Southern America and magnetic meridian lines used to analyze the characteristics of the EIA crests are shown in Figure 4.1. The magnetic meridian lines crossing at 70°, 65°, 60°, 55°, 50°, 45°, 40° W geographic longitude at 5°S. In the following, the north and south hemispheres will be referred to as NH and SH, respectively.

Figure 4.1 - South America map showing the magnetic meridian lines used to study the EIA over the continent. Magnetic meridians of 0.22°W, 3.36°E, 7.58°E, 11.99°E, 16.61°E, 21.50°E, and 26.70°E are depicted in each box at the top of the map.
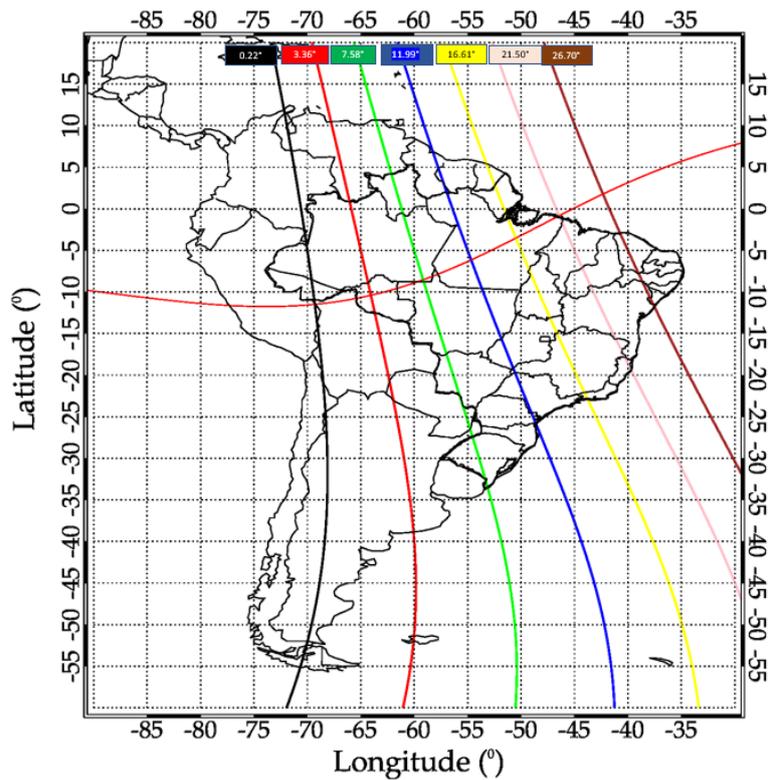
4.1 EIA day-to-day and month-to-month variabilities

The formation of the anomaly exhibits diurnal variation patterns, with the EIA crests becoming more intense gradually after they appear in the morning, reaching their peak in the afternoon, and then gradually fading away, sometimes during the

night. These characteristics of EIA development are found in all magnetic meridian lines (Figure 4.1) considered in this work.

The diurnal variation of the latitudinal ionization distribution was found to have two distinct features. The first is a typical EIA formation, with clear anomaly crests at low latitudes and less plasma density above the magnetic equator, resulting in a trough region. The ionization is concentrated near the magnetic equator and decreases towards low latitudes when the EIA is not formed. The top and bottom panels of Figure 4.2 depict these two prominent features.

Figure 4.2 - Diurnal variation of EIA formation as function of time (UT) and geographic/geomagnetic latitude (left/right y-axis) on August 12, when the EIA is developed showing two crests (top panel), and 21, when there is no EIA formation, in 2014. The colour shade represents TECU from 0 (blue) to 60 (red). The red dash line depicts the magnetic equator.
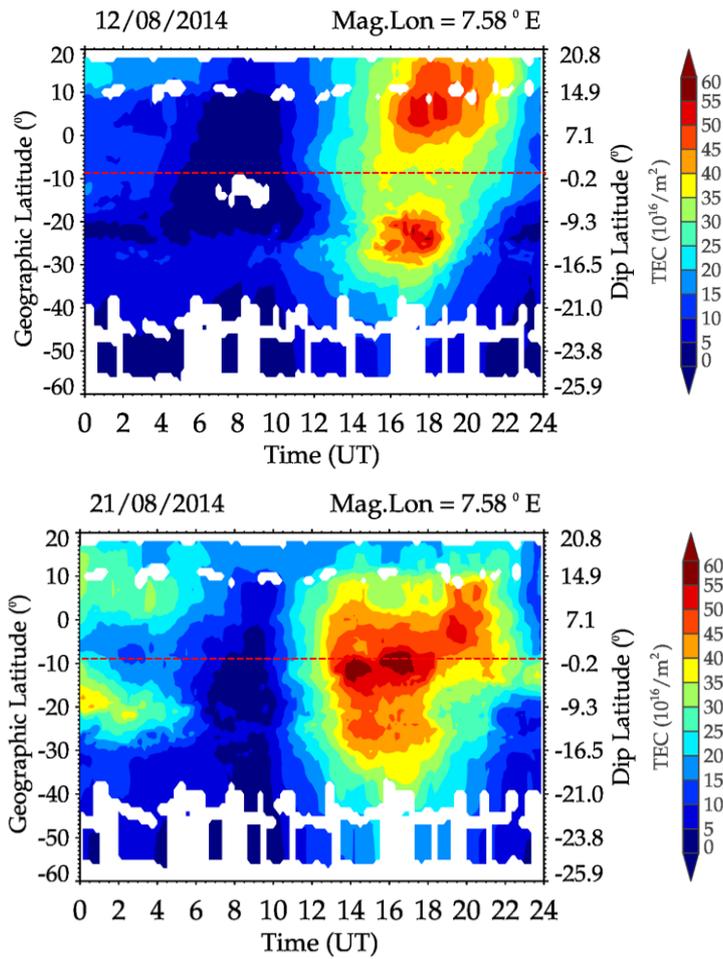
It can be seen that, on 12 of August, 2018, (Figure 4.2 top panel), the development

of the EIA crest begins around 15:00 UT and reaches its maximum at 17:00 UT and 18:00 UT for the southern and northern hemispheric crests, respectively. After that, it gradually weakens until it disappears entirely at 23:00 and 00:00 UT, respectively.

In addition, it can be seen that the SH crest formed earlier than the NH crest, and it is important to note that the magnetic equator has the lowest plasma density. Although anomaly crest formation in both hemispheres lasts for a long time (15:00-21:00 UT), the maximum development of SH and NH crests is delayed by few hours.

Furthermore, the anomaly crests shown in both hemispheres are found near the magnetic latitudes $\sim 15°$ N and $\sim 10°$ S. The whitish region visible in the figure is due to a lack of data.

On the other hand, on August 21, 2018, a significant plasma ionization begins at 14:00 UT, which accumulated near the magnetic equator, with the maximum occurring at 17:00 UT. In addition, as seen in the bottom panel of Figure 4.2, some latitudinal ionization variation can be noticed in a few degrees on both sides of the magnetic equator. TEC variation also indicates that EIA was present between 00:00 UT and 05:00 UT.

The morphologies of the EIA crests varied greatly in terms of position and intensity (TEC values). It can also be seen in Figure 4.2 that the EIA evolution in both hemispheres differed slightly on all days. The pattern of EIA features shown in Figure 4.2 reveals that EIA crests, TEC values (intensities), and their latitudinal positions vary significantly from day to day.

Along the EIA crests, there are changes in intensity (TEC values), latitudinal and longitudinal positions, local time, and season. The monthly variations of the EIA at each magnetic meridian sector were constructed using daily keograms (Figure 4.1). For each meridian sector, the averaged TEC values obtained from daily keograms between 12:00 and 24:00 UT were plotted as a function of the month and geographic/Dip latitude. A typical example of the EIA's monthly variations is shown in Figure 4.3 at the magnetic meridian 7.58° E in 2014.

Figure 4.3 - Monthly averaged TEC along the magnetic meridian as a function of
month and geographic/Dip latitude (left/right y-axis) from January (1)
to December (12) in 2014, along the magnetic meridian 7.58°E.
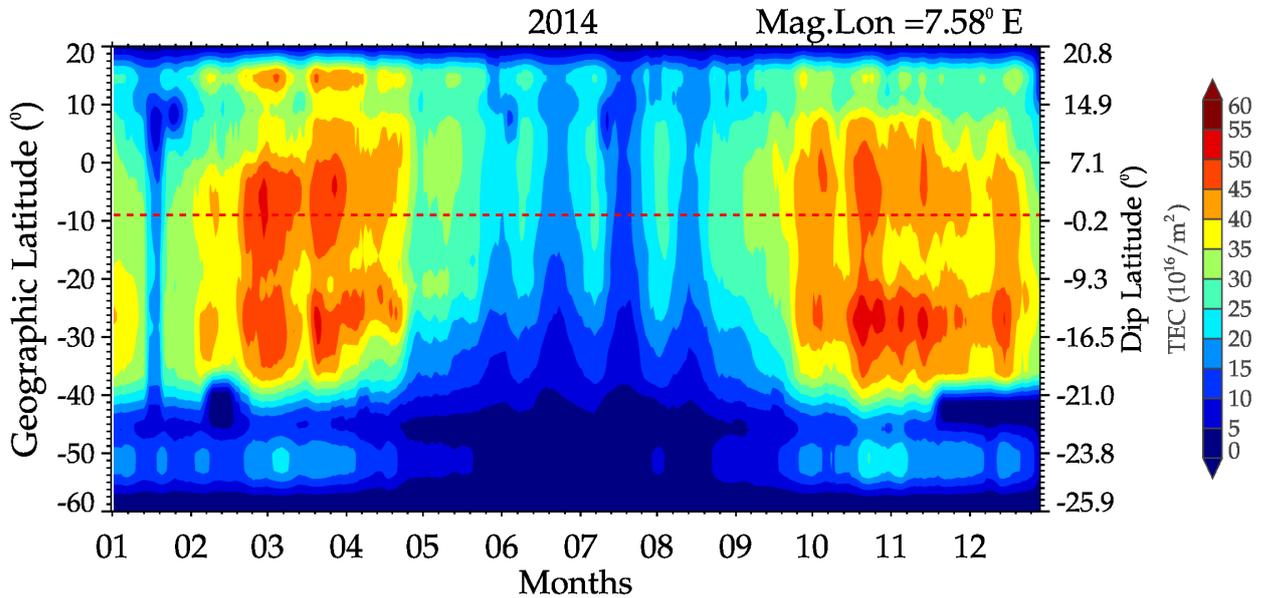
The months were divided into seasons to better understand the monthly variations
of the EIA, as follows: the months of November, December, January, and February
are considered the December solstice, the months of March, April, September, and
October are considered the equinox, and the months of May, June, July, and August
are considered the June solstice. The EIA variations shown in Figure 4.3 demonstrate
significant changes in the TEC level between the equinoxes (March and September)
and solstices (June and December), revealing the EIA's monthly behavior.

The semimonthly and semiannual variation in EIA are clearly shown in Figure 4.3.
The maximum occurs between March and April and October and November, with
a gradual increase in TEC observed between January and March and August and
November. Compared to the winter months, there is a noticeable increase in TEC
during the summer and equinox months. The anomaly crests are more symmetric
during the March equinox than during the September equinox.

There is also a significant variation in the asymmetries between the EIA crests in
all seasons, as shown in Figure 4.3, with regard to the magnetic equator. Some
latitudinal distribution toward NH above the geographic equator can be detected
between February and April.

From the December solstice to the June solstice, the south crest position is seen to contract. The opposite is true for the north crest, which expands from the winter solstice to the December solstice. However, the interhemispheric asymmetry positions at the magnetic equator and intensities of the EIA crests in the figure show some changes (TEC values).

The anomaly pattern observed in this study at each magnetic meridian sector followed a similar pattern. It did, moreover, show some variations in shape, hemispheric crest positions, and intensities over the course of the study years. The latitudinal location of the EIA crests observed from other sectors of the magnetic meridian over time revealed some variations, which will be discussed in the next section.

4.2   Annual variability of EIA

As previously noted, there were some notable patterns in the diurnal and monthly variations in EIA crest intensities (TEC values) and latitudinal positions. The asymmetry, shape, intensities, and magnetic latitude of anomaly crests vary from year to year at the various magnetic meridian sectors considered in this study. Furthermore, the EIA crest pattern in eastern magnetic meridians sectors shows similar characteristics to those in western magnetic meridians sectors.

This section will provide some examples of EIA annual variability. Magnetic and geographic latitudes will be referred to simply as MLat and GLat, respectively. Annual variations in the EIA are depicted in Figure 4.4 (western meridian) and Figure 4.5 (eastern meridian). In addition, due to the lack of data over the ocean, the latitudinal coverage is low.

The seasonal variations of EIA crest intensities in the NH and SH are similar, as shown in Figure 4.4 and Figure 4.5. Both crests are stronger in equinoctial months than in solstice months, indicating distinct semi-annual variations. Furthermore, some latitudinal distribution of TEC intensity can be detected above the geographic equator, particularly from February to April.

EIA crests are asymmetrical in general for all selected meridians and throughout the year. The northern crest is usually closer to the magnetic equator than the southern crest. It's important to mention that NH has fewer GNSS receivers, which means the data for such locations is less representative. As a result, the north crest analysis is less precise than the south crest analysis, with better receiver coverage.

Figure 4.4 - Annual variability of EIA at 7.58°E meridian sector from 2014 to 2019.
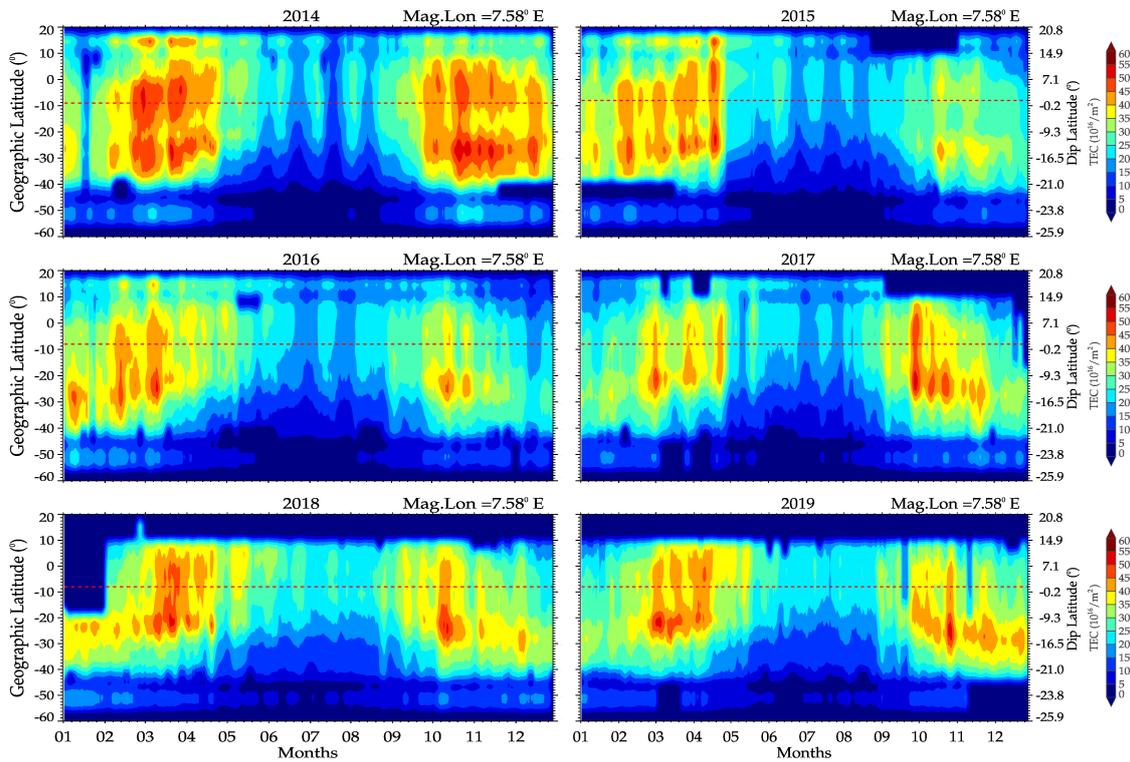
There are also evident EIA semi-annual variations in both figures. The maximum of TEC occurs at crests during January-February-March, the minimum occurring during June-August, and the secondary maximum occurring during September-November. There is a significant interhemispheric symmetry and asymmetry in the TEC strength of the anomaly crests from March to May and October to November, respectively.

Furthermore, the EIA crests appear extended and slightly displaced to the north during the winter months. Besides, the south crest contracts from the December solstice to the June solstice. On the other hand, the north crest exhibits a poleward expansion between such solstices along the year. Such features, on the southern and northern crests, are not clearly seen during 2014 and early 2015 for the 21.50°E meridian. This is attributed to the low latitudinal data coverage along the meridian.

From Figure 4.6 to Figure 4.8, typical examples of such characteristics are shown, with the continuous red line representing the magnetic equator. The anomaly crests in the western and eastern meridian sectors in the figures have similar characteristics over time, with slight differences in intensity and latitudinal positions. The EIA crest

80

intensities have decreased significantly over the years.

Figure 4.5 - Same as Figure 4.4 but for magnetic meridian 21.50°E sector.
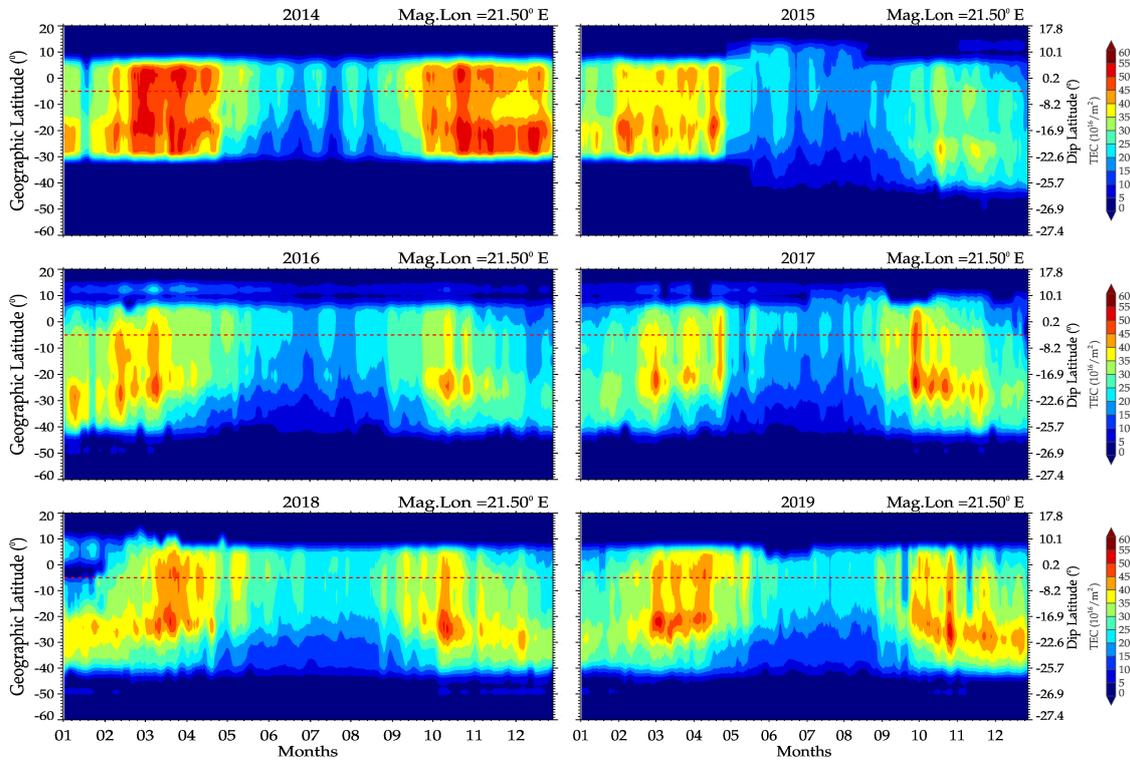
Figure 4.6 - Same as Figure 4.5 but for all magnetic meridian sectors and only the year 2014.
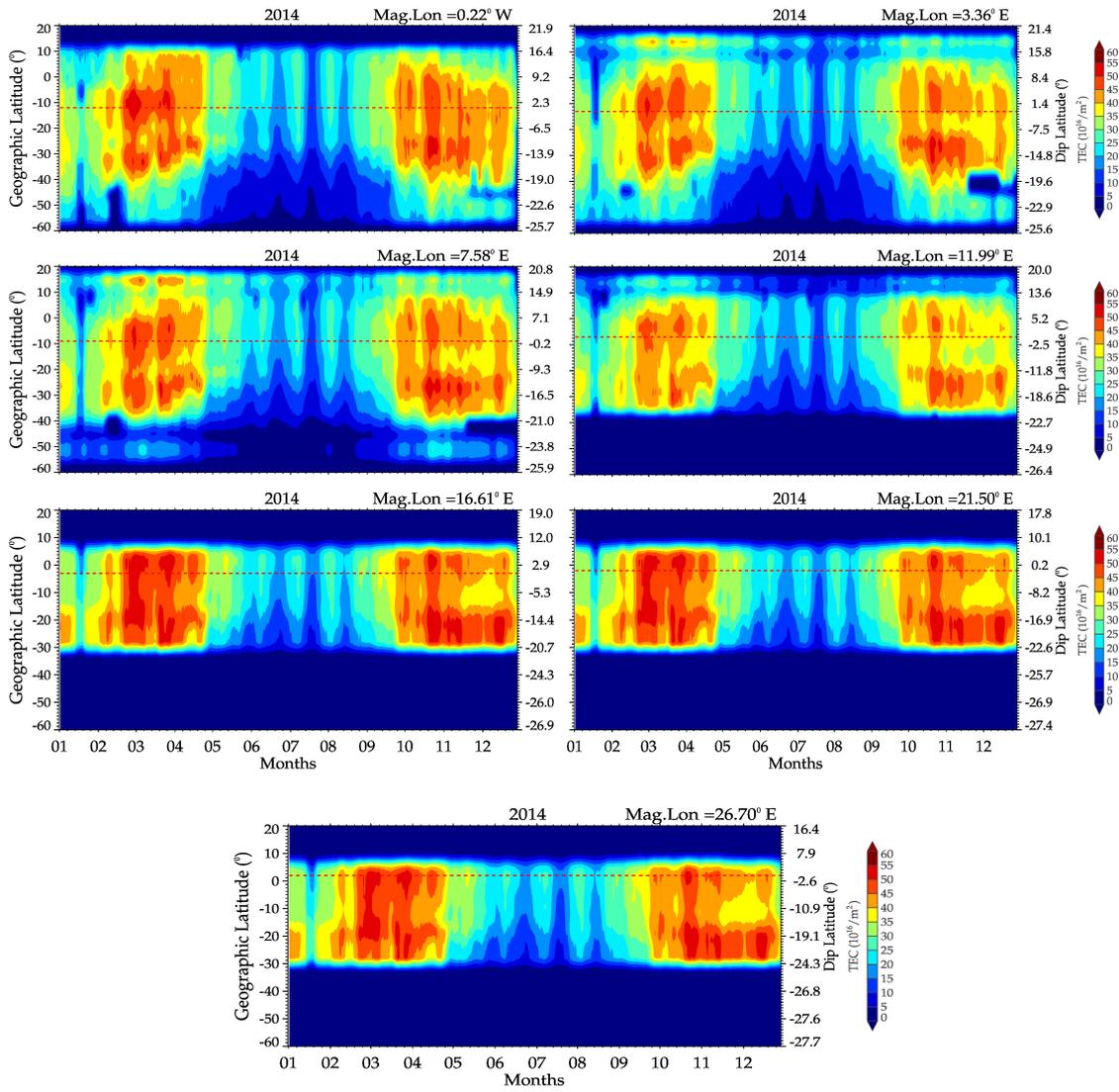
Figure 4.7 - Same as Figure 4.6 but for the year 2017.
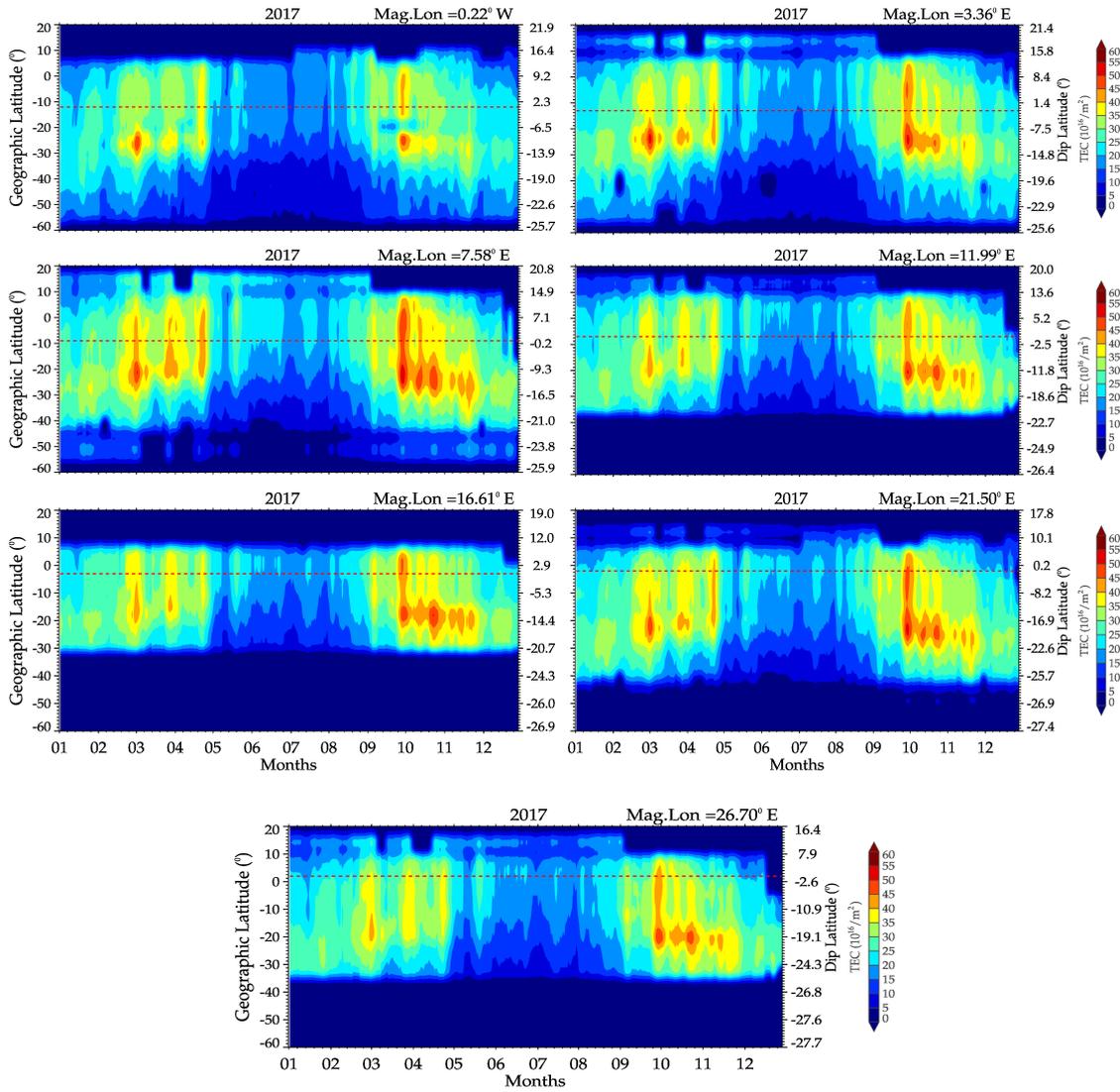
Figure 4.8 - Same as Figure 4.6 but for the year 2019.
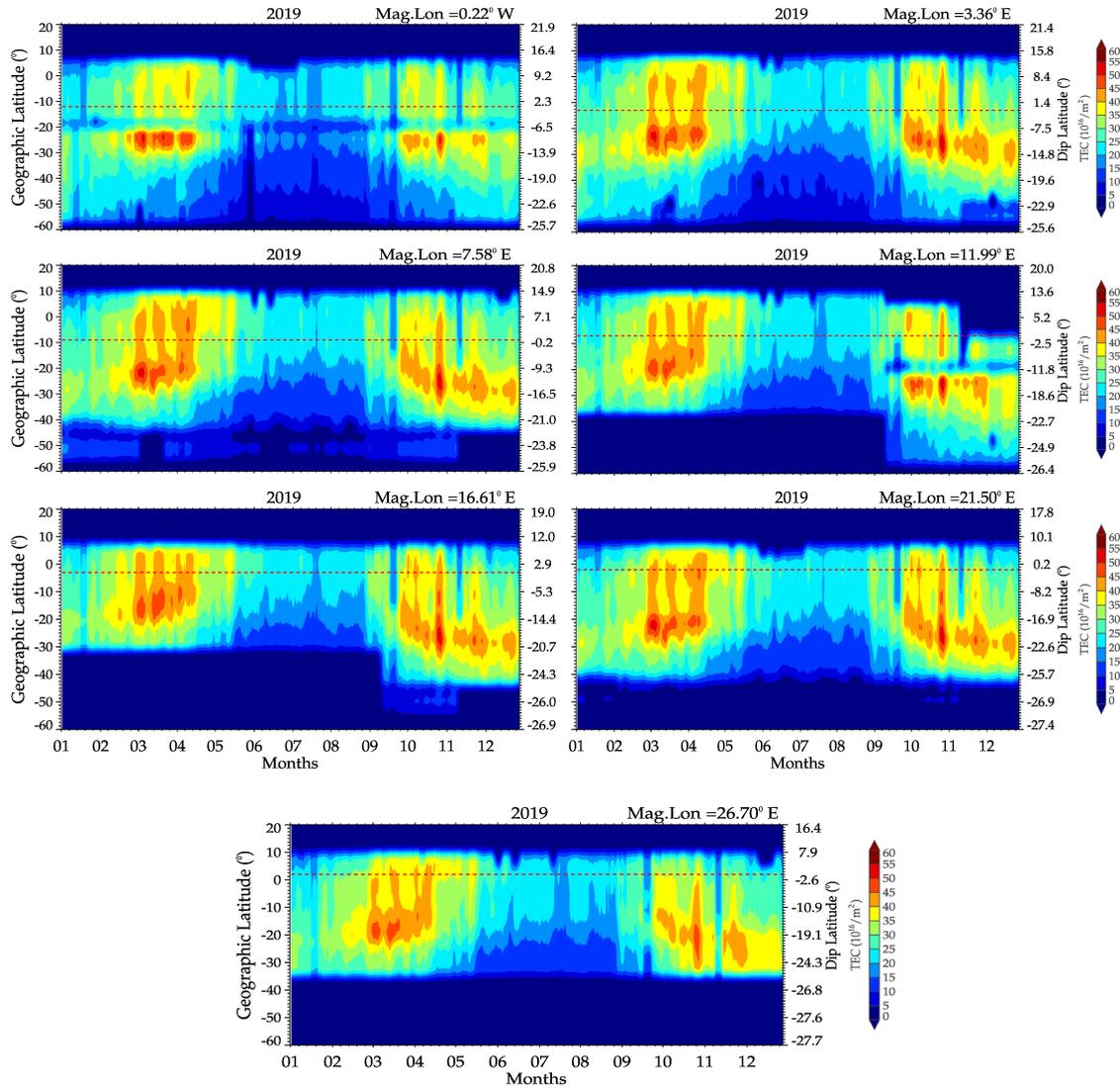
The SH crests of the anomaly are observed to contract in terms of latitudinal distances from the geomagnetic equator from January to April. From September to December, the opposite occurs, demonstrating the expansion of the anomaly crests. During the winter, EIA crests are extended and displaced to the north.

4.3 Annual variations of Southern Hemispheric EIA crest positions

The current research is also focused on the positions of the EIA southern hemispheric crest. The SH EIA crest displayed semiannual variations at the magnetic meridian sectors investigated in this research (Figure 4.1). A typical example of SH crest positions will be presented in this section.

The monthly SH EIA crest position variations at GLat, observed at the meridian sector 7.58°E between 2014 and 2019, are depicted in Figure 4.9. The presence of semiannual variations in the SH crest position in 2014 is observed in Figure 4.9, with maximum expansion during the December solstice and maximum contraction in June. In addition, during the December solstice, the crests are found near the MLat of −9.5 to −17.0 and the GLat of −18.0° to −35°, respectively.

Figure 4.9 - EIA SH crest positions at the Magnetic Meridian 7.58°E sector during the years of 2014-2019.
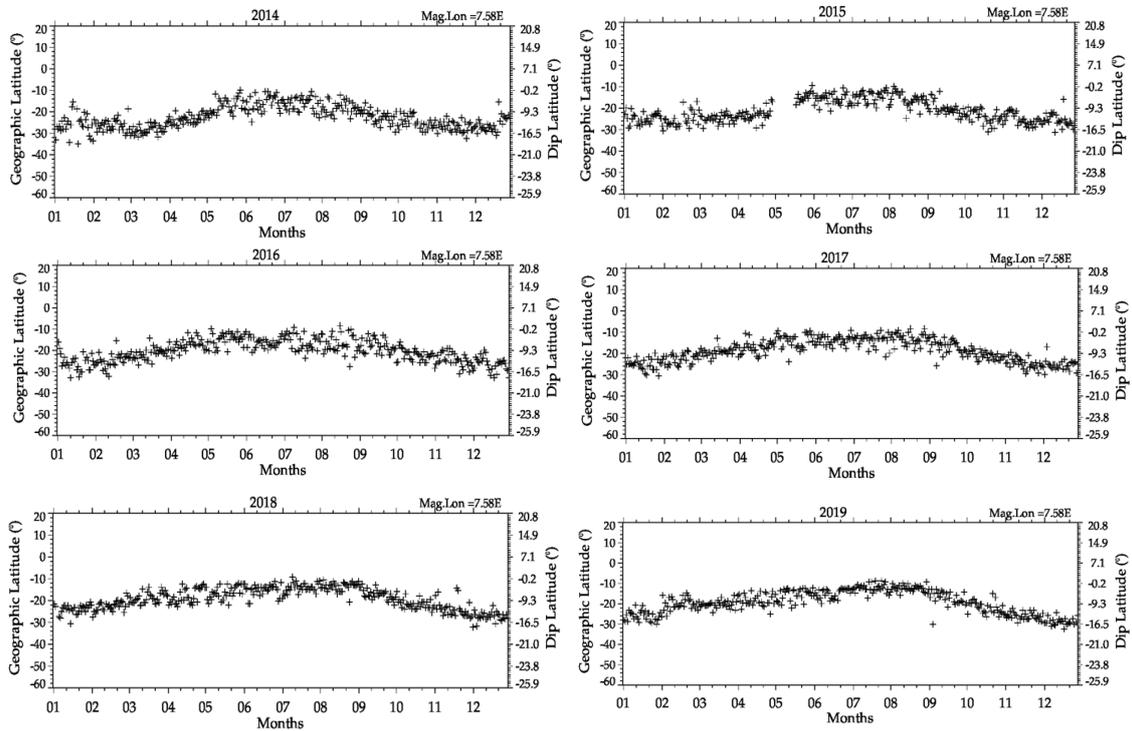
Furthermore, the crest of the EIA in the SH can be seen moving northward near the magnetic equator during the June solstice months. Additionally, the positions of the SH anomaly crests followed a pattern similar to that seen in 2014, with only minor variations between 2015 and 2019. During the June solstice in 2019, the SH crest can be seen near −0.2 MLat and −10.0 GLat, respectively. The SH crest is found at MLat positions ranging from −9.3 to −16.5 and GLat positions ranging from −20.0 to −30.0 during the December solstice.

4.4 Oscillation signatures observed in the day-to-day variability of the EIA crest positions

On annual TEC maps, the SH EIA crests vary semimonthly, as previously demonstrated. As a result, a wavelet spectral analysis of the various crest positions considered in this work was performed at each magnetic meridian.

Planetary Wave (PW) oscillations with periods of around 2, 5, 10, and 16 days have also been seen in the troposphere and lower thermosphere. The manifestations of these waves, however, do not occur exactly in these periods, but rather in bands of a specified width, according to López-González et al. (2009). Furthermore, the oscillation signatures revealed in daily crest positions are just oscillations, not planetary waves.

For two selected meridians, 7.58°E and 11.99°E, respectively, Figure 4.10 and Figure 4.11 illustrate an example of a result obtained using wavelet spectrum analysis. The Morlet wavelet power spectrum for both magnetic meridians is presented as a day-of-year (DOY) function for a period of 2 to 16 days. The cut-off period is lower than 2 days.

Figure 4.10 - Time series and wavelet power spectrum of the southern EIA crest positions at the magnetic meridian (7.58°E) (top) from January (DOY 1) to December (DOY 365) in 2014. The color shade shows spectral power density. The full lines indicate the 90% significance level.
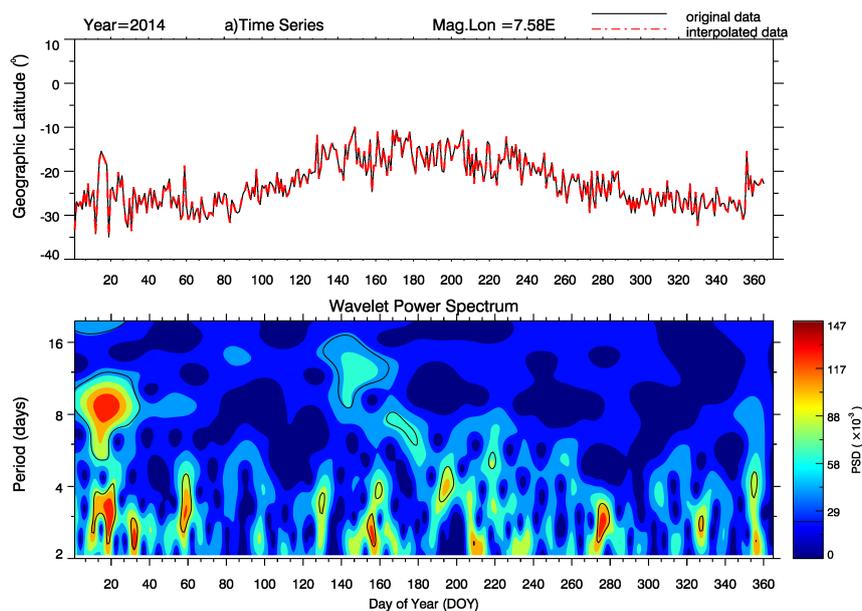
Figure 4.11 - Time series and wavelet power spectrum of the southern EIA crest
position at the magnetic meridian (11.99°E) in 2014. The color shade
shows spectral power density. The regions enclosed with the black lines
depicts the 90% confidence levels.
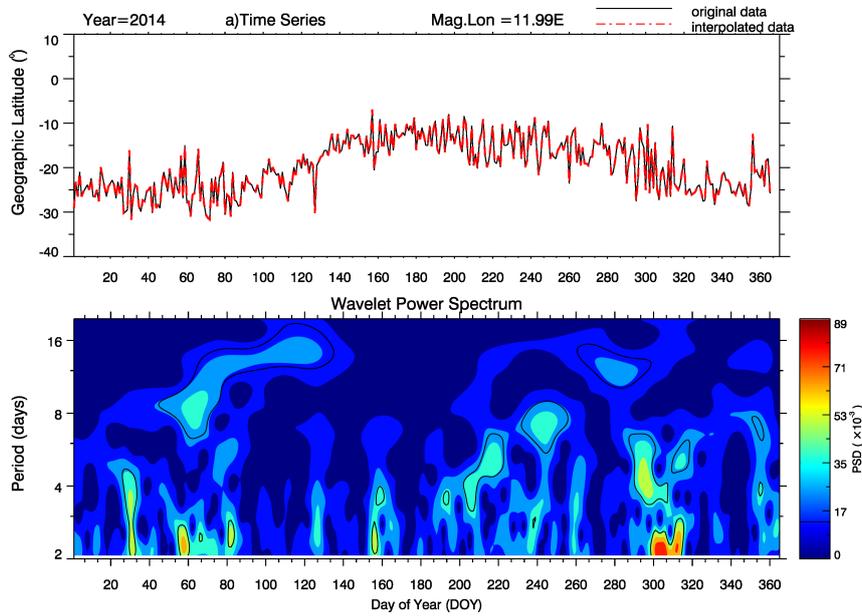
The time series plot shows the interpolated (red lines) and original (black lines)
data. The color shade represents the spectral power density next to the wavelet
spectrum, and the regions enclosed with the black lines depicts the 90% confidence
levels. Several packets of oscillations can be seen in the figures from each Morlet
wavelet spectrum.

The Morlet wavelet spectrum for magnetic meridian sector 7.58°E (Figure 4.10,
bottom panel) reveals oscillations with periods of 2-3 and 8 days found at DOY
0-20. Around DOY 50-56, 181-190, and 265-275, there are also oscillation signatures
of 3-4-days, 4-days and 3-days are presented, respectively.

The wavelet spectrum of the 11.99°E magnetic meridian, on the other hand, ex-
hibits oscillations ranging from 2-4-day to 2.5-day to 3.5-day to 2-3-day to 2-4-day
(Figure 4.11 bottom panel). These oscillations can be found in the DOYs 25−30,
55−60, 140−160 and 150−160, in that order. The cross-power wavelet spectrum in
Figure 4.12 shows that the two magnetic meridians had common period oscillations.

Figure 4.12 - Cross wavelet transform of the latitudinal southern crests positions of the EIA between the magnetic meridians 7.58°E and 11.99°E during 2014. The regions enclosed with the black lines depicts the 90% confidence levels.
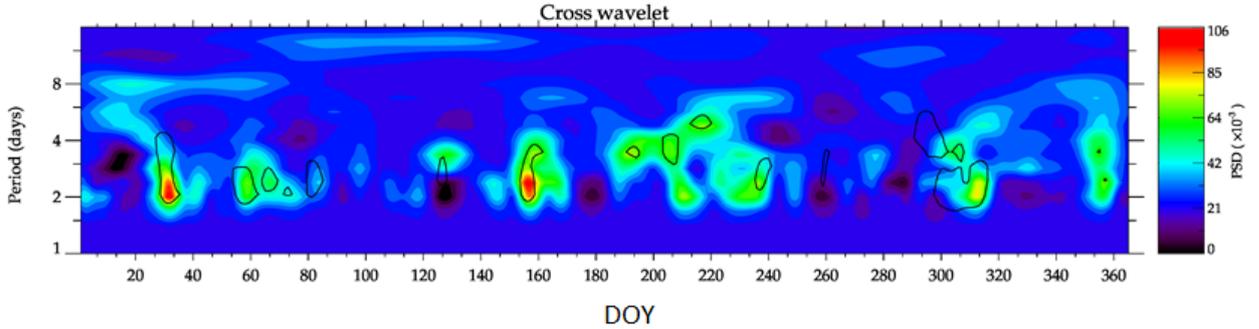
The cross-wavelet spectrum shows the oscillation of 2-3 days during the DOY 25-35. The $3-4$-day oscillation at DOY 200-220 is also visible. Table 4.1 summarizes the periodic oscillations shared by both time series.

Table 4.1 - Common oscillations and occurrences estimated from cross-wavelet analysis.

DOY	Period (day)
20-40	2-3
60-80	2-3
120-130	3
180-200	4
200-220	2
220-240	2
300-320	2,3
340-360	2-4

Figure 4.13 depicts the common period of oscillations observed at each magnetic meridian sector from January 2014 to December 2019. The color bar represents the frequency of occurrence of the common oscillations, with values ranging from 0 (blue) to 20 (red). The graph shows that 2-day oscillations have been dominant over the years, occurring on days ranging from 0 to 20, 20 to 40, 180 to 200, 220 to 240, 240 to 260, and 340 to 360.

3-day oscillations can also be detected near the days 0-20, 200-220, 240-260, and 340-360. Similarly, 8-, 6-, and 4-day oscillations can be seen near the days 0-20 , 40-60 and 240-260, respectively. In Table 4.2, the oscillations identified in all magnetic

meridian sectors are summarized.

Figure 4.13 - Occurrence of the most common oscillations observed at all magnetic meridian sectors, between January 2014 and December 2019. The color shades next to the plot show number of occurrence.

Period oscillations occurrences at all sectors (2014–2019)
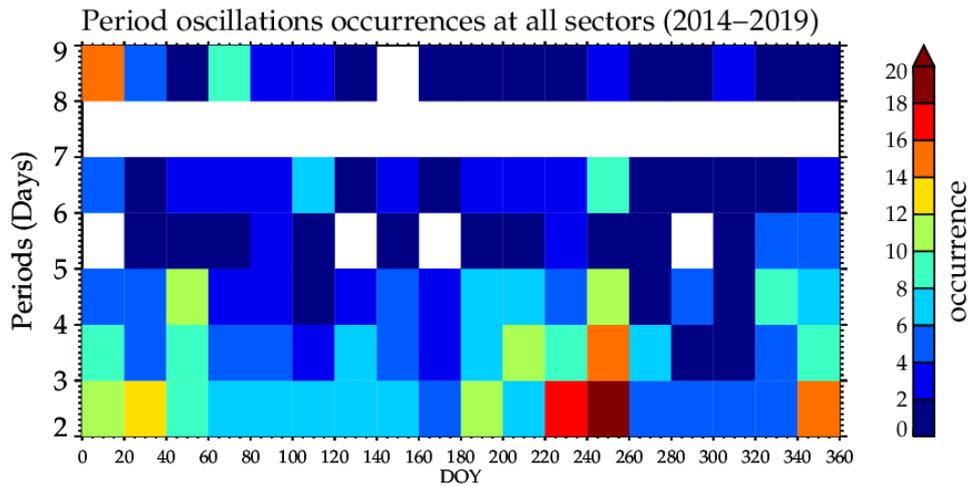
Table 4.2 - Most common oscillations occurrence observed at all magnetic meridian sectors from January 2014 to December 2019.

DOY	2-day	3-day	4-day	5-day	6-day	7-day	8-day
0-20	11	9	5	-	6	-	15
20-40	14	5	6	2	1	-	5
40-60	10	9	11	1	3	-	1
60-80	8	5	4	2	3	-	9
80-100	8	6	3	3	4	-	3
100-120	8	4	1	1	8	-	3
120-140	7	8	3	0	2	-	2
140-160	7	6	5	1	4	-	-
160-180	6	4	3	-	2	-	2
180-200	11	8	8	1	3	-	2
200-220	7	11	7	2	3	-	1
220-240	17	10	6	4	4	-	2
240-260	20	16	11	1	10	-	4
260-280	5	8	2	2	1	-	2
280-300	5	2	5	-	2	-	1
300-320	5	2	1	1	1	-	4
320-340	6	6	9	6	2	-	2
340-360	16	10	7	5	4	—	1

5 DISCUSSIONS

The climatological characteristics and morphologies of the EIA were investigated at different magnetic longitudinal sectors, using TEC maps obtained from a network of GNSS receivers installed over the Southern American. The results obtained in the present study will be compared and discussed with previous ones obtained at different longitudinal sectors. The Sheffield University Plasmasphere Ionosphere Model at Instituto Nacional de Pesquisas Espaciais (SUPIM-INPE) will be used to explain the observed EIA behavior.

It is recognized that EIA crests exhibit day-to-day, month-to-month, annual, and solar cycle variations. These changes are controlled by several factors, such as the ionospheric electric fields, the thermospheric wind, the subsolar point location, dynamical processes, and the local geomagnetic field configuration (BATISTA et al., 1986; ABDU et al., 1991a; ABDU et al., 2008; FAGUNDES et al., 2005; RAM et al., 2009; KIKUCHI et al., 2000; TAKAHASHI et al., 2014a; BALAN et al., 2018; KHADKA et al., 2018; DIAS et al., 2020). The temporal and longitudinal differences of the EIA morphology are the main focus of this present research.

5.1 Case study 1: latitudinal TEC distribution with two peaks/crests

At the equatorial ionospheric region, during the daytime, strong $\vec{E} \times \vec{B}$ drift drives ionization to altitudes, and it then diffuses along the geomagnetic field lines aided by pressure gradient forces and gravity to lower latitudes piling up to form two crests. The minimum of plasma occurs over the magnetic dip equator. Moreover, the equatorial dynamo electric field is thought to be the primary factor of the crest motion (YEH et al., 2001). The day-to-day variations of the EIA crests are controlled dominantly by ionospheric electrodynamics processes.

The formation of the anomaly crests has diurnal variation characteristics. In the previous chapter, two prominent features were observed and described. The first feature of the EIA is the presence of anomaly crests at low latitudes with less plasma density at trough regions near the magnetic equator. The other feature is when the latitudinal TEC distribution shows a high concentration of ionization near the magnetic equator and decreases towards low latitudes.

The daily evolution of EIA as observed at the various magnetic meridians used to investigate its morphology/features reveals comparable features with slight differences in intensity, strength, and latitudinal positions. To further understand the dynamics

that influence EIA crest motion and morphology, the SUPIM-INPE model will be used.

The variability of the EIA during the daytime obtained at magnetic meridian sector 7.58°E on August, 12, 2014 is shown in Figure 5.1, which is a typical example of TEC distributions. The TEC variation as a function of UT and geographic/Dip Latitude is depicted in the figure. The EIA crest formation starts around 15:00 UT and reaches its maximum at the hours of 17:00 UT and 18:00 UT for the crests in the southern and northern hemispheres, respectively.

Figure 5.1 - Contour plot of TEC distribution at the magnetic meridian 7.58°E sector as function of UT and geographic latitude (left yaxis)/ magnetic dip latitude (right y-axis) on 12 August, 2018. In figure shows a double-peaked EIA crest at both hemispheres. The red horizontal line represent the location of the magnetic equator.
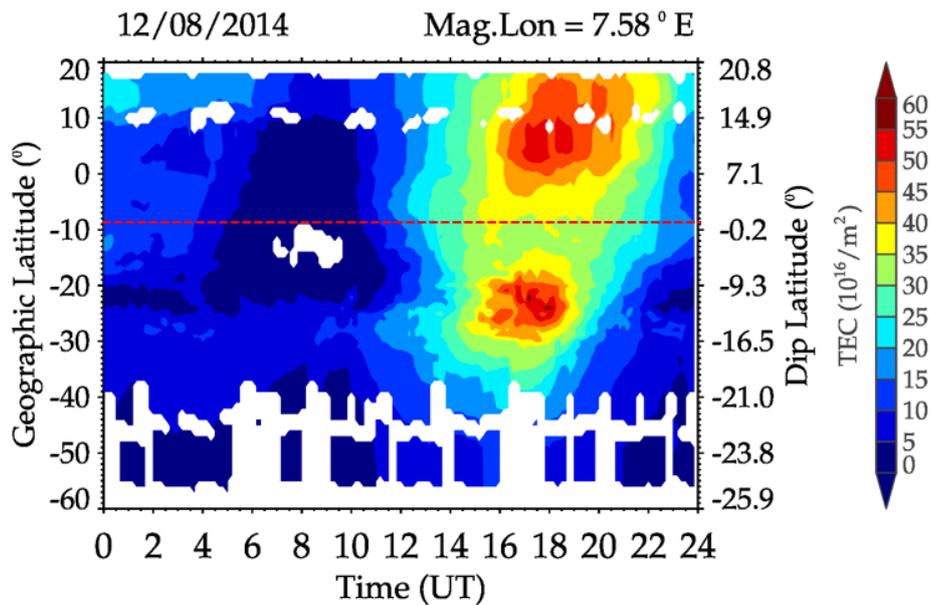
The crests then begin to weaken, eventually disappearing between the hours of 20:00 and 22:00 UT. Both crests can be found near magnetic latitudes ∼ 15° N and ∼ 10° S, and there is less plasma density around the magnetic equator. In addition, the southern crest is smaller and more intense than the northern crest, which is broader and less intense.

The equatorial dynamo electric field was identified as the primary cause of this crest motion by Raghavarao et al. (1988) and Yeh et al. (2001), who found a strong corre-

lation between the integrated strength of the electrojet and fountain effect strength. The SUPIM-INPE model was utilized to explain what is driving the anomaly crest motion latitudinal distribution, as illustrated in Figure 5.2 for the same conditions as Figure 5.1. The input parameters used by SUPIM-INPE to model the observed EIA morphology (Figure 5.1) can be found in Subsection 3.4.3.

Figure 5.2 - Vertical plasma drift (SCHERLIESS; FEJER, 1999) (a) and the effective wind velocity (HEDIN et al., 1996) (b) used as input parameters in the simulations of the SUPIM-INPE model. The output is modeled TEC (c).
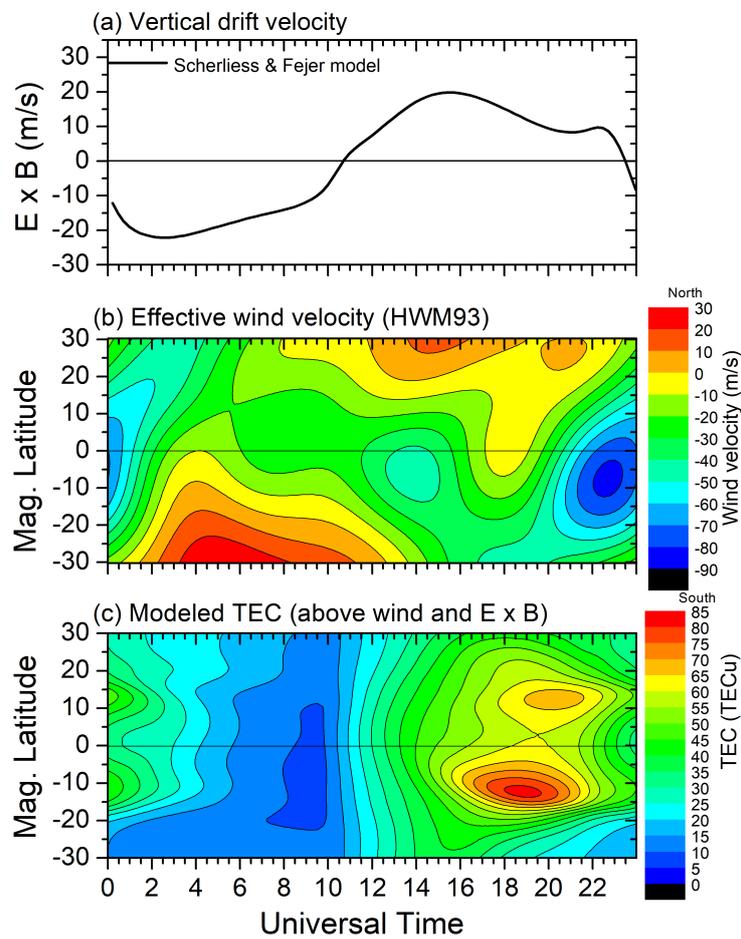
The SUPIM-INPE model inputs used here were the zonal electric field empirical model from Scherliess e Fejer (1999) and the effective meridional wind from the Horizontal Wind Model-93 (HWM93) (HEDIN et al., 1996), as shown in Figure 5.2a and Figure 5.2b, respectively. The observational results were taken along the mag-

netic meridian, which crosses the geographic longitude of 293.5° and latitude of 0.0°, respectively (meaning the Local Time (LT)=Universal Time (UT)-4.43). Such meridian is at magnetic longitude of 7.58°E, as given by the IGRF model.

The vertical drift is well known as the primary factor responsible for uplifting the plasma over the magnetic equator and then diffuses along the geomagnetic field lines (YEH et al., 2001). It has been established that during the daytime, the drift is upward (positive values) and downward (negative values) during the night (SCHERLIESS; FEJER, 1999). The drift velocity, as indicated in Figure 5.2a, is upward and downward during the day and night, respectively, according to the model developed by Scherliess e Fejer (1999).

Furthermore, looking at Figure 5.2, from the hours of 04:00 UT to 10:00 UT, a downward drift can be seen, and then it started to move upward. The effective wind had strong northward movement between the latitudes −15° and −30°, while from the magnetic equator and above, the southward direction of the wind can be noticed. In the same time interval, due to such configurations and the recombinations, the modeled TEC values showed a low level of plasma density extending from latitudes −30° to 30°.

The EIA development modeled by the SUPIM-INPE started around ±15:00UT and reached its maximum between 18:00 UT and 20: 00 UT for the southern and northern hemispheric crests, respectively. Then it begins to weaken until it disappears around 22:00 UT. Observed TEC variations indicate that the EIA intensifies from 15:00 UT to 22:00 UT as to the interhemispheric crest position at latitude 10°S and 15°N for both crests. The modeled results well represented such features. The TEC in the southern hemisphere is slightly intense than in the northern hemisphere. Additionally, the modeled TEC shows a time delay to have fully developed crests of 2-3 hours after the maximum upward drift occurred.

As shown in the effective meridional wind velocity, the wind is a projection of the zonal and meridional winds along the magnetic field line. A strong southerly wind can be noticed around magnetic latitude ±15° in Figure 5.2b, between 12:00 and 17:30 UT. This large latitudinal range of the wind and the strong downward wind observed at 12:00-14:30 UT is responsible for the south crest formation, with its maximum value around 18:00 UT compared to the north crest. However, around the hour of 17:30 UT, a decrease of the southward wind intensity and its latitudinal distribution can be seen, which resulted in the late formation of the north crest.

In the NH, a southward wind results in an upward movement of ionization in that hemisphere. A high wind intensity at the southern hemisphere will imply a more effective downward movement of ionization in that hemisphere (BATISTA et al., 2011), and consequent asymmetry in the two crests of the EIA.

The wind effect will only be seen after few hours (BATISTA et al., 2011), when the southern crest is more intense (denser) than the northern crest. A clear strong southward and weak northward movement of the wind from the equator can also be observed from the wind model at round the hour of 17:00 UT, which depicts the southern hemispheric crest being more intense than in the northern hemisphere, as shown in Figure 5.2c.

From the comparison between the observational data (Figure 5.1) and model results, the SUPIM-INPE can reproduce the TEC distribution, characterized by being more intense in the southern hemisphere than the one in the north. The SUPIM-INPE model result also brings out well the asymmetry in the TEC over time.

Despite the fact that our results provided a good explanation for the formation of EIA crests on August 12, 2014, using a coherent combination of $\vec{E} \times \vec{B}$ drift and effective wind modeling, we decided to investigate different $\vec{E} \times \vec{B}$ drift models in order to confirm or validate our analysis.

Nogueira et al. (2013) investigated the longitudinal variation in Global Navigation Satellite System TEC and topside ion density over the South American sector. They observed a strong longitudinal variation in TEC, with larger values over the eastern Brazilian sector than those in the Peruvian western sector. The SUPIM-INPE model was used to identify the control factors responsible for the longitudinal variations of TEC between these two sectors.

According to their findings, the daytime vertical drift observed over the Peruvian western sector is approximately twice that observed over the Brazilian sector, resulting in longitudinal variations between the two sectors. We will use the Scherliess e Fejer (1999) model as a reference for the electric field to investigate the effect of vertical drift over the EIA crest position.

In this regard, we modified the electric field provided by Scherliess e Fejer (1999). In doing so, data for the vertical drift velocity for August 12, 2014 was obtained from the Jicarmarca Radio Observatory database in Peru (JICAMARCA..., 2021). The JULIA data acquired is depicted as a black circle dot color in Figure 5.3 (top left

panel) and was obtained between the hours of approximately 14:00 UT and 18:00
UT.

Figure 5.3 - Top panels shows the vertical drift models (Model 01 and Model 02),
while the bottom panels represent modeled TEC obtained by both ver-
tical models.
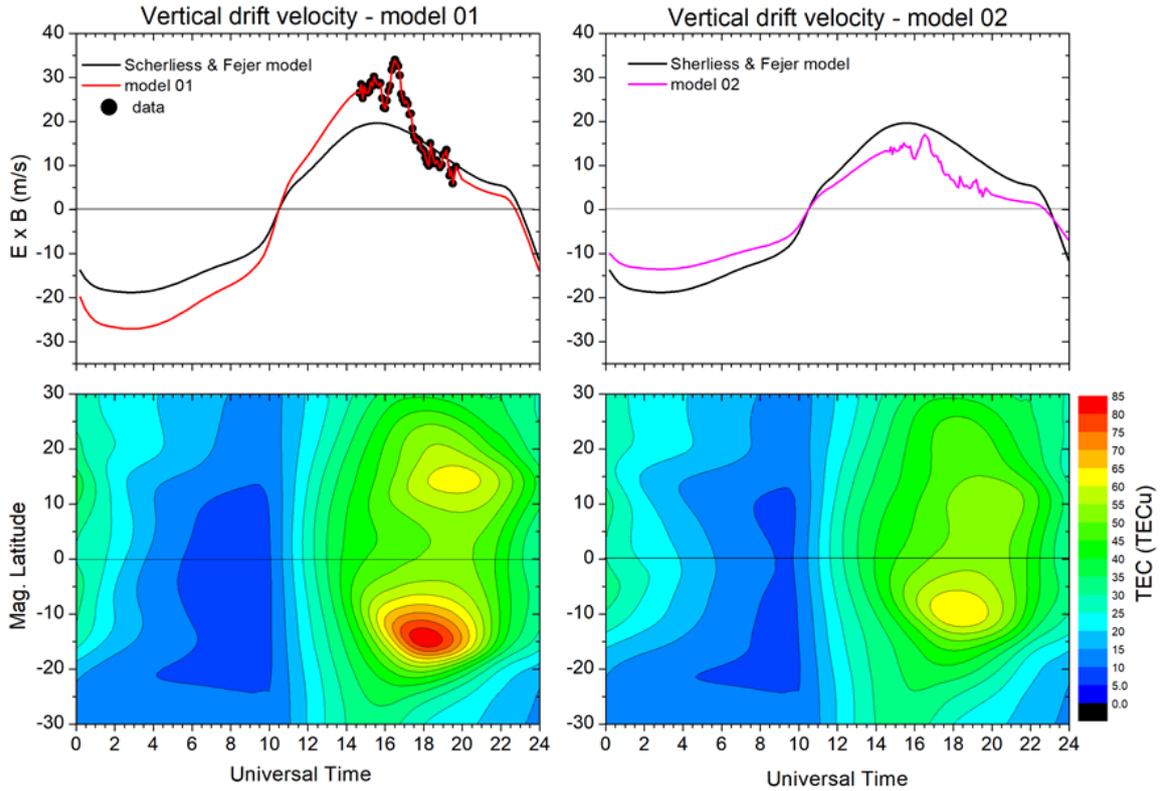
Vertical drift velocity values obtained from ground-based instruments such as
digisonde or magnetometer, according to Souza et al. (2000), can be used as an
input parameter to the SUPIM-INPE model. When the measured drift velocity
from the instrument does not have complete data for the entire period, in our case,
from 00:00 to 24:00 UT, the measured drift velocity can be completed using the
drift velocity given by the Scherliess e Fejer (1999) model. To that end, the modeled
values can be adjusted as many times as needed until the observed measurements
agree with the modeled values.

As can be seen in Figure 5.3, the drift velocity values obtained from JULIA radar
were obtained over a short period of time (i.e., from 14:00 to 18:00 UT), and the
procedure reported by Souza et al. (2000) was used to obtain the drift values for
the entire day. The values obtained from Scherliess e Fejer (1999)'s model were

thus adjusted to match the data. The values were multiplied by a factor of 1.44, indicating that the drift velocity becomes stronger and covers the entire required period (0:00-24:00 UT).

The vertical drift velocity is then used as an input parameter to the SUPIM-INPE model, which is depicted in the top left panel of Figure 5.3 by a continuous red thick line (model 01). The figure shows that the drift velocity from model 01 and that of Scherliess e Fejer (1999) exhibit similar behavior. Furthermore, in comparison to the model from Scherliess e Fejer (1999), the drift values observed from model 01 are more downward (before 10:00 UT) and upward (after 10:00 UT) (this is a result of the methods used). It is important to note that the effective meridional wind as an input parameter is the same as observed in Figure 5.2 and was held unchanged.

The SUPIM-INPE results, when using the drift model 01, show an amplified expansion of the crests towards the poles, as shown in the lower left panel of Figure 5.3. The discrepancies between these results and the data were caused by this expansion, as well as a decrease in the intensity of the north crest.

Another drift velocity model, obtained by dividing model 01 values by a factor of 2, is shown in the top right panel of Figure 5.3. It is represented by a thick pink line that runs continuously (model 02). However, as a result of this factor, the drift velocity in model 02 is weaker than that of the Scherliess e Fejer (1999). The vertical drift velocity, model 02, is then fed into the SUPIM-INPE model as an input parameter.

The modeled TEC distribution resulting from model 02 drift velocity is shown in the bottom right side of Figure 5.3. When compared to the experimental data from Figure 5.1, the modeled results showed an evident contraction of the EIA crests, which was significant enough to cause disagreements.

In conclusion, these comparisons show that the anomaly crest positons and motions observed in the observational data can be modeled and reproduced using the SUPIM-INPE model. Furthermore, it can be deduced from these investigations that the primary cause of this crests motion is the equatorial dynamo electric field, which has also been reported elsewhere by Raghavarao et al. (1988) and Yeh et al. (2001). The anomaly crests configuration observed in both scenarios, however, was caused by effective meridional winds, which is consistent with observations made by Batista et al. (2011) and Mridula et al. (2020).

5.2 Case study 2: latitudinal TEC distribution with one peak

The previous section used the SUPIM-INPE model to discuss a fully developed EIA with two crests on each side of the magnetic equator. This section will examine the second feature of EIA development, which is inhibited or indicates no EIA development.

Figure 5.4 depicts a typical example of the second feature of latitudinal TEC distribution, with a single maximum near the magnetic equator. The apparent bulk of ionization can be seen near the magnetic equator at the start of the maximum formation, around 14:00 UT, with its maximum occurrence at $\sim$ 17:30 UT. Above and below the magnetic equator, there is an ionization distribution.

Figure 5.4 - Same as Figure 5.1, but on 21 August, 2018, when no EIA development, but, shows bulk of ionization near the magnetic equator.
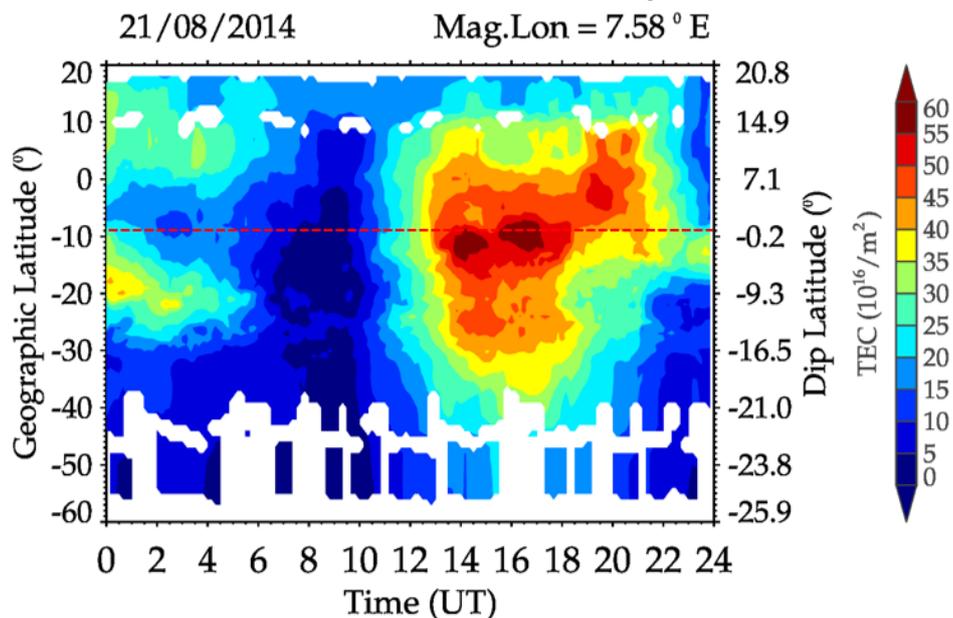
The SUPIM-INPE model will be used once more to identify the control factors responsible for the single crest formation observed in Figure 5.4. The input parameter values used in the previous section in the SUPIM-INPE model did not reproduce the observed morphology of the EIA shown in Figure 5.4. However, a coherent tendency was observed when the drift values were decreased to produce the drift model 02. However, changes to such input parameters are required to determine which levels are responsible for the formation of the feature shown in Figure 5.4.

The TEC distribution modeled by the SUPIM-INPE model based on climatological conditions for August 21, 2014, as presented in Figure 5.4, is depicted in Figure 5.5. The vertical drift velocity provided by Scherliess e Fejer (1999) is depicted in Figure 5.4a by a continuous black line. Vertical drift velocity data from the JULIA radar instrument, represented by a circle black dot in the same panel of Figure 5.5a, was acquired between the hours of 14:00 and 20:00 UT.

In Figure 5.5, the vertical drift velocity m01 was used as an input parameter to the SUPIM-INPE model. The drift velocity values of m01 were obtained by combining data from the JULIA radar and that from Scherliess e Fejer (1999), with a few adjustments made by dividing it by a factor of 1.41.

Figure 5.5 - Same as Figure 5.2, but vertical drift velocity m01 (as thick red line) was used the input parameter in the SUPIM-INPE model.
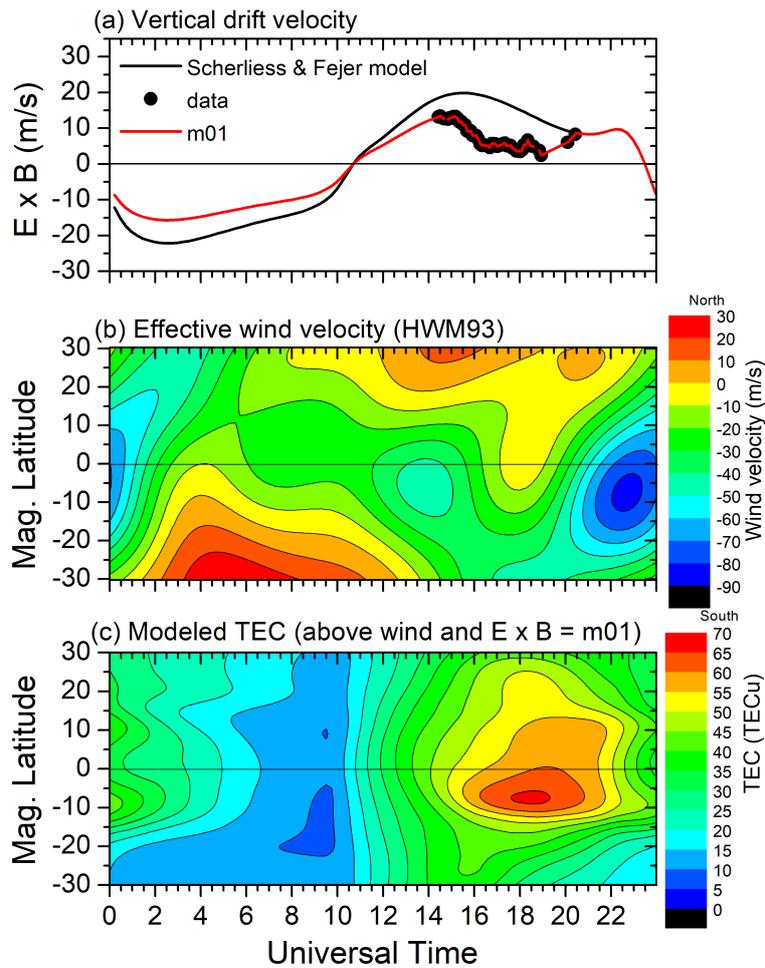
The vertical drift velocity, m01, is less downward (before 10:00 UT) and more upward in comparison to the model from Scherliess e Fejer (1999), as shown in Figure 5.5. The effective meridional wind used as an input parameter in Figure 5.5 is the same as the one used in Figure 5.2 and has been left unchanged.

Only the southern anomaly crest formation can be seen after the maximum upward drift velocity occurrence at the hour of 14:00 UT, which began at 15:30 UT. Its maximum occurs at 18:30 UT, as shown in Figure 5.5c. It can also be seen that the maximum TEC of the crest is found near magnetic latitude $-10°$.

The latitudinal position of the single crest seen in Figure 5.4 is close to the magnetic equator. When the weaker drift velocity m01, and the effective meridional are used as input parameters to the model, the result modeled by the SUPIM-INPE model is found near magnetic latitude $-10°$.

To understand why the SUPIM-INPE model results did not agree with the observation shown in Figure 5.4, more investigation on the input parameters was required to control the required morphology of the EIA single crest in Figure 5.4. The effective meridional wind parameter was still kept constant in this scenario, and drift velocity m01 values were further adjusted by dividing the values in m01 by a factor of 2.00, represented as the blue continuous thick line in Figure 5.6a and depicted as m02.

Figure 5.6 - Same as Figure 5.5, but vertical drift velocity m02 (as thick blue line) was used the input parameter in the SUPIM-INPE model.

(a) Vertical drift velocity

(b) Effective wind velocity (HWM93)

(c) Modeled TEC (above wind and E x B = m02)
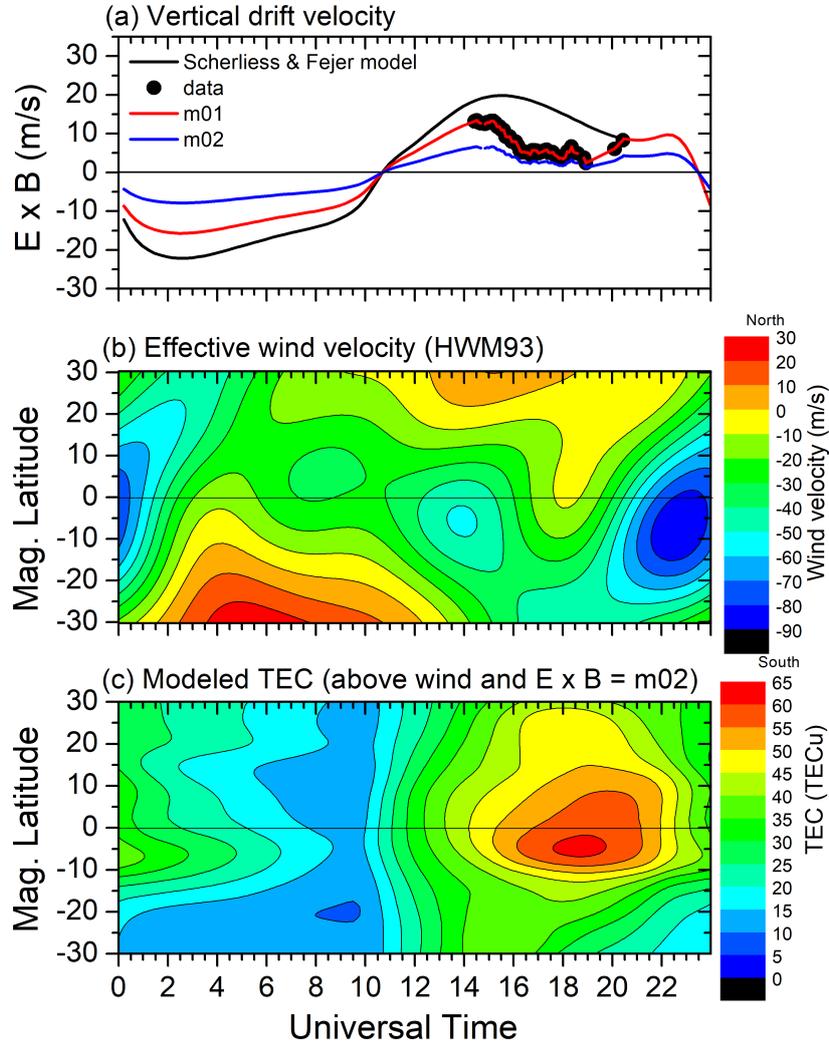
The vertical drift velocity, m02, is included in model as an input parameter. In addition, Figure 5.6 shows that m02 drift velocity is less downward (before 10:00 UT) and less upward (after 10:00 UT) than m01 and the model from Scherliess e Fejer (1999). After reaching the maximum upward drift velocity of m02 at the hour of 15:00 UT, an intense ionization is observed near the magnetic latitude −5°, with the maximum crest density formed at 18:30 UT, as shown in Figure 5.6.

Furthermore, when the SUPIM-INPE model is run with the weaker drift velocity, m02, the single crest EIA produced is found near the magnetic equator at latitude

$-5°$. As a result, the lower drift velocity, m02, did not reproduce the desired single crest position seen in Figure 5.4.

However, despite the fact that vertical drift velocity is the primary driving force for EIA formation, the latitudinal position of the EIA single crest configuration in Figure 5.4 was not generated by the vertical drift velocities m01 and m02.

As a result, the input vertical drift velocity parameter must be constant while making minor adjustments to the effective meridional wind parameter.

Using the same method stated earlier on by Souza et al. (2000), the effective meridional wind parameter, which was held constant throughout the simulation procedure, was changed by dividing the wind values by a factor of 1.41, implying that the wind strength was reduced. The adjusted effective meridional wind (Figure 5.7b) and the vertical drift velocity of m01 were then used as input parameters in the SUPIM-INPE model. The results of adjusting the wind parameter are shown in Figure 5.7.

Figure 5.7 - Same as Figure 5.6, vertical drift velocity m01 was held fixed, but the effective meridional winds changed by dividing it by a factor of 1.14 and both were used as input parameters in the SUPIM-INPE model.
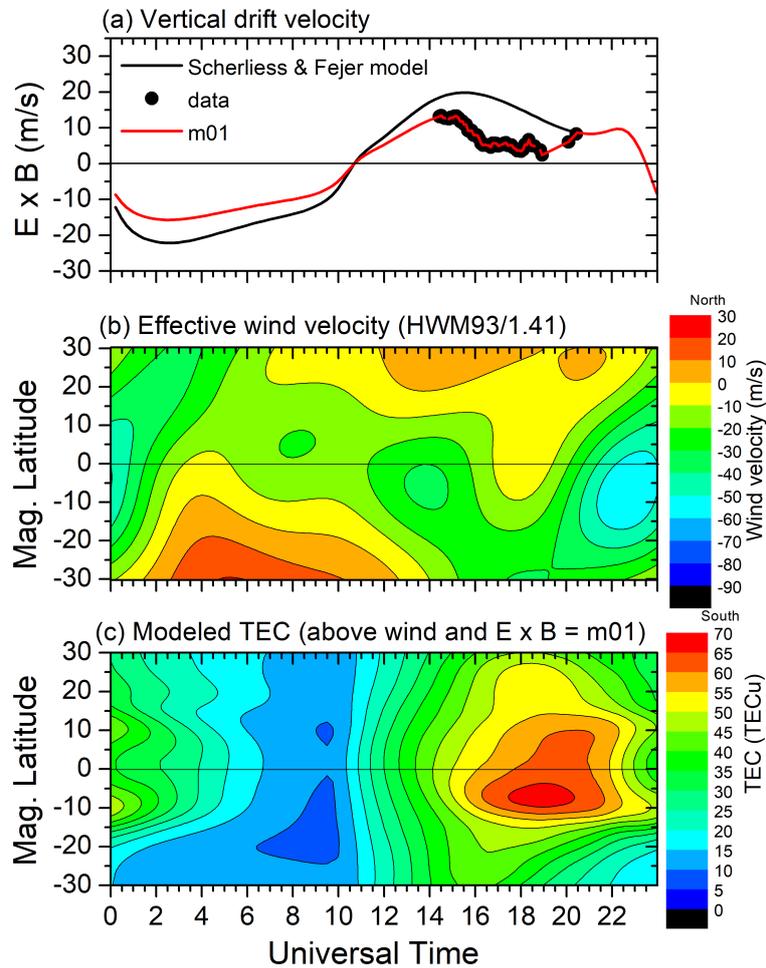
The modeled TEC in Figure 5.7c, based on the wind adjustments, did not produce the configuration of the EIA crest observed in Figure 5.4. It implies that the vertical drift velocity m01 (Figure 5.6a) and the altered effect meridional wind were insufficient to produce the desired configuration. To explain why the latitudinal crest position configuration remained unchanged, the vertical drift velocity m01 (Figure 5.6a) was substituted as the input parameter for the weaker drift velocity, m02, from Figure 5.6a.

The combination of the weaker drift velocity m02, and the adjusted effect meridional wind was then used as input parameters, as illustrated in Figure 5.8. Based on the

changes, the outcome of the modeled TEC configuration shown in Figure 5.8c was slightly better than the previous input parameters. It can be concluded that the weaker drift velocity m02, combined with the altered meridional wind, provided good approximations but did not produce the exact EIA single crest latitude position predicted in Figure 5.4.

Figure 5.8 - Same as Figure 5.7, but vertical drift velocity m02 was used with the combination of the altered effective meridonal winds values as input parameters in the SUPIM-INPE model.
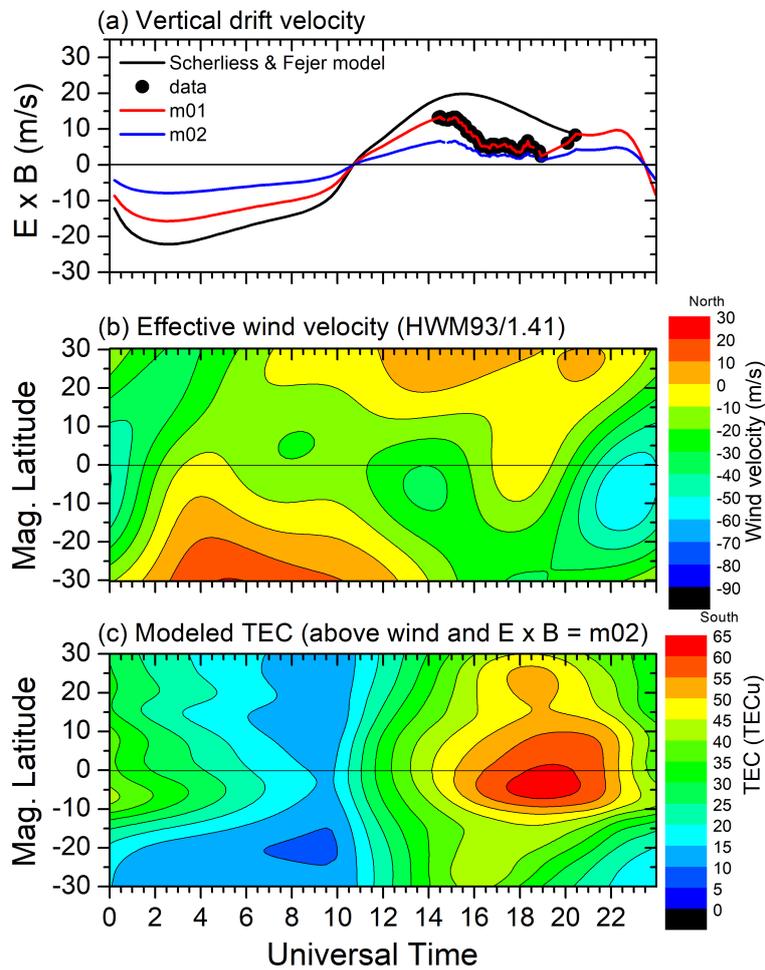
An alternative approach was considered by dividing values by a factor of 2.00 to adjust the effective meridional wind parameter. It means that the effective meridional wind is weaker than the one used as an input parameter in Figure 5.8c. The weaker vertical drift velocity, m02, was held constant and used as an input parame-

ter in the SUPIM-INPE model, along with the weaker meridional wind parameter, as illustrated in Figure 5.9.

Figure 5.9 - Same as Figure 5.8, vertical drift velocity m02 was held fixed, but the effective meridional winds changed by dividing it by a factor of 2.00 and both used as input parameters in the SUPIM-INPE model.
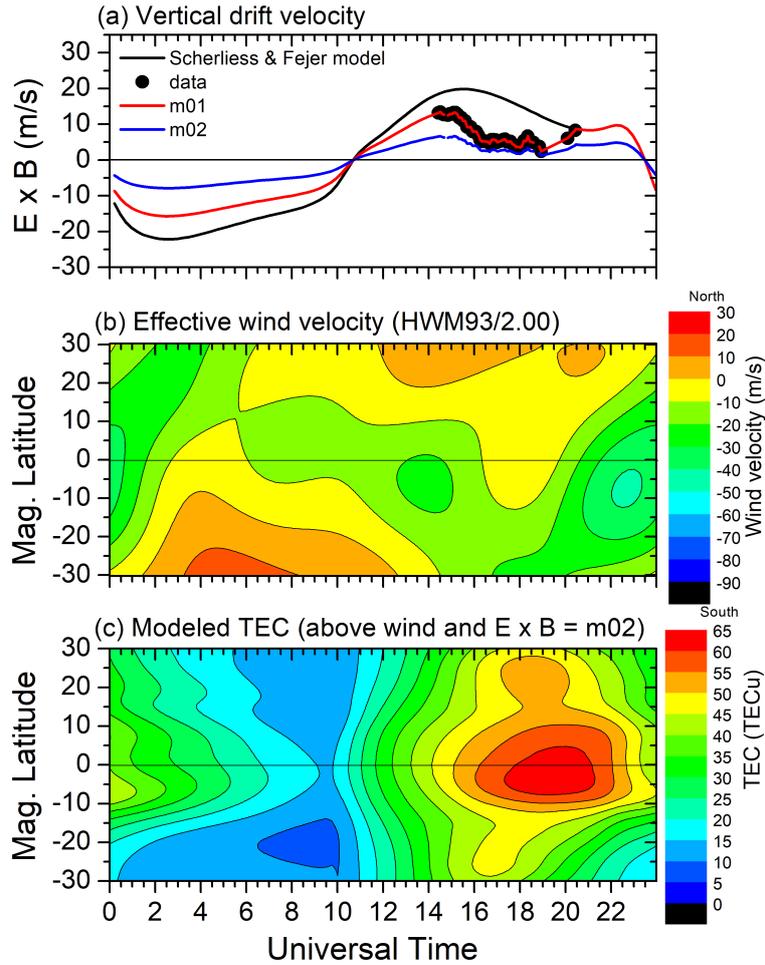
The modeled TEC reproduced by the model based on the adjustment made is shown in Figure 5.9c, with an intense ionization near the magnetic equator and some distribution of ionization above and below the magnetic equator. When the result from the observation data in Figure 5.4 is compared to the result from the model in Figure 5.9c, it can be concluded that both results are in agreement.

Thus, the model accurately reproduced the latitudinal crest position of the EIA

observed in Figure 5.4 by using a weaker vertical drift velocity and a less intense effective meridional wind as input parameters.

As a result of these observations, we can conclude that plasma from the magnetic equator regions is unlikely to be removed when the vertical drift velocity is low. As a result of the lower vertical drift velocity, the F-layer will not be uplifted as much as needed to form the EIA crests in both hemispheres.

It will, however, produce intense ionization near the magnetic equator and some degree of ionization distribution on each side of the dip equator, which is consistent with our observations and that reported by Dias et al. (2020). More importantly, aside from the lower drift velocity, the above observations show that less intense effective meridional wind played a significant role in the configuration of the latitudinal single crest position seen in Figure 5.4.

In conclusion, we have demonstrated that the daytime eastward electric field, as well as the meridional neutral wind, play a critical role in the establishment of the EIA by carrying plasma along the field lines. The combination of effective meridional wind and vertical drift velocity, according to this study, alters the latitudinal positions and intensity of the crests.

5.3   Month-to-month variation of the EIA

To analyze the month-to-month variations of the EIA at each magnetic meridian sector, the mean values of the TEC from daily keograms were estimated between 12:00 and 24:00UT, as indicated in section 4.1. The mean TEC values are then utilized to create a time series as a function of the month of the year and geographic/Dip latitude at the magnetic meridian 7.58° E sector in the year of 2014, as shown in Figure 5.10.

Figure 5.10 - Contour plot displays TEC variation a function of month of the year and geographic/Dip Latitude (left/right y-axis) from January (01) to December (12) 2014, between 12:00 and 00:00 UT.
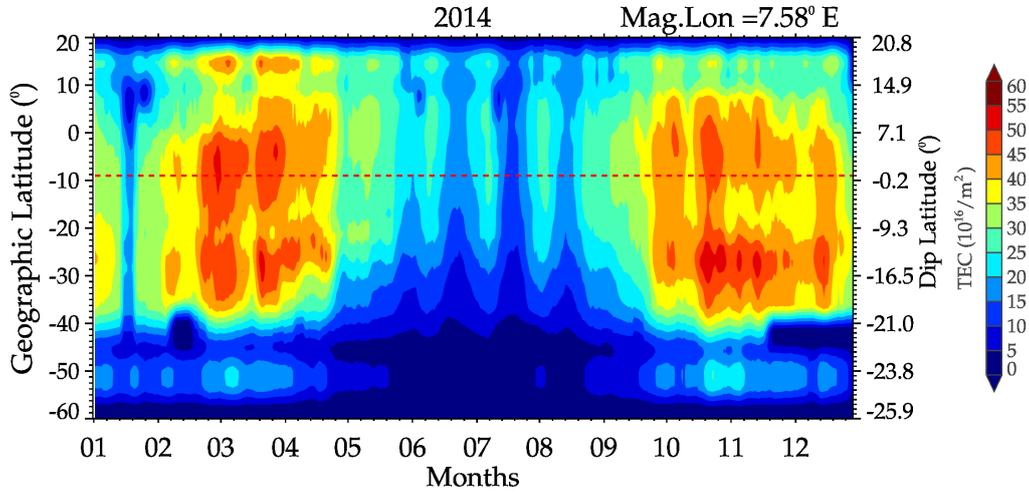
The months were classified into seasons to help understand the month-to-month variation of the EIA. Thus, November, December, January, and February correspond to the December solstice, March, April, September, and October to the equinox, and May, June, July, and August to the June solstice.

The variation in the EIA, as seen in Figure 5.10, shows significant changes in crest positions and TEC levels between the equinox (March and September) and solstice (June and December), revealing the EIA's monthly behavior.

The EIA crests TEC values are higher during the equinox months and lower during the winter solstice, as shown in Figure 5.10. The EIA crests are also more asymmetrical, intense, and visible at equinoxes than at solstices. December solstice and equinoxes show a more apparent trend of increased ion density.

This well-known monthly variation is primarily caused by changes in the pattern of meridional wind circulation (ARRIAGADA et al., 1997; KARPACHEV; GASILOV, 2001; MARUYAMA et al., 2008; ROMERO-HERNANDEZ et al., 2018; DIAS et al., 2020), which are caused by the temperature gradient, which causes the atmosphere to expand, resulting in neutral wind generation.

In general, semimonthly variations can be observed with maximum TEC levels at the crests during January, February, and March, and a minimum during June, July, and

August. The second maximum level occurs in September, October, and November.

In addition, the EIA southern hemispheric crests show a contraction from December solstice to June solstice in Figure 5.10. Meanwhile, from the December solstice to the June solstice, the northern hemisphere's EIA crests expand. Furthermore, some northward latitudinal distribution of the TEC above the geographic equator can be observed, primarily between February and April.

It is important to note that the anomaly pattern observed at the various magnetic meridians in this study exhibited a similar pattern but differed in shape, hemispheric crest positions, and intensities throughout the observed years.

Dias et al. (2020) investigated the daily and monthly variations of the equatorial ionization anomaly over the Brazilian equatorial and low-latitude regions. The authors used TEC data collected from various GNSS receivers in the year 2016, during the descending phase of solar activity. The EIA month-to-month characteristics were investigated using three longitudinally spaced sectors depicted as black lines on a map of South America in Figure 5.11.

Figure 5.11 - Top panel shows the 34 GPS-TEC stations used to study the EIA at eastern (green icons), middle (red icons), and western (yellow icons) Brazilian sectors. The left panel shows contour plots of EIA month-to-month variation as a function of UT and dip latitude from January to December 2016.
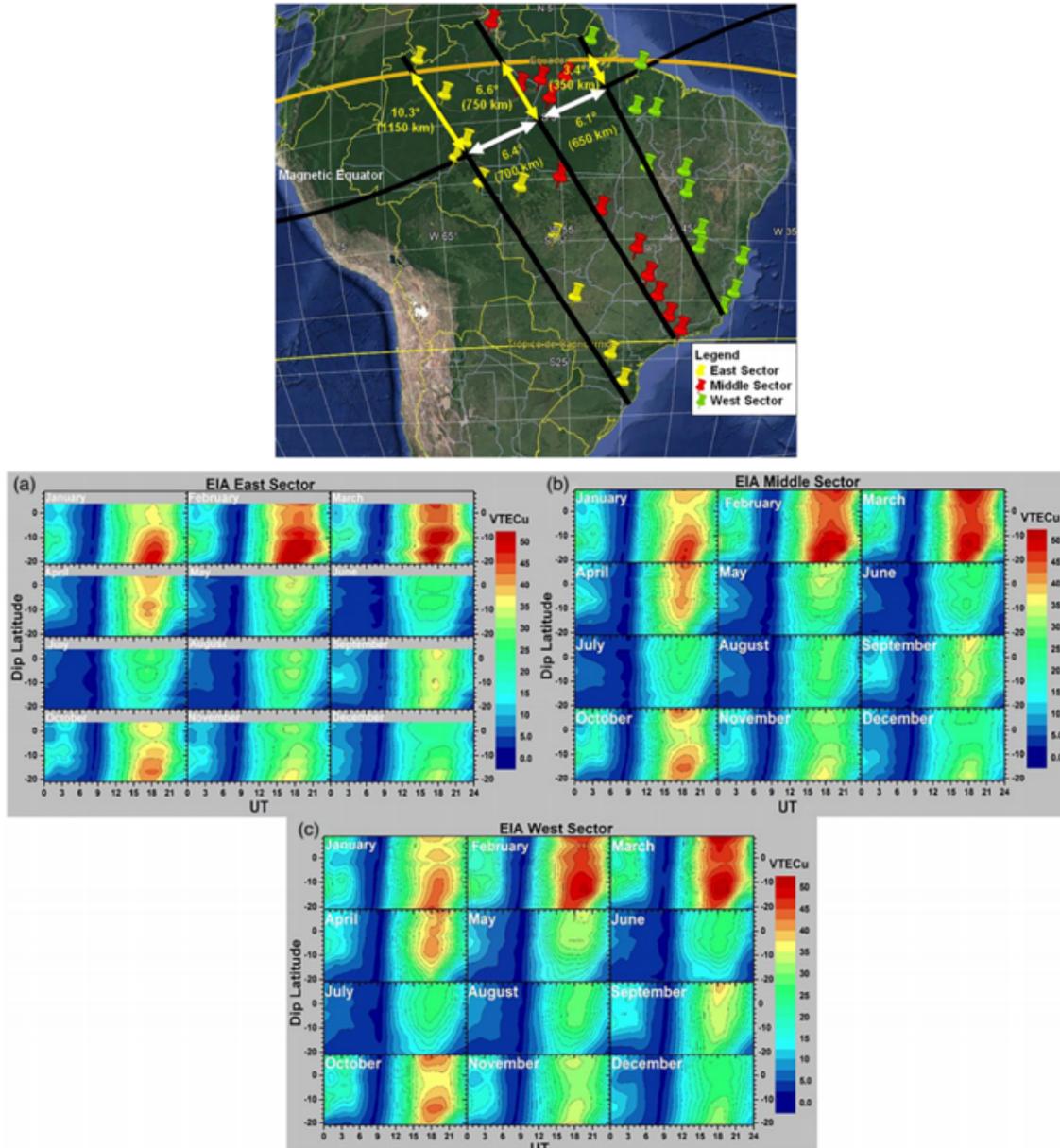
Source: Dias et al. (2020).

The longitudinal distances between the black lines are indicated by white arrows, indicating that the three sectors are separated by approximately ~ 700 km. The geographic and geomagnetic equators are separated by more than 1100 km in the west sector (yellow arrows).

Furthermore, the characteristics of monthly EIA variations in the eastern, middle, and western Brazilian sectors were investigated using the monthly mean diurnal variation of TEC at all GNSS receiver stations and the three longitudinal sectors. From January to December, the monthly mean contour plots of TEC as a function of UT and dip latitude are shown in the bottom panel of Figure 5.11a (east), Figure 5.11b (middle), and Figure 5.11c (west). As shown in the bottom panel of Figure 5.11, all sectors exhibit EIA semiannual variations, with maximum TEC at the crests in January, February, and March; minimums in June, July, and August, and a secondary maximum in September, October, and November.

It is important to note that differences in the shape and lifetime of the EIA crests are seen from month to month during the EIA major maximum, minimum, and secondary maximum periods within a short separation between the eastern, middle, and western sectors. The EIA crests and troughs between the three sectors show that the east and west sectors have shape and intensity (TEC) that are sometimes quite different. However, the middle sector exhibits similar EIA crests behavior to the east in some months and to the west in others. According to the authors, the observed differences in EIA crest morphologies at each sector are due to the effects of photochemical and dynamical processes.

Additionally, the EIA crests for the three longitudinal sectors are weaker or not developed from June to August. The majority of the plasma is concentrated over the geomagnetic equator. The EIA crests in the eastern sector are weakly developed in June, July, and August. Nevertheless, the EIA crests in the middle and west sectors are not well developed during those months, except in middle June, when it is very weakly developed.

The authors reported that the fountain effect was weaker during the winter months (June, July, and August) and did not have enough strength to form the EIA crests every day, as shown in Figure 5.11.

The EIA crests are less developed in September, especially in the east and middle sectors, where the two crests and troughs can be seen. However, the lifespan and longitudinal extension are both reduced. The EIA crests and troughs are not visible in the west sector, indicating that the EIA crests and troughs are not well developed. The strongest EIA crests can be seen in October, and they are very similar in all sectors, but the troughs in the middle and west sectors are a little wider than in the east sector.

The EIA crests are weaker in all sectors in November than in October. They proposed a possible explanation for the variations in EIA crests during those months by combining the strong fountain effect with the solar zenith angle during summer and the large distance between the geographic and geomagnetic equators. Moreover, our observation (Figure 5.10) shows that the EIA crests patterns exhibit similar trends and agree with the anomaly crests month-to-month characteristics reported by Dias et al. (2020).

Besides, as shown in Figure 5.11, TEC maximum near the magnetic equator, in the west, middle, and east sectors, primarily in January. These observed features were also seen in observations made at other magnetic meridian sectors in this study, primarily during the months of January and February. In the section 5.2, a good example of such feature is investigated intensively.

Furthermore, focusing on the June solstice, it is clear that the EIA crests TEC levels observed by Dias et al. (2020) during those months did not develop in the middle and west sectors. The EIA crests are exceptionally weakly developed in the middle sector in June, and these features of winter anomaly crest intensities are also present in our observations.

In general, the EIA crest intensities (TEC levels) observed at the various magnetic meridian considered in this work were weaker in the winter months than in other seasons. This observed behaviour is caused by seasonal variations in vertical drift velocity (KWAK et al., 2019). Furthermore, the daily mean TEC from each keogram used in the construction of the EIA's monthly variations resulted in the low level of TEC rather than the absolute values of TEC.

It can be concluded that the month-to-month variations of the EIA crests patterns observed agree with those reported by Dias et al. (2020) and Kwak et al. (2019).

Khadka et al. (2018) also investigated the effects of electric field and neutral wind on the EIA asymmetry. The authors used magnetometer measurements of equatorial electrojet (EEJ) currents and trans-equatorial neutral winds data from the Second-Generation Optimized Fabry-Perot Doppler Imager (SOFDI). The Low-Latitude Ionospheric Sensor Network (LISN) and several other networks in South America were also used to collect TEC data from GPS receivers.

According to them, the main drivers of the EIA monthly variations are the vertical $\vec{E} \times \vec{B}$ plasma drift associated with an eastward electric field (EEF) and geomagnetic

conditions, as well as the neutral wind field. The monthly variation of the EIA, showing its equivalent vertical TEC levels derived from LISN GPS receivers, is shown in Figure 5.12 from 2011 to 2013.

Figure 5.12 - Geomagnetic latitudinal profiles of month-to-month variability of EIA crests from 2011 to 2013.
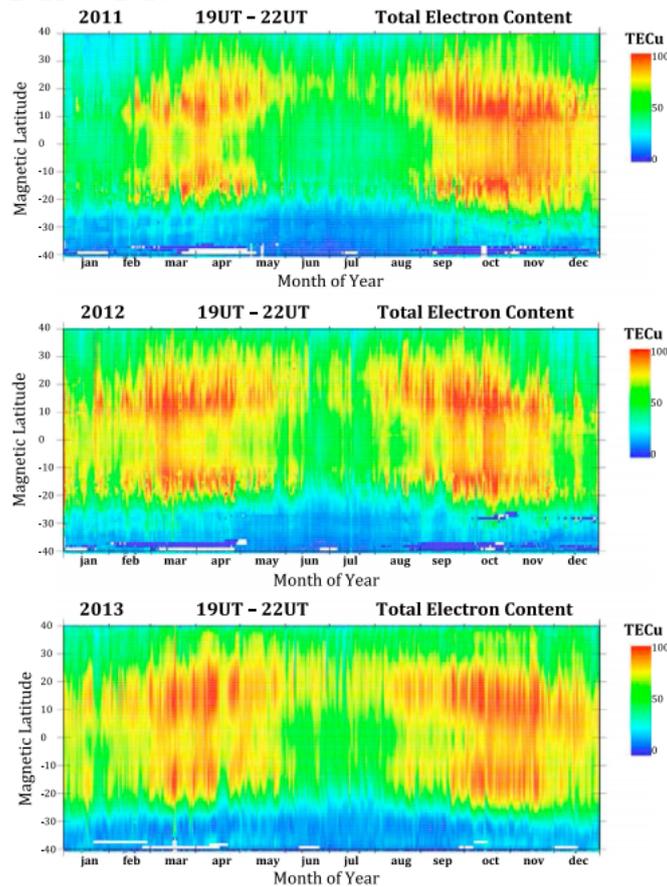
Source: Khadka et al. (2018).

It is clear from Figure 5.12 and our observations (Figure 5.10) that they followed a similar pattern in terms of the TEC level of the EIA crests. It is also worth noting that the magnitude of TEC has increased from 2011 to 2013. Furthermore, minor differences in the intensity of the EIA TEC levels at the crests can be identified. This could be because, as shown in Figure 5.12, the time interval used for the daily TEC average was between 19:00 and 22:00 UT for Figure 5.12 and 12:00-24:00 UT for our observation (Figure 5.10).

Khadka et al. (2018) used a week plasma drift velocity and measured neutral wind data from Jicamarca Incoherent Scatter Radar (ISR) in August 2011, from SOFDI

(GERRARD; MERIWETHER, 2011), to investigate the neutral wind effect on the monthly asymmetry pattern of the EIA crests.

The Low-Latitude IONospheric Sector (LLIONS) model was used to elucidate the role of the meridional component of neutral wind in the EIA asymmetry (VAL-LADARES; CHAU, 2012). They used a week of neutral wind data in August 2011, as shown in the bottom panel of Figure 5.13, along with simultaneous measurements of ISR drift velocity in the middle panel of Figure 5.13.

Figure 5.13 - Top: Contour plots of total electron content (TEC) distribution along 70°W on 7, 8, 9, and 10 August 2011. Middle: Average vertical plasma drift profiles in the ionosphere from Jicamarca Incoherent Scatter Radar (ISR). Bottom: Meridional wind velocity for each hour at Huancayo for 07, 08, 09, and 10 August 2011 in the western meridian of American low latitudes.
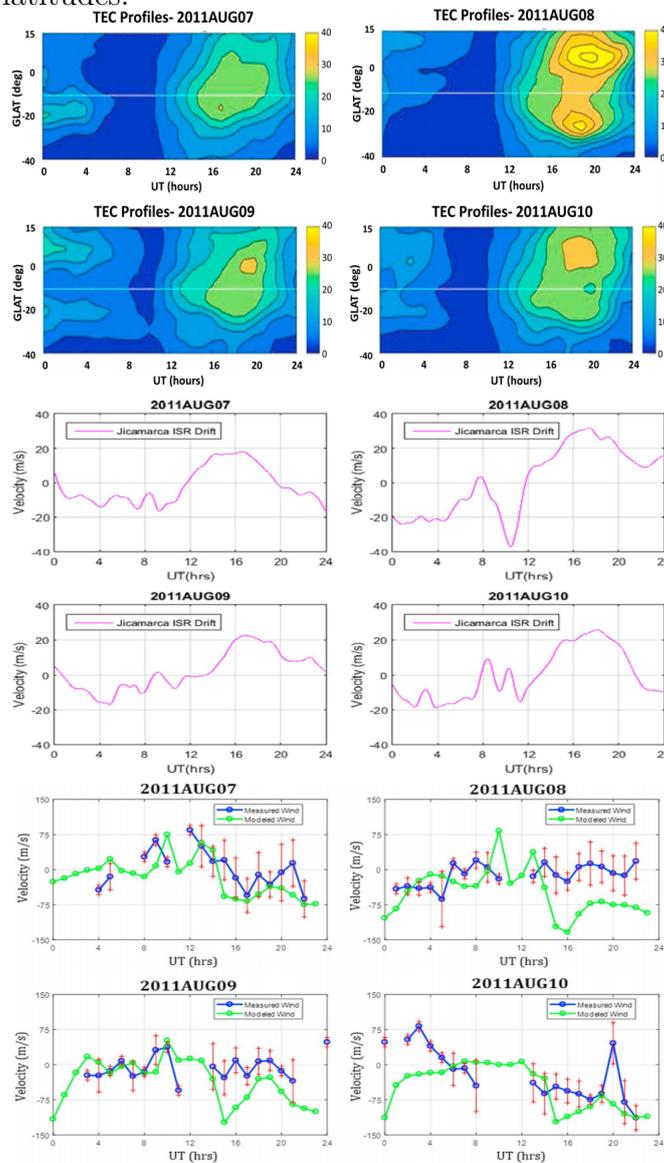
Source: Khadka et al. (2018).

On the 08 August 2011, an asymmetric EIA crest can be seen, with two intense crests in both hemispheres, with peak maximums at 17:00 UT and 18:00 UT, respectively. The asymmetry is due to the effect of meridional wind on that particular day. Furthermore, on 8 August 2011, the SOFDI winds fluctuate around zero, with no crest developing. The meridional wind was northward for more than 4 hours on 07

114

August, between 12:00 UT and 16:00 UT, causing plasma to move up to the field lines in the southern hemisphere and down in the northern hemisphere. The wind value near 20:00 UT for each plot exhibits the same effect.

On the day 07 August of 2018, a very weak vertical drift velocity can be seen, and the effect of this can be seen in EIA formation on that same day, where a significant accumulation of plasma was found near the magnetic equator. The combined effects of vertical drift velocity and winds result in these patterns of EIA crest location near the magnetic equator.

According to our observations, Figure 5.14 depicts EIA crests formation from 07 to 10 August 2014, at the meridian 0.22°W sector. It is worth noting that our meridian (0.22°W) falls within the geographic meridian sector (70° − 80°W) used by Khadka et al. (2018) in their studies.

Figure 5.14 - Contour plots of TEC distribution along magnetic meridian 0.22° W on 07, 08, 09 and 10 August, 2014.
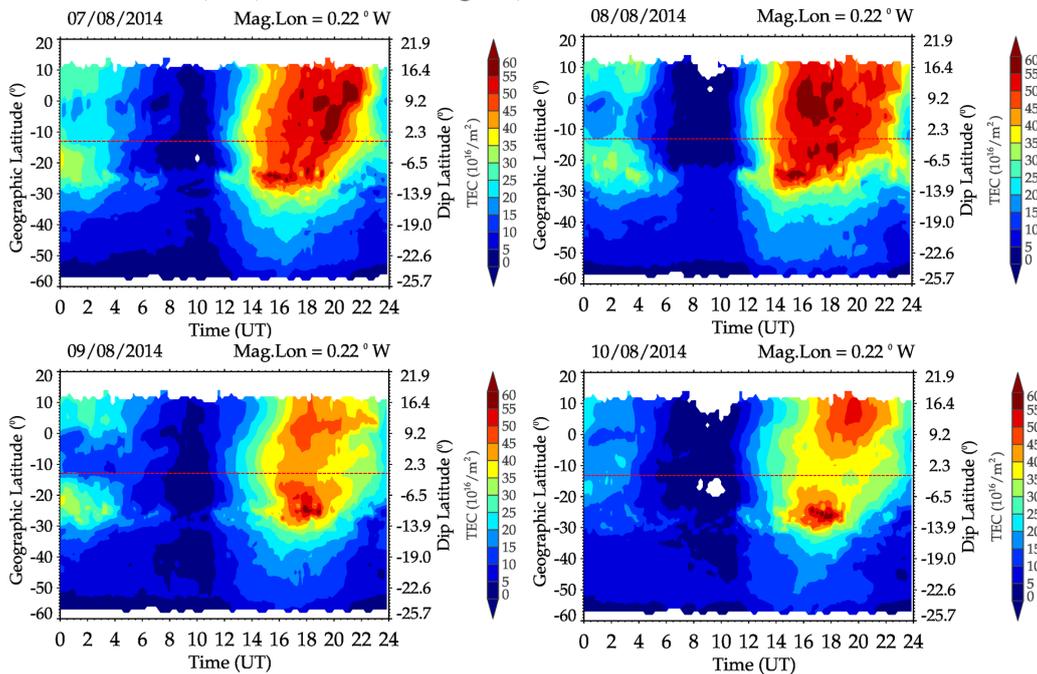
On the days 07 and 08, Figure 5.14 shows intense ionizations near the magnetic equator with some spread above and below the magnetic equator regions. Moreover, an interhemispheric asymmetry EIA crest formation with two intense crests at each hemisphere can be seen on days 09 and 10. The observed patterns of EIA crests are

similar to those observed by Khadka et al. (2018) (bottom panel of Figure 5.13).

When the features of the EIA crest observed by Khadka et al. (2018) on the day 07 are compared to our observations on the day 07, it can be seen that the EIA formed exhibits similar features. Both have maximum TEC formation around 18:00 UT, but with minor differences in intensity (TEC level). Based on the previous discussions in the section 5.2, it can be concluded that the anomaly crest morphology and latitudinal locations were caused by the weaker vertical drift velocity and northward meridional wind observed on that day.

Besides, the month-to-month EIA variation in Figure 5.12 demonstrates the same seasonality pattern as our observation (Figure 5.10). Interestingly, the northward spread of TEC (intensities) from February to April can be seen in Figure 5.10 and Figure 5.12, respectively. This northward spread has been linked to various motions produced by a wind dynamo (KHADKA et al., 2018).

Consequently, the monthly variation of the EIA's asymmetries, which are stronger in December solstice and equinox than in June solstice, is controlled by the monthly variation of the vertical drift and meridional wind. Furthermore, the anomaly crests in Figure 5.12 are more symmetric in equinox seasons than in solstices, and this behavior can be seen in our observations at each magnetic meridian used in this work.

These similarities, differences, and characteristics of month-to-month EIA variations have been associated to the seasonal dependence of vertical drift and meridional wind (FEJER et al., 1991; KHADKA et al., 2018; MARUYAMA et al., 2008; KARPACHEV; GASILOV, 2001; ARRIAGADA et al., 1997). As a result, it is possible to conclude that the month-to-month EIA variation features/patterns agree with those observed by Khadka et al. (2018).

In conclusion, the meridional winds and vertical drift velocity play an important role in the monthly variation of the latitudinal distribution of the EIA crests. Furthermore, dynamic forces are known to control the day-to-day and month-to-month variations of the EIA (ZOU et al., 2000; FAGUNDES et al., 2005; YAMAZAKI et al., 2018; MO et al., 2018).

The following section will look into the possible physical dynamics processes (such as tides and planetary waves) and solar flux activity dependence that could cause variations in the southern EIA crest.

5.4 Dynamic mechanisms responsible for the day-to-day longitudinal variation of EIA

The equatorial and low latitude ionospheric variability due to wave oscillations such as tides, gravity and planetary waves has been a subject of interest to the space weather community (CHEN, 1992; FORBES, 2000; FAGUNDES et al., 2005; FORBES, 1996; GONCHARENKO et al., 2013; LIU, 2016; PANCHEVA et al., 2010; PEDATELLA et al., 2012; GAN et al., 2016; YAMAZAKI et al., 2018; GU et al., 2014; GU et al., 2018; TAKAHASHI et al., 2005; TAKAHASHI, 2012; MO; ZHANG, 2020a).

In general, some pathways have been proposed to understand the upward coupling of these wave oscillations with the ionosphere thermosphere system. One frequently proposed explanation is that wave oscillations permeate into the ionospheric E region, modulating winds and causing changes in electric fields. Thus, generating wave-like oscillations in ionospheric electron densities (FORBES, 2000; MO; ZHANG, 2020a; GU et al., 2018; YAMAZAKI et al., 2018; TAKAHASHI, 2012).

Recent studies, however, have revealed that the equatorial ionization anomaly exhibits some evidence of wave oscillations (YAMAZAKI et al., 2018; MO et al., 2018).

For possible periodic oscillations, the EIA south crest positions estimated at the magnetic meridian 26.70°E were investigated. The magnetic meridian (26.70°E) was chosen because it passes through the sector where coincident data were obtained for comparison purposes. Data from ground-based Fabry-Perot Interferometers (FPI) and Digisondes instruments were used to calculate thermospheric wind and maximum ionization height of the F layer ($hmF2$).

A Morlet wavelet transform was applied to daily EIA southern crest positions to investigate the temporal behavior of oscillations. The wavelet spectra were calculated over a period range of 2 to 32 days. The time series of EIA crest latitudinal positions as a function of day of the year (DOY) is shown in Figure 5.15a.

Figure 5.15 - (A) Times series, (B) Wavelet spectrum and (C) Amplitude of the 3-4
day oscillation filtered out from the southern hemispheric crest positions
of the EIA at the magnetic meridian 26.70°E in 2014. The dashed white
line is the 3.5 day oscillations. The regions enclosed with the black lines
depicts the 90% confidence levels.
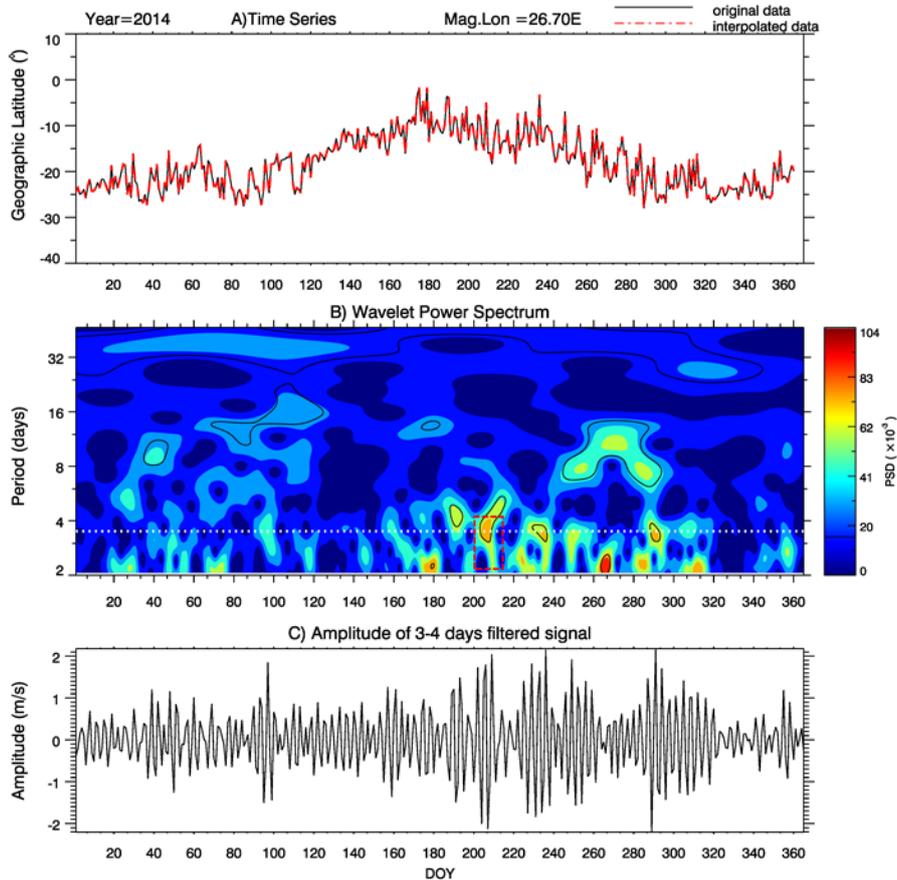
The Morlet wavelet power spectrum is shown in Figure 5.15b, and the amplitude of a
3-4 day filtered signal is shown in Figure 5.15c, both at magnetic meridian 26.70°E.
The south crest positions of the EIA move to low-latitude during the December
solstices and northward during the June solstices, as shown in Figure 5.15a. The
trend of the EIA south crest positions is similar to what was observed at the various
magnetic meridians used in this study.

Various wave packets with periods ranging from 2 to 32 days can be seen from
the EIA spectrum's south crest positions. The strongest 2.5 day oscillations are seen
around the days 260-266. Day oscillations of 3-4 can be found between days 200-212,
230-240, and 285-290, respectively. Other oscillations of 8-day, 16-day, and 10-day
can also be seen extending from day 35-40, 60-115, and 240-285.

A bandpass filter was applied, centered on the periods between 3 and 4, and the resulting time series is shown in Figure 5.15c as a time series for days 1-365. We focus our discussion in this work on the 3-4 day oscillation. Following the filtering process, a period near the 3.5-day oscillation was identified as dominant and required further investigation, as shown in Figure 5.15b as a white short dash line.

5.4.1 3-4-days oscillation

In order to investigate the 3-4 day oscillation observed from the EIA South crest positions in the Morlet wavelet power spectrum near the days 200 to 212 (represented as a rectangular red dash line), as shown in Figure 5.15b, coincident observations from ground-based instruments will be used.

Thermospheric wind data collected by a Fabry-Perot Interferometer (FPI) at Cajazeiras (3.8°S, 38.6°W, dip angle 11°S) were used. The meridional (south-north) and zonal (east-west) thermospheric wind measurements were obtained by OI 630.0 nm (red line) airglow emission at an altitude of ~ 250.0 km between the days 200-212 (i.e., 19-31, July) of 2014.

The winds from the FPI were calculated from the Doppler shift of the fringes of the emission layer line spectrum. The time resolution of the wind measurement is ~ 5 min. More details and explanations of FPI and instructions on the data processing and techniques can be found in (MERIWETHER et al., 2008; MAKELA et al., 2012; ENGLERT et al., 2012; FIGUEIREDO et al., 2017; FISHER, 2013; LOMOTEY, 2016).

The measured thermospheric winds were used to calculate the north, south, east, and west wind components. The wind measurements were subjected to a Lomb-Scargle periodogram analysis to determine the presence of an oscillation with a period of 3-4-day. The thermospheric zonal (meridional) wind component as a function of DOY is depicted in Figure 5.16 (top/bottom panels) along with their respective periodogram. The short red dashed line represents the 90% significance level. Figure 5.16 (top/bottom panels) shows evidence of an oscillation with a period near 2.5- and 3.0-day in various thermospheric wind components. The most prominent oscillation is 3.0-day, which can be found in all wind components.

Figure 5.16 - Time series of nighttime thermospheric winds measurements and Lomb Scargle periodograms of winds measurement from Fabry-Perot Interferometer (FPI) at Cajazeiras (3.8°S, 38.6°W, dip angle: 11°S) from July 19 to July 31, 2014. The Zonal components of wind (top panel) are respected by East and West, the meridional component is represented by South and North components (bottom panel). The dashed red line depicts 90% significance level.
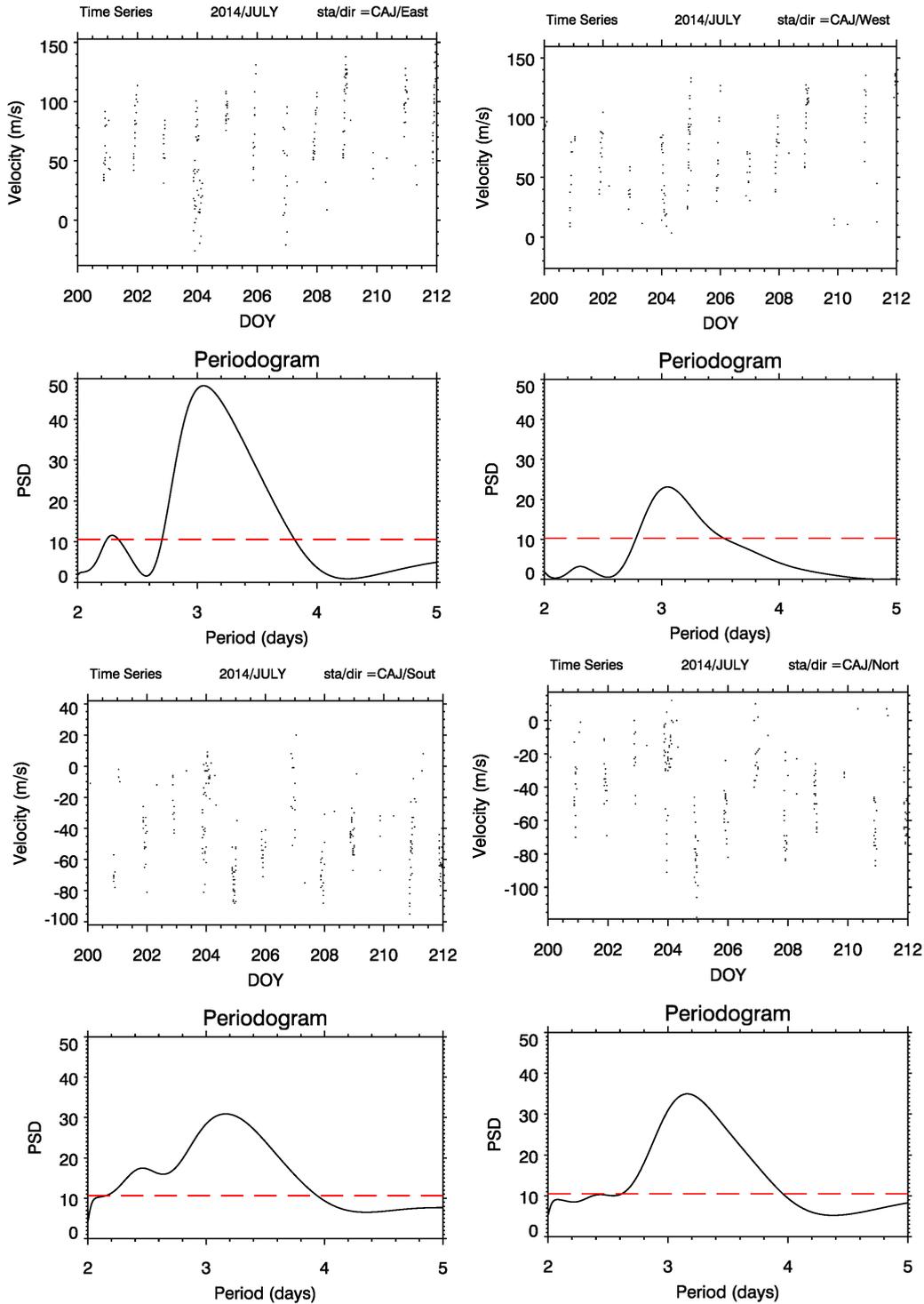
Ionospheric data measured by Digisonde, which operates as a pulse radar system with a wide-band 10 kW peak power transmitter and precise fast-switching frequency synthesis and is located at São Luís (2.33°S, 44.2°W, dip angle 2.7°S).

The frequency of operation is one ionogram every ten minutes. The maximum ionization height of the F layer ($hmF2$) is the ionospheric parameter used here. The F-layer is uplifted after sunset, and the F-region dynamo process is driven by thermospheric zonal wind. A specific local time was chosen to observe the uplifting.

Evening vertical drift velocity was used by Abdu et al. (2006) and Takahashi (2006) to observe the uplifting effects. In this study, a local time of 20:00 LT (23:00 UT) was chosen as the time when $hmF2$ reaches its maximum height on most nights.

Figure 5.17 - Top: Nighttime ionospheric $hmF2$ time series. Bottom: Lomb Scargle periodogram (LS) from July 19 to July 31, 2014, observed at São Luís (2.33°S, 44.2°W, dip angle: 2.7°S) at 20:00 Local Time.
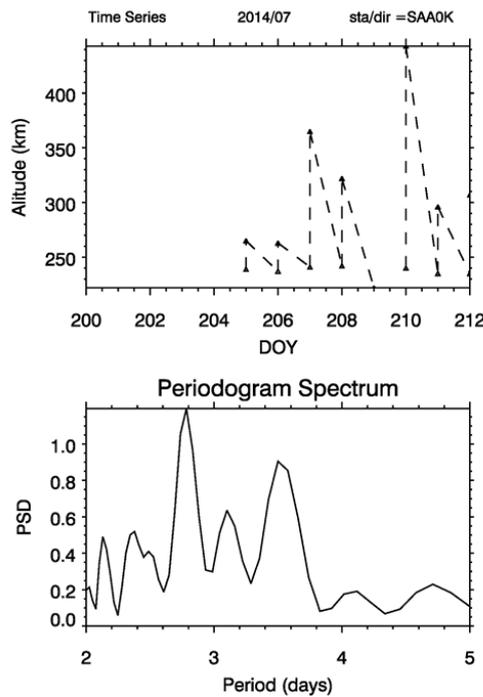
The nighttime ionospheric $hmF2$ parameter as a function of DOY is depicted in Figure 5.17 (top/bottom panels) along with its corresponding periodogram. On the periodogram spectrum, oscillations with periods near 2.0-,2.5-, 3.0-, 3.5-, 4.0-, and 4.5-days can be seen.

When the periodogram spectra are compared to those of the thermospheric wind and the nighttime ionospheric $hmF2$ parameter, it is possible to see the presence of a common oscillation with a period of 3.-3.5-day. According to the literature, (WALLACE; KOUSKY, 1968; HIROTA, 1979), the 3.5-day oscillations detected could be an equatorial Kelvin wave.

Kelvin waves are atmospheric wave oscillations that propagate eastward and are classified as slow (16-day) (WALLACE; KOUSKY, 1968), fast (6-day) (HIROTA, 1979), and ultra-fast (3.5-day). These Kelvin wave categories have been detected in a variety of ground-based instruments, including airglow measurement with a multichannel photometer and Mesosphere and Lower Thermosphere (MLT) wind measurement with meteor radar, (TAKAHASHI et al., 2002; PANCHEVA et al., 2004; EGITO et al., 2017).

Egito et al. (2017) used airglow from a multichannel photometer and wind measurements from a meteor radar over the Brazilian sector to investigate the presence and effects of the 3-4-day wave in the MLT regions over the equatorial region. They discovered 3-4-day oscillations in airglow and wind that occur intermittently throughout the year (i.e., January, March, July, August, and November). Furthermore, the observed 3-4 day oscillations were attributed to an Ultra-Fast Kelvin wave.

Takahashi et al. (2002) observed a 3.5-day oscillation in ground-based mesospheric airglow measurements. Pancheva et al. (2004) identified 3.5-day wave oscillations in the meridional and zonal wind components of the MLT wind data analysis from Ascension Island.

A 3.5-day Ultra-Fast Kelvin wave plays an important role in the variability of the lower thermosphere and ionosphere system, according to observations made by Egito et al. (2017), Takahashi et al. (2002), Pancheva et al. (2004), and Forbes (2000). They are noted to have a long vertical wavelength (> 50 km). By penetrating into these regions and transporting energy and momentum from the troposphere region, they could trigger alterations in electrodynamic processes in MLT and thermosphere regions (100-150 km).

Additionally, according to Forbes et al. (2009), Ultra-Fast Kelvin waves can be detected on rare occasions throughout the year, although their amplitude varies by 20-60 days. Kelvin waves are also known to influence the ionosphere in the equatorial region.

At the time of sunset and evening, the F-layer is lifted ($\vec{E} \times \vec{B}$ drift) due to the eastward E-field generated by the F-region dynamo (RISHBETH, 1971). The generated E-field depends on the zonal wind (U) and E-region conductivity:

$$E_z = U_y \times B_0 \left(\sum_F / \left(\sum_F + \sum_E \right) \right), \tag{5.1}$$

where U_y is the thermospheric zonal wind (at $\sim$ 200 km) and B_0 is the Earth's magnetic field intensity, $\sum_E$ and $\sum_F$ are the integrated conductivities of the E-and F-regions (ABDU et al., 2003; TAKAHASHI, 2006).

Thus, the day-to-day variability of $hmF2$, $foF2$, and TEC is also caused by the zonal wind system in the lower thermosphere. Moreover, assume that the Kelvin waves penetrate the MLT region even to E-region heights (100 to 120 km). In that case, they could modulate the local diurnal tidal wind system (mainly zonal), resulting in a variation in the electron conductivity. Assume that the waves penetrate even higher, from 150 to 200 km. In that case, they could modulate the lower thermosphere zonal wind velocity directly, resulting in direct modulation of the $\vec{E} \times \vec{B}$ drift, which is the primarily driven force responsible for the EIA formation.

On the other hand, the effects of solar flux activity on the EIA crests positions have been established in the literature (TAKAHASHI et al., 2014b; MO; ZHANG, 2020b; LI et al., 2018a). However, using TEC maps from GNSS receivers, Takahashi et al. (2014b) investigated the daily variation of the EIA crests to troughs over the Brazilian sector at a given local time (1500) and for the longitude sector of 50°W.

Their results revealed a larger amplitude of TEC values at the crest (18°S) as compared to the trough regions. The authors find out that the TEC at the magnetic equator showed similar changes to that of solar flux (F10.7), as illustrated in Figure 5.18.

Figure 5.18 - Right panel represent day to day variation in the maximum TEC (a)
at the equator and (b) at 18°S at the 50°W longitudinal zone. (c) Solar
radio frequency flux F10.7 and the left panel is Wavelet analysis of the
maximum TEC at the magnetic equator, middle and F10.7 flux, from
January (DOY 1) to December (DOY 365) in 2011.
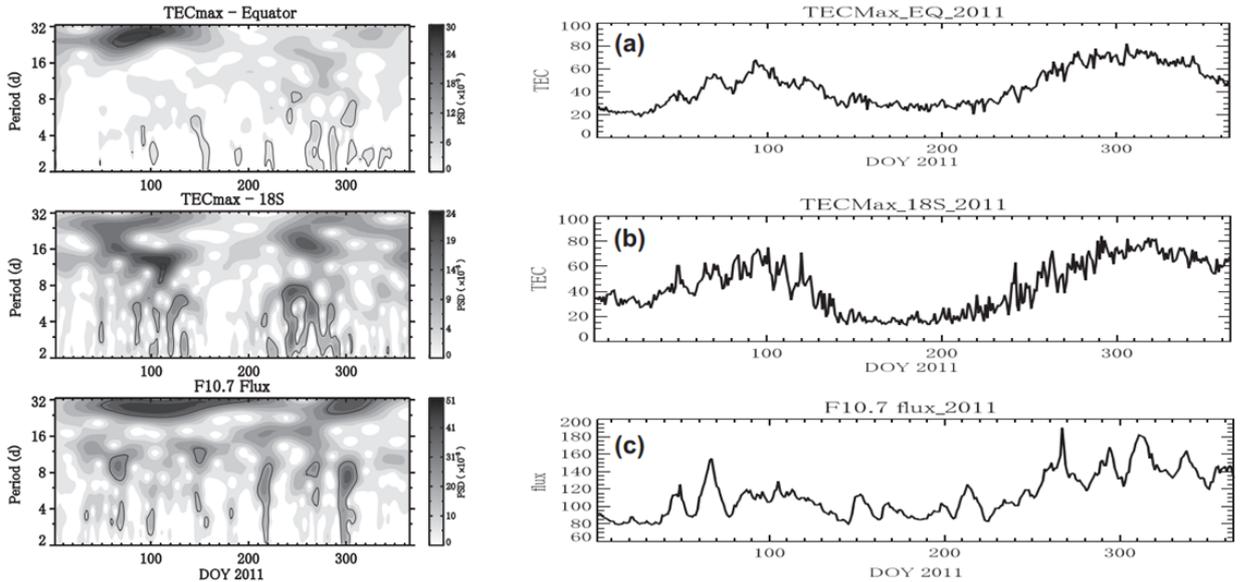
Soure: Takahashi et al. (2014b).

The TEC at the magnetic equator and crest regions had periods of two days or
more. As demonstrated in Figure 5.19, the daytime EIA crests may be influenced by
additional dynamic forces, such as planetary waves, rather than just solar activity.
As a result, the observed 3.5-day oscillation may be influenced by solar activity.
Possible oscillations in the solar flux (F10.7) were investigated.

Figure 5.19 - Top panel represents day-to-day variation and the below panel is wavelet analysis of the Solar radio frequency flux F10.7 ,from January (DOY 1) to December (DOY 365) in 2014.
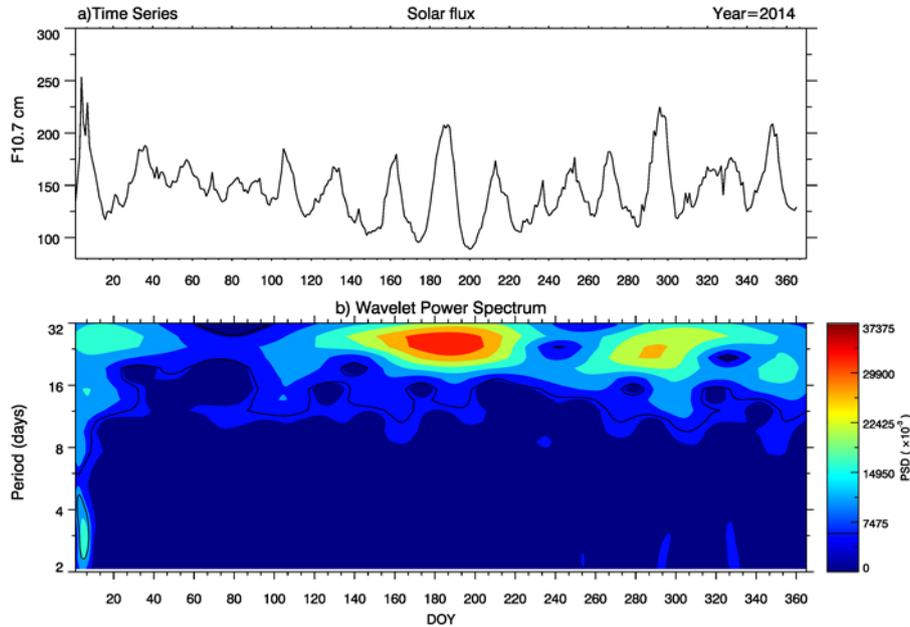
In Figure 5.19, the time series of day-to-day oscillations in solar flux (F10.7) (top panel) and wavelet analysis (bottom panel) are shown. The data for solar flux (F10.7) was obtained from the OMNIWeb data explorer (AERONAUTICS; (NASA)., 2021). Significant variations in solar flux (F10.7) can be seen in Figure 5.19a, and more importantly, the wavelet spectrum (Figure 5.19b) shows an oscillation with a period of 3-4-days occurring between the day of year 1-12.

In addition, a period of roughly 8-16 day oscillation can be noted around the days 1-25. However, the time range of 200-212 days, which is the subject of the investigation, the presence of oscillations having a period near 3.5-day cannot be identified.

When comparing the packets of oscillations observed in the wavelet spectrum of the TEC values at the crest (18°S) and trough (longitude 50°W) regions in Figure 5.18 to our observation in Figure 5.15, it becomes clear that between Figure 5.18, which depicts TEC, and Figure 5.15, which depicts crest positions, there are certain common times of oscillations. The 3.5-day oscillation can be seen near days 200-220, and additional oscillations, such as the 2.5-day and 4-day, can be seen between days 260 and 300, respectively. Also visible in the spectrum is the presence of a $\sim$ 27 day period, which will be explored in the next section.

As a result, the 3.5 oscillation seen in the EIA southern crest positions, thermospheric wind, and ionospheric parameter was visible in the TEC values at the crest (18°S) and trough (longitude 50°W) areas, as observed by Takahashi et al. (2014b). This shows that the 3.5-day oscillation and other oscillation packets detected in our investigation are unaffected by solar activity.

Our findings are consistent with those of Takahashi et al. (2014b), suggesting that the daytime EIA crests may be influenced by other dynamical processes, such as planetary waves, rather than just solar activity.

The 3.5-day oscillation in EIA south crest positions could be propagating upwards from the stratosphere to the mesosphere and lower thermosphere. Thus, interact with the ionosphere, modulating E-region conductivity and the F-region dynamo.

This mechanism could also be important for day-to-day variations in the EIA and other ionospheric irregularities, such as the formation of equatorial plasma bubbles. Because of the absence of observational instrumentation in other sectors, the observed 3.5-day oscillation in the EIA south crest positions could not be identified as planetary wave oscillation. As a result, more studies are needed to determine whether the oscillation seen is a planetary wave-type oscillation.

5.5 EIA variation during solar cycle descending phases

The production of plasma in the ionospheric F-region is mainly due to solar extreme ultraviolet (EUV) and X-ray. F-region is also strongly dominated by the transport processes. Furthermore, extreme variations in solar radiation and geomagnetic activity influence the production of free electrons in the ionosphere (BARON et al., 1983; FORBES, 2000; ABDU et al., 2008; LI et al., 2018b; RAO et al., 2018), resulting in significant impacts on civil radio communication (KUTIEV et al., 2012; WELLS, 1943) and satellite orbital stability (WALTERSCHEID, 1989). In this section, the EIA crests intensities will be briefly be discussed during descending phases of the solar cycle (i.e., 2014-2019).

A typical example of the yearly (2014-2019) variation of the EIA crest intensities observed at the various magnetic meridian sector considered in this work is illustrated in Figure 5.20 at magnetic meridian 3.36°E. The EIA crests features observed in Figure 5.20, exhibits a similar pattern but with slight differences concerning its shapes and TEC levels (intensity). Additionally, the NH has fewer GNSS receivers, which means the data for such locations is less representative. As a result, the north crest

analysis is less precise than the south crest analysis, with better receiver coverage.

Figure 5.20 - Yearly variability of the EIA from 2014 to 2019 as observed at magnetic meridian 3.36°E sector.
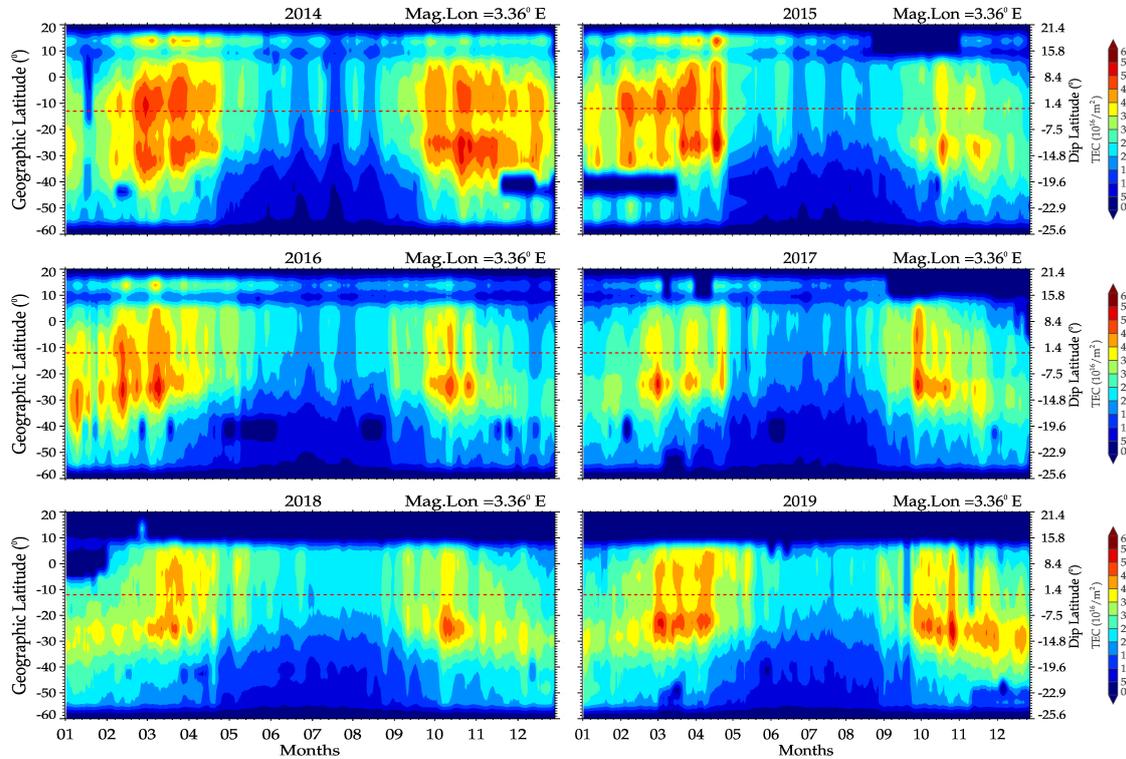
From 2014 to 2015, it can be noticed that the EIA intensity exhibits a decrease in TEC values. The TEC of the EIA crests demonstrates significant semimonthly changes, as previously indicated in section 5.3, with the EIA increasing in December solstices and equinoxes while gradually decreasing in June solstices. Furthermore, the 27-day period found in Figure 5.19 shows that the solar rotation period, which is 27 days, is the cause of semimonthly variation.

Moreover, compared to previous years, the intensities of the EIA crest decrease significantly during the equinoxes and December solstices from 2016 to 2017. However, when focusing on the solar minimum phases (2018-2019), it can be seen that the intensities of the EIA crests appear to be stronger in the southern hemisphere than in the northern hemisphere. In June solstices, however, low level or weak anomaly crests can be seen.

In general, the results of the EIA crest intensities show a semiannual anomaly, with

two maxima appearing in March/April and December/January and minima appearing in June/August over the years. Furthermore, it can be seen in Figure 5.21 that the intensities of the EIA decrease evidently over the years of the solar descending phases. Predominantly, from November to December, the TEC levels of EIA crests have weakened over the years, except for 2018-2019, when the EIA has shown a slight enhancement.

The hemispheric asymmetry during the December and June solstices shows a slightly different variation with the solar descending phases, but a general tendency exists. EIA crests intensities during the solar minimum phases, especially in the winter months, gradually decrease over the years. In addition, at solar maximum phases, a stronger EIA is formed in the summer and equinoxes. Some researchers discuss such formation of the hemispheric asymmetry and its variation by the combined effects of the fountain process and summer-to-winter wind (KWAK et al., 2019).

Batista et al. (2017), studied the occurrence of the F_3 layer using ionospheric data from low-latitude north and south of the geomagnetic equator at roughly the same magnetic longitude. Their research shows that the bottomside F-layer thickness parameter, B_0, is larger in the summer hemisphere than in the winter due to the formation of the F_3 layer. They also show that there is inverse behavior of critical frequency (foF2). According to our results, the intensities of the EIA crests follow the B_0 variations, i.e., the summer hemisphere crest is larger than the winter during the solar descending phases.

Also, Balan et al. (1998) revealed the process for the development of this layer (F_3). According to them, at least three criteria are required for the formation of the F_3 layer: (1) upward vertical drift (eastward electric field), (2) equatorial meridional wind, and (3) the regular photochemical and dynamical processes that build the regular F layer.

Furthermore, as found by Batista et al. (2017), the F_3 layer formed at the Southern Hemisphere station lasted for a longer period of time during the December solstice, and its occurrence is greatest at times of maximum northward effective meridional wind. This means that the peak heights of the F layer were higher in the Southern Hemisphere than in the Northern.

Moreover, the F_3 layer that forms at the June solstice at the Northern Hemisphere station lasts for a longer time, and its occurrence is greatest at the time of maximum southward effective meridional wind. This means that the F layer peak heights in the

morning are higher at the Northern Hemisphere station than at the Southern Hemisphere station. Based on the Horizontal Wind Model analysis of effective meridional wind, they determined that wind played a significant impact in the asymmetry of the F layer peak height seen at the two stations during both quiet and disturbed times.

Based on the findings of Batista et al. (2017) and the mechanisms provided by Balan et al. (1998), it can be shown in our observations (Figure 5.20) that EIA crests in the Southern Hemisphere are more intense than in the Northern Hemisphere, and the contrary occurs during the June solstice along the solar cycle descending phases. According to Batista et al. (2017), the observed alterations can be attributable to the effective meridional.

During the solar maximum, descending, and minimum phases, the equinoctial asymmetries observed in the six years showed a considerable decrease in EIA intensities and latitudinal distance around magnetic equator regions. However, we assume that the variations in EIA crest intensities are related to solar activity somehow. In solar maximum phases in December solstices and equinoxes, higher TEC levels of EIA crests were found, with a decrease in June solstices.

Yue et al. (2015) also studied the morphology of EIA during 2006-2014, using ionospheric peak density (NmF2) and peak height (hmF2), derived from a large number of GPS radio occultation electron density profiles. They observed an evident solar activity variation of the EIA, and both NmF2 and hmF2 magnitudes decreased from 2006-2008/9 (solar minimum) and then increased gradually due to the solar activity enhancement, as shown in Figure 5.21.

Figure 5.21 - Monthly local time-magnetic latitude maps of NmF2 and hmF2 during May 2006-Dec 2014.
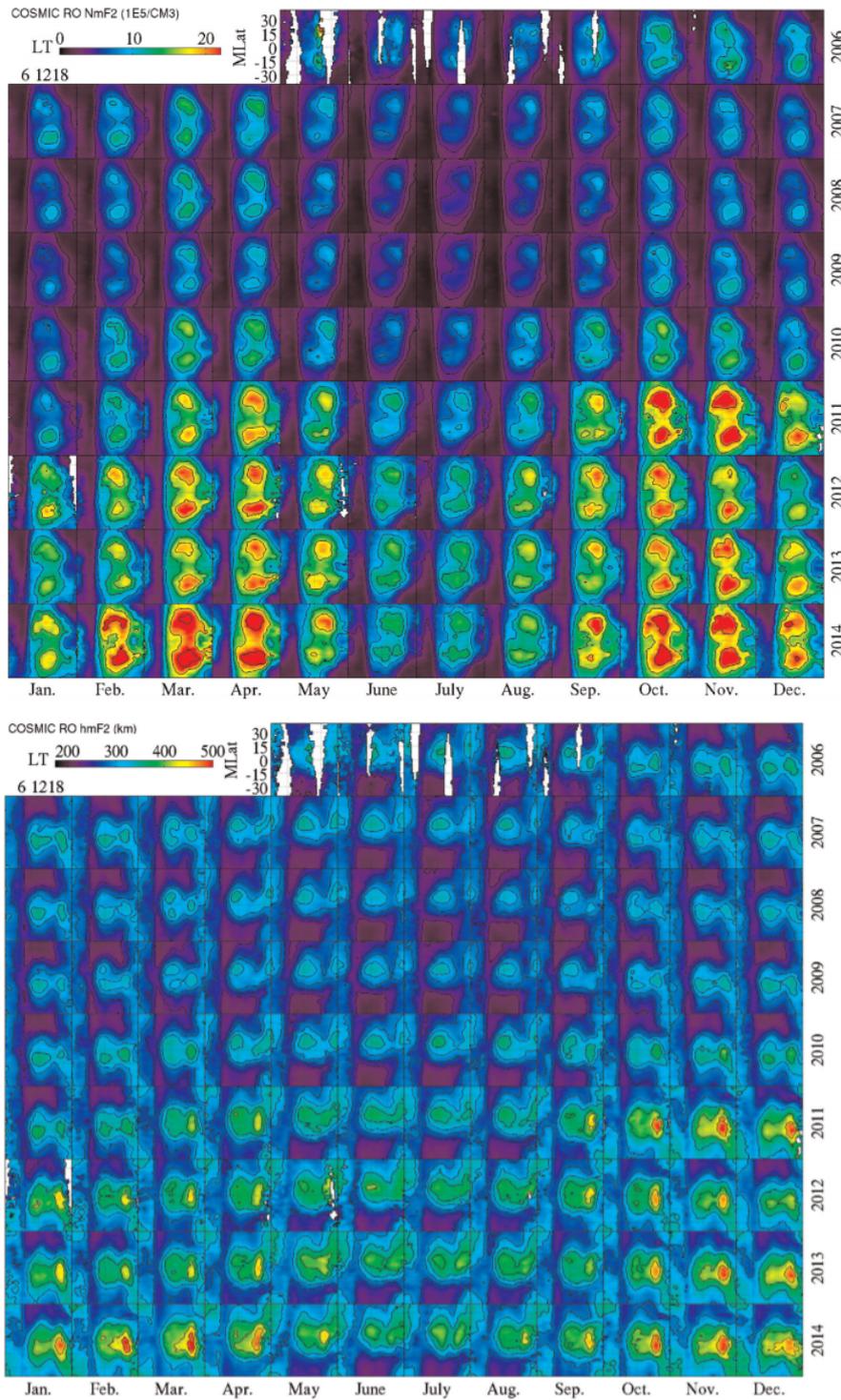
Source: Yue et al. (2015).

In Figure 5.21 shows the monthly mean local time (LT)- magnetic latitude (MLat) map of NmF2 and hmF2 during May 2006-Dec 2014 period, respectively. In addition,

it can be noticed that the ionospheric peak parameters exhibited a strong semiannual variation. Especially, both the NmF2 and hmF2 are higher in equinox than those in the solstice. According to the authors, the semiannual variation of middle and low latitude ionosphere can be well understood by the $O/N2$ variations through both the simulations and data comparison.

Moreover, simulations and evaluations conducted by Qian et al. (2013) using data from the Constellation Observation System for Meteorology, Ionosphere, and Climate (COSMIC) confirmed that turbulent mixing of atomic and molecular gas composition drives annual and semiannual variations in the ionosphere. When comparing the decreasing in EIA intensities in Figure 5.21 to our observation (Figure 5.20), it can be seen that they both follow the same trend, with slight differences in interhemispheric positions.

Finally, climatological investigations of EIA crest intensities during solar cycle descending phases were studied over the Southern American region. According to our observations, the intensity of the EIA crests varied significantly with solar activity. More research is needed, such as a correlation analysis of TEC at the magnetic equator and southern crest with the solar flux index, as well as statistical correlations with other modulations, such as lunar tides, to see if there are any overlapping effects on observed changes.

6 CONCLUSIONS

The current study investigated and characterized the longitudinal variability of Equatorial Ionization Anomaly (EIA) using Total Electron Content (TEC) data from ground-based Global Navigation Satellite System (GNSS) receivers at different magnetic meridian sectors over the Southern American sector. Long-term (i.e., from 2014 to 2019) EIA observations were combined with simulations at the Instituto Nacional de Pesquisas Espaciais using the Sheffield University Plasmasphere Ionosphere Model (SUPIM-INPE).

Over the Southern American sector, a comprehensive study of the Equatorial Ionization Anomaly (EIA) along Southern American magnetic meridian lines was undertaken. Various characteristics of the EIA crests in terms of shape, latitudinal positions, and intensities were revealed during solar descending phases in this study. The primary goal of this study was to understand more about the electrodynamic processes that cause the EIA crests latitudinal and longitudinal extents over the Brazilian sector.

The EIA showed some distinctive morphologies at the various magnetic meridian sectors investigated in this research, including the accumulation of intense ionization near the magnetic equator (not developed/absent EIA) and two nonidentical crests in both hemispheres. The combination of $\vec{E} \times \vec{B}$ plasma drift and effective meridional wind fields are the primary drivers of EIA, producing these two different features identified based on simulations utilizing the SUPIM-INPE model.

The monthly variations in the EIA over the various magnetic meridian sectors demonstrate a semiannual variation. The December solstice (December, January, and February) and equinox (March, April, September, and October) show major maximums, whereas the June solstice (May, June, July, and August) shows a substantial minimum.

The EIA crests look more symmetric in equinox than in solstice seasons. The asymmetries of the EIA observed during the December solstice are intense than during the June solstice, whereas September equinox is less symmetric than March equinox seasons. This variability is related to the seasonal dependence of the vertical drift (FEJER et al., 1991) and meridional wind. Aside from that, from February to April at most magnetic meridian sectors, the latitudinal distribution of TEC can be seen above the geographic equator. We suggest that the latitudinal distribution is due to the different motions caused by a wind dynamo.

There was a notable contraction of the EIA southern hemispheric crests from the December solstice to June. Meanwhile, the EIA crest positions in the northern hemisphere expand from the December solstice to the June solstice. The intensity of the EIA crests decreased significantly with solar descending phases (i.e., 2014-2019), according to our observations at all sectors.

In addition, spectral analysis of day-to-day crest positions obtained at different magnetic meridians revealed packets of oscillations with periods ranging from 2 to 16 days in this study. Our spectral analysis of the day-to-day latitudinal EIA SH crest positions revealed strong 3-4 day oscillations. The same oscillations were seen in a thermospheric wind and ionospheric parameter ($hmF2$) measured simultaneously by FPI and Digisonde.

The 3-4 day oscillation in the ionospheric parameter and thermospheric wind suggests that the 3-4 day oscillation could modulate electric fields via the E region wind dynamo, altering the vertical height and horizontal distribution of electron densities via upward $\frac{\vec{E} \times \vec{B}}{B^2}$ drift. In the F region, this leads to similar periodic variations in these ionospheric parameters.

In terms of future work on the Equatorial Ionization Anomaly (EIA), it is recommended:

- To examine the effects of annual variations in the EIA overlapping with other modulations, such as lunar tides, as well as a correlation analysis of TEC at the magnetic equator and southern crest with the solar flux index.

- That continuous wind data measurements from the Mesosphere and Lower Thermosphere should be used to study the presence of these 3-4 day oscillations. This will help the space weather community better understand the dynamics of atmospheric propagating waves between the lower atmosphere and the ionosphere and the coupling processes they cause. Furthermore, the SUPIM-INPE model may be used to test how the observed oscillation parameters, such as amplitude, period, and phase, affect EIA development.

REFERENCES

ABDU, M.; BATISTA, I.; WALKER, G.; SOBRAL, J.; TRIVEDI, N.; PAULA, E.
D. Equatorial ionospheric electric fields during magnetospheric disturbances: local
time/longitude dependences from recent eits campaigns. **Journal of
Atmospheric and Terrestrial Physics**, v. 57, n. 10, p. 1065–1083, 1995. 4

ABDU, M.; BRUM, C.; BATISTA, I.; SOBRAL, J.; PAULA, E. D.; SOUZA, J.
Solar flux effects on equatorial ionization anomaly and total electron content over
brazil: observational results versus iri representations. **Advances in Space
Research**, v. 42, n. 4, p. 617–625, 2008. 19, 20, 91, 126

ABDU, M.; MACDOUGALL, J.; BATISTA, I.; SOBRAL, J.; JAYACHANDRAN,
P. Equatorial evening prereversal electric field enhancement and sporadic e layer
disruption: a manifestation of e and f region coupling. **Journal of Geophysical
Research: Space Physics**, v. 108, n. A6, 2003. 17, 123

ABDU, M.; MEDEIROS, R. D.; BITTENCOURT, J.; BATISTA, I. Vertical
ionization drift velocities and range type spread f in the evening equatorial
ionosphere. **Journal of Geophysical Research: Space Physics**, v. 88, n. A1, p.
399–402, 1983. 1

ABDU, M.; RAMKUMAR, T.; BATISTA, I.; BRUM, C.; TAKAHASHI, H.;
REINISCH, B.; SOBRAL, J. Planetary wave signatures in the equatorial
atmosphere–ionosphere system, and mesosphere-e-and f-region coupling. **Journal
of Atmospheric and Solar-Terrestrial Physics**, v. 68, n. 3-5, p. 509–522,
2006. 121

ABDU, M.; SOBRAL, J.; PAULA, E. D.; BATISTA, I. Magnetospheric
disturbance effects on the equatorial ionization anomaly (eia): an overview.
Journal of Atmospheric and Terrestrial Physics, v. 53, n. 8, p. 757–771,
1991. 1, 4, 91

_____. _____. **Journal of Atmospheric and Terrestrial Physics**, v. 53, n. 8,
p. 757–771, 1991. 19, 20

ABDULLAH, M.; STRANGEWAYS, H. J.; WALSH, D. M. Improving ambiguity
resolution rate with an accurate ionospheric differential correction. **The Journal
of Navigation**, v. 62, n. 1, p. 151–166, 2009. 37

AERONAUTICS, N.; (NASA)., S. A. **International Geomagnetic Reference Field**. 2019. Disponível em: <https://ngdc.noaa.gov/IAGA/vmod/igrf.html>. 45

_____. **OMNIWeb data explorer**. 2021. Disponível em: <https://omniweb.gsfc.nasa.gov/form/dx1.html>. 125

AFRAIMOVICH, E.; PEREVALOVA, N. Gps monitoring of the earths upper atmosphere. **Irkutsk: SC RRS SB RAMS**, v. 480, 2006. 38

AKALA, A.; DOHERTY, P.; CARRANO, C.; VALLADARES, C.; GROVES, K. Impacts of ionospheric scintillations on gps receivers intended for equatorial aviation applications. **Radio Science**, v. 47, n. 04, p. 1–11, 2012. 3

AMAECHI, P.; OYEYEMI, E.; AKALA, A. Variability of the african equatorial ionization anomaly (eia) crests during the year 2013. **Canadian Journal of Physics**, v. 97, n. 2, p. 155–165, 2019. 23, 25, 26

ANDERSON, D. A theoretical study of the ionospheric f region equatorial anomalyi. theory. **Planetary and Space Science**, v. 21, n. 3, p. 409–419, 1973. 1

ANDERSON, D.; ANGHEL, A.; YUMOTO, K.; ISHITSUKA, M.; KUDEKI, E. Estimating daytime vertical exb drift velocities in the equatorial f-region using ground-based magnetometer observations. **Geophysical Research Letters**, v. 29, n. 12, p. 37–1, 2002. 1, 19, 20

APPLETON, E. V. Two anomalies in the ionosphere. **Nature**, v. 157, n. 3995, p. 691, 1946. 1, 18

ARRIAGADA, M. A.; FOPPIANO, A. J.; BUONSANTO, M. J. Solar activity variations of meridional winds over king george island, antarctica. **Journal of Atmospheric and Solar-Terrestrial Physics**, v. 59, n. 12, p. 1405–1410, 1997. 107, 116

BAGIYA, M. S.; JOSHI, H.; IYER, K.; AGGARWAL, M.; RAVINDRAN, S.; PATHAN, B. Tec variations during low solar activity period (2005–2007) near the equatorial ionospheric anomaly crest region in india. **Annales Geophysicae**, v. 27, n. 3, p. 1047–1057, 2009. 2

BAILEY, G.; BALAN, N. Some modelling studies of the equatorial ionosphere using the sheffield university plasmasphere ionosphere model. **Advances in Space Research**, v. 18, n. 6, p. 59–68, 1996. 10, 68, 72

BAILEY, G.; BALAN, N.; SU, Y. The sheffield university plasmasphere ionosphere modela review. **Journal of Atmospheric and Solar-Terrestrial Physics**, v. 59, n. 13, p. 1541–1552, 1997. 1, 68

BAILEY, G.; SELLEK, R. A mathematical model of the earth's plasmasphere and its application in a study of he+ at l= 3. **Annales Geophysicae**, v. 8, p. 171–189, 1990. 72

BAKER, W.; MARTYN, D. Conductivity of the ionosphere. **Nature**, v. 170, n. 4339, p. 1090–1092, 1952. 13

BALAN, N.; BAILEY, G. Equatorial plasma fountain and its effects: possibility of an additional layer. **Journal of Geophysical Research: Space Physics**, v. 100, n. A11, p. 21421–21432, 1995. 18, 20

BALAN, N.; BAILEY, G.; ABDU, M.; OYAMA, K.; RICHARDS, P.; MACDOUGALL, J.; BATISTA, I. Equatorial plasma fountain and its effects over three locations: evidence for an additional layer, the f 3 layer. **Journal of Geophysical Research: Space Physics**, v. 102, n. A2, p. 2047–2056, 1997. 8, 19

BALAN, N.; BAILEY, G.; SUBBARAO, K.; ABDU, M.; RAO, P. Model comparisons of equatorial plasma fountain and equatorial anomaly at three locations. **Advances in Space Research**, v. 18, n. 6, p. 69–78, 1996. 1

BALAN, N.; BATISTA, I.; ABDU, M.; MACDOUGALL, J.; BAILEY, G. Physical mechanism and statistics of occurrence of an additional layer in the equatorial ionosphere. **Journal of Geophysical Research: Space Physics**, v. 103, n. A12, p. 29169–29181, 1998. 128, 129

BALAN, N.; SOUZA, J.; BAILEY, G. Recent developments in the understanding of equatorial ionization anomaly: a review. **Journal of Atmospheric and Solar-Terrestrial Physics**, v. 171, p. 3–11, 2018. 1, 4, 91

BARON, M.; HEINSELMAN, C.; PETRIČEKS, J. Solar cycle and seasonal variations of the ionosphere observed with the chatanika incoherent scatter radar. **Radio Science**, v. 18, n. 6, p. 895–900, 1983. 126

BASU, S.; GROVES, K.; BASU, S.; SULTAN, P. Specification and forecasting of scintillations in communication/navigation links: current status and future plans. **Journal of Atmospheric and Solar-Terrestrial Physics**, v. 64, n. 16, p. 1745–1754, 2002. 19

BATISTA, I.; ABDU, M.; BITTENCOURT, J. Equatorial f region vertical plasma drifts: seasonal and longitudinal asymmetries in the american sector. **Journal of Geophysical Research: Space Physics**, v. 91, n. A11, p. 12055–12064, 1986. 15, 16, 17, 19, 20, 91

BATISTA, I. S.; ABDU, M. Ionospheric variability at brazilian low and equatorial latitudes: comparison between observations and iri model. **Advances in Space Research**, v. 34, n. 9, p. 1894–1900, 2004. 1, 19, 20

BATISTA, I. S.; CANDIDO, C.; SOUZA, J.; ABDU, M.; ARAUJO, R. de; RESENDE, L.; SANTOS, A. F3 layer development during quiet and disturbed periods as observed at conjugate locations in brazil: the role of the meridional wind. **Journal of Geophysical Research: Space Physics**, v. 122, n. 2, p. 2361–2373, 2017. 128, 129

BATISTA, I. S.; DIOGO, E. M.; SOUZA, J. R.; ABDU MANGALATHAYIL ALI, P. D.; BAILEY, G. J. Equatorial ionization anomaly: the role of thermospheric winds and the effects of the geomagnetic field secular variation. In: **Aeronomy of the Earth's atmosphere and ionosphere**. [S.l.: s.n.], 2011. p. 317–328. 95, 97

BOLAJI, O.; OWOLABI, O.; FALAYI, E.; JIMOH, E.; KOTOYE, A.; ODEYEMI, O.; RABIU, B.; DOHERTY, P.; YIZENGAW, E.; YAMAZAKI, Y. Observations of equatorial ionization anomaly over africa and middle east during a year of deep minimum. **Annales Geophysicae**, v. 35, n. 1, p. 123–132, 2017. 1, 2, 23

BOLAJI, O.; OYEYEMI, E.; OWOLABI, O.; YAMAZAKI, Y.; RABIU, A.; OKOH, D.; FUJIMOTO, A.; AMORY-MAZAUDIER, C.; SEEMALA, G.; YOSHIKAWA, A. Solar quiet current response in the african sector due to a 2009 sudden stratospheric warming event. **Journal of Geophysical Research: Space Physics**, v. 121, n. 8, p. 8055–8065, 2016. 19, 20

CHEN, C.-H.; LIU, J.-Y.; YUMOTO, K.; LIN, C.-H.; FANG, T.-W. Equatorial ionization anomaly of the total electron content and equatorial electrojet of ground-based geomagnetic field strength. **Journal of Atmospheric and Solar-Terrestrial Physics**, v. 70, n. 17, p. 2172–2183, 2008. 1, 4, 19, 20

CHEN, P.-R. Two-day oscillation of the equatorial ionization anomaly. **Journal of Geophysical Research: Space Physics**, v. 97, n. A5, p. 6343–6357, 1992. 1, 117

DASGUPTA, A.; PAUL, A.; DAS, A. Ionospheric total electron content (tec) studies with gps in the equatorial region. **Indian Journal of Radio and Space Physics**, v. 36, n. n4, p. 278–292, 2007. 4

DEAR, R. M.; MITCHELL, C. N. Gps interfrequency biases and total electron content errors in ionospheric imaging over europe. **Radio Science**, v. 41, n. 06, p. 1–7, 2006. 40

DIAS, M.; FAGUNDES, P.; VENKATESH, K.; PILLAT, V.; RIBEIRO, B.; SEEMALA, G.; ARCANJO, M. Daily and monthly variations of the equatorial ionization anomaly (eia) over the brazilian sector during the descending phase of the solar cycle 24. **Journal of Geophysical Research: Space Physics**, 2020. 3, 22, 91, 106, 107, 108, 109, 111

DUNCAN, R. The equatorial f-region of the ionosphere. **Journal of Atmospheric and Terrestrial Physics**, v. 18, n. 2-3, p. 89–100, 1960. 1

DURMAZ, M.; KARSLIOGLU, M. O. Regional vertical total electron content (vtec) modeling together with satellite and receiver differential code biases (dcbs) using semi-parametric multivariate adaptive regression b-splines (sp-bmars). **Journal of Geodesy**, v. 89, n. 4, p. 347–360, 2015. 37

EASTES, R.; SOLOMON, S.; DANIELL, R.; ANDERSON, D.; BURNS, A.; ENGLAND, S.; MARTINIS, C.; MCCLINTOCK, W. Global-scale observations of the equatorial ionization anomaly. **Geophysical Research Letters**, v. 46, n. 16, p. 9318–9326, 2019. 4

EGITO, F.; BURITI, R. A.; MEDEIROS, A. F. de; TAKAHASHI, H. The 3-4 day ultra-fast kelvin wave (ufkw) induced airglow and mlt wind variability and its possible interaction with diurnal tide over the brazilian equatorial region. In: BRAZILIAN GEOPHYSICAL SOCIETY. **INTERNATIONAL CONGRESS OF THE BRAZILIAN GEOPHYSICAL SOCIETY, 15., 2017, Rio de Janeiro**. [S.l.], 2017. p. 1679–1684. 122

ENGLAND, S.; MAUS, S.; IMMEL, T.; MENDE, S. Longitudinal variation of the e-region electric fields caused by atmospheric tides. **Geophysical Research Letters**, v. 33, n. 21, 2006. 18

ENGLERT, C.; HARLANDER, J.; BROWN, C.; MERIWETHER, J.; MAKELA, J.; CASTELAZ, M.; EMMERT, J.; DROB, D.; MARR, K. Coincident thermospheric wind measurements using ground-based doppler asymmetric spatial heterodyne (dash) and fabry–perot interferometer (fpi) instruments. **Journal of Atmospheric and Solar-Terrestrial Physics**, v. 86, p. 92–98, 2012. 119

ESTUDO E MONITORAMENTO BRASILEIRO DO CLIMA ESPACIAL (EMBRACE). 2017. Disponível em: <http://www2.inpe.br/climaespacial/portal/en/.>. 41

FAGUNDES, P.; PILLAT, V.; BOLZAN, M.; SAHAI, Y.; BECKER-GUEDES, F.; ABALDE, J.; ARANHA, S.; BITTENCOURT, J. Observations of f layer electron density profiles modulated by planetary wave type oscillations in the equatorial ionospheric anomaly region. **Journal of Geophysical Research: Space Physics**, v. 110, n. A12, 2005. 1, 4, 19, 20, 91, 116, 117

FARLEY, D.; BONELLI, E.; FEJER, B. G.; LARSEN, M. The prereversal enhancement of the zonal electric field in the equatorial ionosphere. **Journal of Geophysical Research: Space Physics**, v. 91, n. A12, p. 13723–13728, 1986. 17

FEJER, B. G.; PAULA, E. D.; GONZALEZ, S.; WOODMAN, R. Average vertical and zonal f region plasma drifts over jicamarca. **Journal of Geophysical Research: Space Physics**, v. 96, n. A8, p. 13901–13906, 1991. 16, 17, 18, 19, 20, 116, 133

FENNELLY, J.; TORR, D.; RICHARDS, P. Euvac: a solar euv flux model for aeronomic calculations. **Journal of Geophysical Research**, v. 99, n. A5, p. 8981–8992, 1994. 73

FIGUEIREDO, C. A. O.; BURITI, R. A.; PAULINO, I.; MERIWETHER, J. W.; MAKELA, J. J.; BATISTA, I. S.; BARROS, D.; MEDEIROS, A. F. Effects of the midnight temperature maximum observed in the thermosphere–ionosphere over the northeast of brazil. In: **Annales Geophysicae**. [S.l.: s.n.], 2017. v. 35, n. 4, p. 953–963. 119

FISHER, D. **Three-dimensional wind measurements and modeling using a bi-static fabry-perot interferometer system in Brazil**. Thesis (Master of Science in Electrical and Computer Engineering) — University of Illinois, United States, 2013. 119

FORBES, J. M. The equatorial electrojet. **Reviews of Geophysics**, v. 19, n. 3, p. 469–504, 1981. 15

_____. Planetary waves in the thermosphere-ionosphere system. **Journal of Geomagnetism and Geoelectricity**, v. 48, n. 1, p. 91–98, 1996. 117

_____. Wave coupling between the lower and upper atmosphere: case study of an ultra-fast kelvin wave. **Journal of Atmospheric and Solar-Terrestrial Physics**, v. 62, n. 17-18, p. 1603–1621, 2000. 117, 122, 126

FORBES, J. M.; LEVERONI, S. Quasi 16-day oscillation in the ionosphere. **Geophysical Research Letters**, v. 19, n. 10, p. 981–984, 1992. 4

FORBES, J. M.; ZHANG, X.; PALO, S. E.; RUSSELL, J.; MERTENS, C. J.; MLYNCZAK, M. Kelvin waves in stratosphere, mesosphere and lower thermosphere temperatures as observed by timed/saber during 2002–2006. **Earth, Planets and Space**, v. 61, n. 4, p. 447–453, 2009. 122

FRICK, P.; GALYAGIN, D.; HOYT, D. V.; NESME-RIBES, E.; SCHATTEN, K. H.; SOKOLOFF, D.; ZAKHAROV, V. Wavelet analysis of solar activity recorded by sunspot groups. **Astronomy and Astrophysics**, v. 328, p. 670–681, 1997. 59

GAN, Q.; WANG, W.; YUE, J.; LIU, H.; CHANG, L. C.; ZHANG, S.; BURNS, A.; DU, J. Numerical simulation of the 6 day wave effects on the ionosphere: dynamo modulation. **Journal of Geophysical Research: Space Physics**, v. 121, n. 10, p. 10–103, 2016. 4, 117

GAO, Y. Ionosphere modelling using carrier smoothed ionosphere observations from a regional gps network. **Geomatica**, v. 56, n. 2, p. 97–106, 2002. 38

GERRARD, A.; MERIWETHER, J. Initial daytime and nighttime sofdi observations of thermospheric winds from fabry-perot doppler shift measurements of the 630-nm oi line-shape profile. **Annales Geophysicae**, v. 29, n. 9, p. 1529–1536, 2011. 113

GOLTON, E.; WALKER, G. Observations of ionospheric electron content across the equatorial anomaly at sunspot minimum. **Journal of Atmospheric and Terrestrial Physics**, v. 33, n. 1, p. 1–11, 1971. 2, 27

GONCHARENKO, L.; CHAU, J.; CONDOR, P.; COSTER, A.; BENKEVITCH, L. Ionospheric effects of sudden stratospheric warming during moderate-to-high solar activity: case study of january 2013. **Geophysical Research Letters**, v. 40, n. 19, p. 4982–4986, 2013. 1, 117

GOODMAN, J. M. Ionosphere characteristics. In: . [S.l.: s.n.], 2001. 8

GU, S.-Y.; LIU, H.-L.; LI, T.; DOU, X.; WU, Q.; III, J. M. R. Observation of the neutral-ion coupling through 6 day planetary wave. **Journal of Geophysical Research: Space Physics**, v. 119, n. 12, p. 10–376, 2014. 117

GU, S.-Y.; RUAN, H.; YANG, C.-Y.; GAN, Q.; DOU, X.; WANG, N. The morphology of the 6-day wave in both the neutral atmosphere and f region ionosphere under solar minimum conditions. **Journal of Geophysical Research: Space Physics**, v. 123, n. 5, p. 4232–4240, 2018. 4, 117

HALDOUPIS, C. A tutorial review on sporadic e layers. **Aeronomy of the Earth's Atmosphere and Ionosphere**, p. 381–394, 2011. 9

HANSON, W.; MOFFETT, R. Ionization transport effects in the equatorial f region. **Journal of Geophysical Research**, v. 71, n. 23, p. 5559–5572, 1966. 1, 18, 19

HARGREAVES, J. K. **The solar-terrestrial environment: an introduction to geospace-the science of the terrestrial upper atmosphere, ionosphere, and magnetosphere**. [S.l.]: Cambridge University Press, 1992. 9, 11

HEDIN, A. E.; FLEMING, E.; MANSON, A.; SCHMIDLIN, F.; AVERY, S.; CLARK, R.; FRANKE, S.; FRASER, G.; TSUDA, T.; VIAL, F. et al. Empirical wind model for the upper, middle and lower atmosphere. **Journal of Atmospheric and Terrestrial Physics**, v. 58, n. 13, p. 1421–1447, 1996. xi, xiii, xviii, 73, 93

HEELIS, R. Electrodynamics in the low and middle latitude ionosphere: a tutorial. **Journal of Atmospheric and Solar-Terrestrial Physics**, v. 66, n. 10, p. 825–838, 2004. 4, 14, 17, 18

HEELIS, R.; HANSON, W. Interhemispheric transport induced by neutral zonal winds in the f region. **Journal of Geophysical Research: Space Physics**, v. 85, n. A6, p. 3045–3047, 1980. 18, 20

HIROTA, I. Kelvin waves in the equatorial middle atmosphere observed by the nimbus 5. scr. **Journal of Atmospheric Sciences**, v. 36, n. 2, p. 217–222, 1979. 122

HOFMANN-WELLENHOF, B.; LICHTENEGGER, H.; COLLINS, J. **Global positioning system: theory and practice**. [S.l.]: Springer Science & Business Media, 2012. 36, 40

_____. _____. [S.l.]: Springer Science & Business Media, 2012. 37

HORNE, J. H.; BALIUNAS, S. L. A prescription for period analysis of unevenly sampled time series. **The Astrophysical Journal**, v. 302, p. 757–763, 1986. 56, 57

HUY, M. L.; AMORY-MAZAUDIER, C.; FLEURY, R.; BOURDILLON, A.; LASSUDRIE-DUCHESNE, P.; THI, L. T.; CHIEN, T. N.; HA, T. N.; VILA, P. Time variations of the total electron content in the southeast asian equatorial ionization anomaly for the period 2006–2011. **Advances in Space Research**, v. 54, n. 3, p. 355–368, 2014. 27, 29, 30

JAKOWSKI, N. Tec monitoring by using satellite positioning systems. **Modern Ionospheric Science**, p. 371–390, 1996. 40

JAYACHANDRAN, P.; RAM, P. S.; SOMAYAJULU, V.; RAO, P. R. Effect of equatorial ionization anomaly on the occurrence of spread-f. **Annales Geophysicae**, v. 115, n. 2, p. 255–262, 1997. 1

JICAMARCA RADIO OBSERVATORY. Madrigal. 2021. Disponível em: <https://hesperia.gsfc.nasa.gov/ssw/gen/idl/image/centroid.pro.>. 95

JONAH, O.; PAULA, E. de; MUELLA, M.; DUTRA, S.; KHERANI, E.; NEGRETI, P.; OTSUKA, Y. Tec variation during high and low solar activities over south american sector. **Journal of Atmospheric and Solar-Terrestrial Physics**, v. 135, p. 22–35, 2015. 4

JOSEPH, O. O.; YAMAZAK, Y.; CILLIERS, P.; BAKI, P.; NGWIRA, C. M.; MITO, C. A study on the response of the equatorial ionization anomaly over the east africa sector during the geomagnetic storm of november 13, 2012. **Advances in Space Research**, v. 55, n. 12, p. 2863–2872, 2015. 3

KARPACHEV, A.; GASILOV, N. Zonal and meridional wind components derived from intercosmos-19 hmf2 measurements. **Advances in Space Research**, v. 27, n. 6-7, p. 1245–1252, 2001. 107, 116

KELLEY, M. **The Earth's ionosphere: plasma physics and electrodynamics**. [S.l.: s.n.], 2012. 1, 4, 7, 13, 14

KENDALL, P. Geomagnetic control of diffusion in the f2-region of the ionospherei the form of the diffusion operator. **Journal of Atmospheric and Terrestrial Physics**, v. 24, n. 9, p. 805–811, 1962. 72

KHADKA, S. M.; VALLADARES, C. E.; SHEEHAN, R.; GERRARD, A. J. Effects of electric field and neutral wind on the asymmetry of equatorial ionization anomaly. **Radio Science**, v. 53, n. 5, p. 683–697, 2018. 19, 20, 21, 91, 111, 112, 114, 115, 116

KIKUCHI, T.; LÜHR, H.; SCHLEGEL, K.; TACHIHARA, H.; SHINOHARA, M.; KITAMURA, T.-I. Penetration of auroral electric fields to the equator during a substorm. **Journal of Geophysical Research: Space Physics**, v. 105, n. A10, p. 23251–23261, 2000. 1, 91

KOPP, E. On the abundance of metal ions in the lower ionosphere. **Journal of Geophysical Research: Space Physics**, v. 102, n. A5, p. 9667–9674, 1997. 9

KUMAR, S.; SINGH, A. Variation of ionospheric total electron content in indian low latitude region of the equatorial anomaly during may 2007–april 2008. **Advances in Space Research**, v. 43, n. 10, p. 1555–1562, 2009. 2

KUTIEV, I.; OTSUKA, Y.; PANCHEVA, D.; HEELIS, R. Response of low-latitude ionosphere to medium-term changes of solar and geomagnetic activity. **Journal of Geophysical Research: Space Physics**, v. 117, n. A8, 2012. 126

KWAK, Y.-S.; KIL, H.; LEE, W. K.; YANG, T.-Y. Variation of the hemispheric asymmetry of the equatorial ionization anomaly with solar cycle. **Journal of Astronomy and Space Sciences**, v. 36, n. 3, p. 159–168, 2019. 111, 128

LEICK, A.; RAPOPORT, L.; TATARNIKOV, D. **GPS satellite surveying**. [S.l.]: John Wiley & Sons, 2015. 38

LI, K.-F.; LIN, L.-C.; BUI, X.-H.; LIANG, M.-C. The 11 year solar cycle response of the equatorial ionization anomaly observed by gps radio occultation. **Journal of Geophysical Research: Space Physics**, v. 123, n. 1, p. 848–861, 2018. 123

_____. _____. **Journal of Geophysical Research: Space Physics**, v. 123, n. 1, p. 848–861, 2018. 126

LIU, H.-L. Variability and predictability of the space environment as related to lower atmosphere forcing. **Space Weather**, v. 14, n. 9, p. 634–658, 2016. 117

LOMB, N. R. Least-squares frequency analysis of unequally spaced data. **Astrophysics and Space Science**, v. 39, n. 2, p. 447–462, 1976. 56, 57

LOMOTEY, S. O. **Observações de osilações em escala planetária na baixa termosfera equatorial.**. 29 p. Mestrado em Física — Universidade Federal de Campina Grande (UFCG), Campina Grande, 2016. 119

LÓPEZ-GONZÁLEZ, M.; RODRÍGUEZ, E.; GARCÍA-COMAS, M.; COSTA, V.; SHEPHERD, M.; SHEPHERD, G.; AUSHEV, V.; SARGOYTCHEV, S. Climatology of planetary wave type oscillations with periods of 2-20 days derived from o2 atmospheric and oh (6-2) airglow observations at mid-latitude with sati. In: **Annales Geophysicae: Atmospheres, Hydrospheres and Space Sciences**. [S.l.: s.n.], 2009. v. 27, n. 9, p. 3645. 86

MAEDA, K.; KATO, S. Electrodynamics of the ionosphere. **Space Science Reviews**, v. 5, n. 1, p. 57–79, 1966. 12

MAKELA, J. J.; MERIWETHER, J. W.; RIDLEY, A. J.; CIOCCA, M.; CASTELLEZ, M. W. Large-scale measurements of thermospheric dynamics with a multisite fabry-perot interferometer network: overview of plans and results from midlatitude measurements. **International Journal of Geophysics**, v. 2012, 2012. 119

MANNUCCI, A.; WILSON, B.; YUAN, D.; HO, C.; LINDQWISTER, U.; RUNGE, T. A global mapping technique for gps-derived ionospheric total electron content measurements. **Radio Science**, v. 33, n. 3, p. 565–582, 1998. 40

MARTYN, D. F. Atmospheric tides in the ionosphere-i. solar tides in the f2 region. **Proceedings of the Royal Society of London A**, v. 189, n. 1017, p. 241–260, 1947. 1, 18

MARUYAMA, T.; SAITO, S.; KAWAMURA, M.; NOZAKI, K. Thermospheric meridional winds as deduced from ionosonde chain at low and equatorial latitudes and their connection with midnight temperature maximum. **Journal of Geophysical Research: Space Physics**, v. 113, n. A9, 2008. 107, 116

MATSUOKA, M. T.; CAMARGO, P. de O. Correção ionosférica utilizando os mapas globais do tec do igs: avaliação no posicionamento por ponto na região brasileira. **Boletim de Ciências Geodésicas**, v. 13, n. 2, 2007. 38

MERIWETHER, J.; FAIVRE, M.; FESEN, C.; SHERWOOD, P.; VELIZ, O. New results on equatorial thermospheric winds and the midnight temperature maximum. **Annales Geophysicae**, v. 26, n. 3, p. 447–466, 2008. 119

MITRA, A. A review of d-region processes in non-polar latitudes. **Journal of Atmospheric and Terrestrial Physics**, v. 30, n. 6, p. 1065–1114, 1968. 73

MITRA, S. Geomagnetic control of region f 2 of the ionosphere. **Nature**, v. 158, n. 4019, p. 668–669, 1946. 19

MO, X.; ZHANG, D. Quasi-10 d wave modulation of an equatorial ionization anomaly during the southern hemisphere stratospheric warming of 2002. **Annales Geophysicae**, v. 38, n. 1, p. 9–16, 2020. 2, 4, 117

_____. Six-day periodic variation in equatorial ionization anomaly region. **Journal of Geophysical Research: Space Physics**, v. 125, n. 11, p. e2020JA028225, 2020. 123

MO, X.; ZHANG, D.; LIU, J.; HAO, Y.; YE, J.; QIN, J.; WEI, W.; XIAO, Z. Morphological characteristics of equatorial ionization anomaly crest over nanning region. **Radio Science**, v. 53, n. 1, p. 37–47, 2018. 27, 31, 32, 116, 117

MONICO, J. F. G. **Posicionamento pelo GNSS: descrição, fundamentos e aplicações**. [S.l.]: Editora Unesp, 2007. 36

MRIDULA, N.; PANT, T. K.; MANJU, G. On the variability of the equatorial ionization anomaly trough over indian region: a novel analysis using beacon tec measurements. **Advances in Space Research**, v. 66, n. 3, p. 646–654, 2020. 97

MUKESH, R.; KARTHIKEYAN, V.; SOMA, P.; SINDHU, P. Ordinary kriging-and cokriging-based surrogate model for ionospheric tec prediction using navic/gps data. **Acta Geophysica**, v. 68, n. 5, p. 1529–1547, 2020. 38

MUNGUFENI, P.; HABARULEMA, J. B.; MIGOYA-ORUÉ, Y.; JURUA, E. Statistical analysis of the correlation between the equatorial electrojet and the occurrence of the equatorial ionisation anomaly over the east african sector. **Annales Geophysicae**, v. 36, n. 3, p. 841–853, 2018. 1, 23, 24, 25

NAMGALADZE, A.; KORENKOV, Y. N.; KLIMENKO, V.; KARPOV, I.; SUROTKIN, V.; NAUMOVA, N. Numerical modelling of the thermosphere-ionosphere-protonosphere system. **Journal of Atmospheric and Terrestrial Physics**, v. 53, n. 11-12, p. 1113–1124, 1991. 1

NATIONAL AERONAUTICS AND SPACE ADMINISTRATION (NASA). Function centroid. 2019. Disponível em: <https://hesperia.gsfc.nasa.gov/ssw/gen/idl/image/centroid.pro>. 51

NOGUEIRA, P.; ABDU, M.; BATISTA, I.; SIQUEIRA, P. D. Equatorial ionization anomaly and thermospheric meridional winds during two major storms over brazilian low latitudes. **Journal of Atmospheric and Solar-Terrestrial Physics**, v. 73, n. 11-12, p. 1535–1543, 2011. 3, 19, 20, 21

NOGUEIRA, P.; ABDU, M.; SOUZA, J.; BATISTA, I.; BAILEY, G.; SANTOS, A.; TAKAHASHI, H. Equatorial ionization anomaly development as studied by gps tec and fof2 over brazil: A comparison of observations with model results from supim and iri-2012. **Journal of Atmospheric and Solar-Terrestrial Physics**, v. 104, p. 45–54, 2013. 1, 19, 20, 95

OGAJA, C. A. **Applied GPS for engineers and project managers. [S.l.]: ASCE Press,**. [S.l.: s.n.], 2011. 36

OLUWADARE, T. S.; THAI, C. N.; AKALA, A. O.-O.; HEISE, S.; ALIZADEH, M.; SCHUH, H. Characterization of gps-tec over african equatorial ionization anomaly (eia) region during 2009–2016. **Advances in Space Research**, v. 63, n. 1, p. 282–301, 2019. 3

OTSUKA, Y.; OGAWA, T.; SAITO, A.; TSUGAWA, T.; FUKAO, S.; MIYAZAKI, S. A new technique for mapping of total electron content using gps network in japan. **Earth, Planets and Space**, v. 54, n. 1, p. 63–70, 2002. 40, 41

OTSUKA, Y.; SUZUKI, K.; NAKAGAWA, S.; NISHIOKA, M.; SHIOKAWA, K.; TSUGAWA, a. Gps observations of medium-scale traveling ionospheric disturbances over europe. **Annales Geophysicae**, v. 31, n. 2, p. 163–172, 2013. 43

PAES, R.; BATISTA, I.; CANDIDO, C.; JONAH, O.; SANTOS, P. Equatorial ionization anomaly variability over the brazilian region during boreal sudden stratospheric warming events. **Journal of Geophysical Research: Space Physics**, v. 119, n. 9, p. 7649–7664, 2014. 19, 20

PANCHEVA, D.; MITCHELL, N.; YOUNGER, P. Meteor radar observations of atmospheric waves in the equatorial mesosphere/lower thermosphere over ascension island. **Annales Geophysicae**, v. 24, n. 2, p. 387–404, 2004. 122

PANCHEVA, D.; MUKHTAROV, P.; ANDONOV, B.; FORBES, J. Global distribution and climatological features of the 5–6-day planetary waves seen in the saber/timed temperatures (2002–2007). **Journal of Atmospheric and Solar-Terrestrial Physics**, v. 72, n. 1, p. 26–37, 2010. 117

PEDATELLA, N.; LIU, H.-L.; HAGAN, M. Day-to-day migrating and nonmigrating tidal variability due to the six-day planetary wave. **Journal of Geophysical Research: Space Physics**, v. 117, n. A6, 2012. 117

PEREIRA, V. A. S.; CAMARGO, P. de O. Brazilian active gnss networks as systems for monitoring the ionosphere. **GPS Solutions**, v. 21, n. 3, p. 1013–1025, 2017. 36, 38

PERRIER, V.; PHILIPOVITCH, T.; BASDEVANT, C. Wavelet spectra compared to fourier spectra. **Journal of Mathematical Physics**, v. 36, n. 3, p. 1506–1519, 1995. 61

PICONE, J.; HEDIN, A.; DROB, D. P.; AIKIN, A. Nrlmsise-00 empirical model of the atmosphere: Statistical comparisons and scientific issues. **Journal of Geophysical Research: Space Physics**, v. 107, n. A12, p. SIA–15, 2002. 73

QIAN, L.; BURNS, A. G.; SOLOMON, S. C.; WANG, W. Annual/semiannual variation of the ionosphere. **Geophysical Research Letters**, v. 40, n. 10, p. 1928–1933, 2013. 131

QUEGAN, S.; BAILEY, G.; MOFFETT, R. Diffusion coefficients for three major ions in the topside ionosphere. **Planetary and Space Science**, v. 29, n. 8, p. 851–867, 1981. 70

RAGHAVARAO, R.; NAGESWARARAO, M.; SASTRI, J. H.; VYAS, G.; SRIRAMARAO, M. Role of equatorial ionization anomaly in the initiation of equatorial spread f. **Journal of Geophysical Research: Space Physics**, v. 93, n. A6, p. 5959–5964, 1988. 92, 97

RAM, S. T.; SU, S.-Y.; LIU, C. Formosat-3/cosmic observations of seasonal and longitudinal variations of equatorial ionization anomaly and its interhemispheric asymmetry during the solar minimum period. **Journal of Geophysical Research: Space Physics**, v. 114, n. A6, 2009. 27, 28, 91

RAO, S.; CHAKRABORTY, M.; PANDEY, R. Ionospheric variations over chinese eia region using fof2 and comparison with iri-2016 model. **Advances in Space Research**, v. 62, n. 1, p. 84–93, 2018. 126

RATCLIFFE, J. A. et al. **An introduction to ionosphere and magnetosphere**. [S.l.: s.n.], 1972. 7

RAY, S.; PAUL, A.; DASGUPTA, A. Equatorial scintillations in relation to the development of ionization anomaly. 2006. Disponível em: <https://hal.archives-ouvertes.fr/hal-00318073/document>. 1

RISHBETH, H. Polarization fields produced by winds in the equatorial f-region. **Planetary and Space Science**, v. 19, n. 3, p. 357–369, 1971. 16, 17, 18, 123

_____. The ionospheric e-layer and f-layer dynamosa tutorial review. **Journal of Atmospheric and Solar-Terrestrial Physics**, v. 59, n. 15, p. 1873–1880, 1997. 11

RISHBETH, H.; GARRIOTT, O. K. **Introduction to ionospheric physics**. [S.l.: s.n.], 1969. 11, 13, 14

ROMERO-HERNANDEZ, E.; DENARDINI, C.; TAKAHASHI, H.; GONZALEZ-ESPARZA, J.; NOGUEIRA, P.; PADUA, M. de; LOTTE, R.; NEGRETI, P.; JONAH, O.; RESENDE, L. Daytime ionospheric tec weather study over latin america. **Journal of Geophysical Research: Space Physics**, v. 123, n. 12, p. 10–345, 2018. 22, 23, 107

SABZEHEE, F.; FARZANEH, S.; SHARIFI, M. A.; AKHOONDZADEH, M. Tec regional modeling and prediction using ann method and single frequency receiver over iran. **Annals of Geophysics**, v. 61, n. 1, p. 103, 2018. 36, 38

SAGAWA, E.; IMMEL, T.; FREY, H.; MENDE, S. Longitudinal structure of the equatorial anomaly in the nighttime ionosphere observed by image/fuv. **Journal of Geophysical Research: Space Physics**, y, v. 110, n. A11, 2005. 2, 3

SANTOS, P. M. T. **Estudo da dinâmica do sistema ionosfera-termosfera por modelo teórico e observações experimentais**. 134 p. Tese (Doutorado em Geofísica Espacial) — Instituto Nacional de Pesquisas Espaciais (INPE), São José dos Campos, 2005. 68

SARDÓN, E.; ZARRAOA, N. Estimation of total electron content using gps data: how stable are the differential satellite and receiver instrumental biases? **Radio Science**, v. 32, n. 5, p. 1899–1910, 1997. 40

SCARGLE, J. D. Studies in astronomical time series analysis. ii-statistical aspects of spectral analysis of unevenly spaced data. **The Astrophysical Journal**, v. 263, p. 835–853, 1982. 56

SCHAER, S.; NATURELLES., S. helvétique des sciences. **Mapping and predicting the Earth's ionosphere using the Global Positioning System**. [S.l.]: Institut für Geodäsie und Photogrammetrie, Eidg. Technische Hochschule , 1999. 37

SCHERLIESS, L.; FEJER, B. G. Radar and satellite global equatorial f region vertical drift model. **Journal of Geophysical Research: Space Physics**, v. 104, n. A4, p. 6829–6842, 1999. xi, xiii, xviii, 73, 93, 94, 95, 96, 97, 99, 100, 101

SCHUNK, R.; NAGY, A. **Ionospheres: physics, plasma physics, and chemistry**. [S.l.]: Cambridge University Press, 2009. 9, 45

SCHUNK, R.; SCHERLIESS, L.; SOJKA, J. J.; THOMPSON, D. C.; ZHU, L. Ionospheric weather forecasting on the horizon. **Space Weather**, v. 3, n. 8, 2005. 1

SEEBER, G. **Satellite geodesy: foundations, methods, and applications**. [S.l.]: Walter de Gruyter, 2008. 37, 38

SEPULVEDA, M. A. B. **Efeitos do campo elétrico e do vento neutro sobre a ionosfera equatorial e de baixas latitudes durante períodos geomagneticamente calmos e perturbados.** 186 p. (INPE-11.12.14.13-TDI). Tese (Doutorado em Geofísica Espacial) — Instituto Nacional de Pesquisas Espaciais (INPE), São José dos Campos, 2015. 10

SHARIFI, M. A.; FARZANEH, S. The ionosphere electron density spatio-temporal modeling based on the slepian basis functions. **Acta Geodaetica et Geophysica**, v. 52, n. 1, p. 5–18, 2017. 38, 39

SOLOVIEV, A.; CHULLIAT, A.; BOGOUTDINOV, S.; GVISHIANI, A.; AGAYAN, S.; PELTIER, A.; HEUMEZ, B. Automated recognition of spikes in 1 hz data recorded at the easter island magnetic observatory. **Earth, Planets and Space**, v. 64, n. 9, p. 743–752, 2012. 44

SOUZA, J.; ABDU, M.; BATISTA, I. An empirical model for the ionospheric electron content at low latitude in brazil and a comparison with iri95. **Advances in Space Research**, v. 31, n. 3, p. 629–634, 2003. 1, 19, 20

SOUZA, J. d.; ABDU, M.; BATISTA, I.; BAILEY, G. Determination of vertical plasma drift and meridional wind using the sheffield university plasmasphere ionosphere model and ionospheric data at equatorial and low latitudes in brazil:

Summer solar minimum and maximum conditions. **Journal of Geophysical Research: Space Physics**, v. 105, n. A6, p. 12813–12821, 2000. 96, 102

SOUZA, J. R. **Modelagem ionosférica em baixas latitudes no Brasil.** 182 p. (INPE-6395-TDI/611). Tese (Doutorado em Geofísica Espacial) — Instituto Nacional de Pesquisas Espaciais (INPE), São José dos Campos, 1997. 10, 72

STENING, R. Modelling the low latitude f region. **Journal of Atmospheric and Terrestrial Physics**, v. 54, n. 11-12, p. 1387–1412, 1992. 1

SU, Y.; OYAMA, K.-I.; BAILEY, G.; TAKAHASHI, T.; WATANABE, S. Comparison of satellite electron density and temperature measurements at low latitudes with a plasmasphere-ionosphere model. **Journal of Geophysical Research: Space Physics**, v. 100, n. A8, p. 14591–14604, 1995. 1

TAKAHASHI, H. Signatures of 3–6 day planetary waves in the equatorial mesosphere and ionosphere. **Annales Geophysicae**, v. 24, n. 12, p. 3343–3350, 2006. 121, 123

_____. Ionospheric response to 2-day planetary wave in the equatorial and low latitude regions. **Journal of Atmospheric and Solar-Terrestrial Physics**, v. 90, p. 164–171, 2012. 4, 117

TAKAHASHI, H.; BURITI, R.; GOBBI, D.; BATISTA, P. Equatorial planetary wave signatures observed in mesospheric airglow emissions. **Journal of Atmospheric and Solar-Terrestrial Physics**, v. 64, n. 8-11, p. 1263–1272, 2002. 122

TAKAHASHI, H.; COSTA, S.; OTSUKA, Y.; SHIOKAWA, K.; MONICO, J.; PAULA, E.; NOGUEIRA, P.; DENARDINI, C.; BECKER-GUEDES, F.; WRASSE, C. Diagnostics of equatorial and low latitude ionosphere by tec mapping over brazil. **Advances in Space Research**, v. 54, n. 3, p. 385–394, 2014. 1, 2, 3, 19, 20, 21, 91

_____. _____. **Advances in Space Research**, v. 54, n. 3, p. 385–394, 2014. 123, 124, 126

TAKAHASHI, H.; LIMA, L.; WRASSE, C.; ABDU, M.; BATISTA, I.; GOBBI, D.; BURITI, R.; BATISTA, P. Evidence on 2–4 day oscillations of the equatorial ionosphere hf and mesospheric airglow emissions. **Geophysical Research Letters**, v. 32, n. 12, 2005. 117

TAKAHASHI, H.; WRASSE, C.; OTSUKA, Y.; IVO, A.; GOMES, V.; PAULINO, I.; MEDEIROS, A.; DENARDINI, C.; SANTANNA, N.; SHIOKAWA, K. Plasma bubble monitoring by tec map and 630 nm airglow image. **Journal of Atmospheric and Solar-Terrestrial Physics**, v. 130, p. 151–158, 2015. 43

TAKAHASHI, H.; WRASSE, C. M.; DENARDINI, C. M.; PADUA, M. B.; PAULA, E. R.; COSTA, S. M. A.; OTSUKA, Y.; SHIOKAWA, K.; MONICO, J. F.; IVO, A. Ionospheric tec weather map over south america. **Space Weather**, v. 14, n. 11, p. 937–949, 2016. 3

TAYLOR, J. Characteristics of electric earth-current disturbances, and their origin. **Proceedings of the Royal Society of London**, v. 71, n. 467-476, p. 225–227, 1903. 7

TOBISKA, W. K.; WOODS, T.; EPARVIER, F.; VIERECK, R.; FLOYD, L.; BOUWER, D.; ROTTMAN, G.; WHITE, O. The solar2000 empirical solar irradiance model and forecast tool. **Journal of Atmospheric and Solar-Terrestrial Physics**, v. 62, n. 14, p. 1233–1250, 2000. 73

TORRENCE, C.; COMPO, G. A practical guide to wavelet analysis. **Bulletin of the American Meteorological Society**, v. 78, n. n1, p. 61–78, 1998. 61, 62, 65

_____. _____. **Bulletin of the American Meteorological Society**, v. 78, n. 1, p. 61–78, 1998. Disponível em: <https://paos.colorado.edu/research/wavelets/>. 61

UNNIKRISHNAN, K.; NAIR, R. B.; VENUGOPAL, C. Harmonic analysis and an empirical model for tec over palehua. **Journal of Atmospheric and Solar-Terrestrial Physics**, v. 64, n. 17, p. 1833–1840, 2002. 20

VALLADARES, C.; CHAU, J. The low-latitude ionosphere sensor network: Initial results. **Radio Science**, v. 47, n. 04, p. 1–18, 2012. 113

VENKATESH, K.; FAGUNDES, P.; PRASAD, D.; DENARDINI, C.; ABREU, A.; JESUS, R.; GENDE, M. Day-to-day variability of equatorial electrojet and its role on the day-to-day characteristics of the equatorial ionization anomaly over the indian and brazilian sectors. **Journal of Geophysical Research: Space Physics**, v. 120, n. 10, p. 9117–9131, 2015. 1, 19, 20

WALKER, G. Longitudinal structure of the f-region equatorial anomalya review. **Journal of Atmospheric and Terrestrial Physics**, v. 43, n. 8, p. 763–774, 1981. 1, 2

WALLACE, J. M.; KOUSKY, V. Observational evidence of kelvin waves in the tropical stratosphere. **Journal of Atmospheric Sciences**, v. 25, n. 5, p. 900–907, 1968. 122

WALTERSCHEID, R. Solar cycle effects on the upper atmosphere-implications for satellite drag. **Journal of Spacecraft and Rockets**, v. 26, n. 6, p. 439–444, 1989. 126

WATTHANASANGMECHAI, K.; YAMAMOTO, M.; SAITO, A.; MARUYAMA, T.; YOKOYAMA, T.; NISHIOKA, M.; ISHII, M. Temporal change of eia asymmetry revealed by a beacon receiver network in southeast asia. **Earth, Planets and Space**, v. 67, n. 1, p. 75, 2015. 2, 19, 20

WELLS, H. Effects of solar activity on the ionosphere and radio communications. **Proceedings of the IRE**, v. 31, n. 4, p. 147–157, 1943. 126

YAMAZAKI, Y.; STOLLE, C.; MATZKA, J.; ALKEN, P. Quasi-6-day wave modulation of the equatorial electrojet. **Journal of Geophysical Research: Space Physics**, v. 123, n. 5, p. 4094–4109, 2018. 4, 116, 117

YEH, K.; FRANKE, S. J.; ANDREEVA, E.; KUNITSYN, V. An investigation of motions of the equatorial anomaly crest. **Geophysical Research Letters**, v. 28, n. 24, p. 4517–4520, 2001. 4, 19, 20, 91, 92, 94, 97

YUE, X.; SCHREINER, W. S.; KUO, Y.-H.; LEI, J. Ionosphere equatorial ionization anomaly observed by gps radio occultations during 2006–2014. **Journal of Atmospheric and Solar-Terrestrial Physics**, v. 129, p. 30–40, 2015. 27, 30, 129, 130

ZARRAOA, N.; SARDON, E.; KLAEHN, D.; JUNGSTAND, A. Evaluation of glonass performance in practical applications- comparison with gps-based ionospheric tec values. In: **INTERNATIONAL TECHNICAL MEETING OF THE SATELLITE DIVISION OF THE INSTITUTE OF NAVIGATION, 8.,**. [S.l.: s.n.], 1995. p. 1031–1039. 36

ZHAO, B.; WAN, W.; LIU, L.; REN, Z. Characteristics of the ionospheric total electron content of the equatorial ionization anomaly in the asian-australian region during 1996–2004. **Annales Geophysicae**, v. 27, n. 10, p. 3861–3873, 2009. 2, 19, 20

ZOU, L.; RISHBETH, H.; MÜLLER-WODARG, I.; AYLWARD, A.; MILLWARD, G.; FULLER-ROWELL, T.; IDENDEN, D.; MOFFETT, R. Annual and

semiannual variations in the ionospheric f2-layer modelling. **Annales Geophysicae**, v. 18, n. 8, p. 927–944, 2000. 4, 116

APPENDIX A- ANNUAL VARIABILITY OF EIA

The annual variations of the EIA observed at various magnetic meridian lines between 2014 and 2019 was shown in chapter 4. The yearly variations of EIA at the magnetic meridians 0.22°W, 3.36°E, 11.99°E, and 21.50°E were excluded because they essentially exhibit the same information. These will be provided here.

Figure A.1 - Annual variability of EIA crest at 0.22°W Meridian from 2014 to 2019.
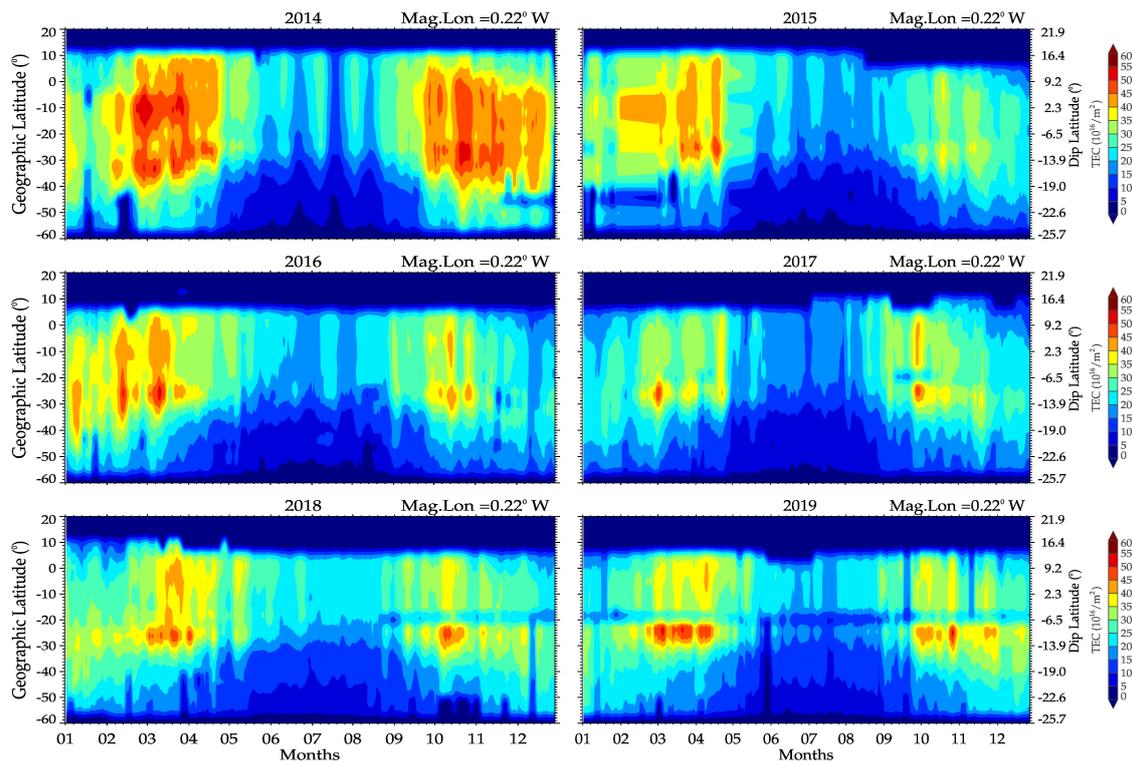
Figure A.2 - Same as Figure A.1 but for Magnetic Meridian 3.36°E sector.
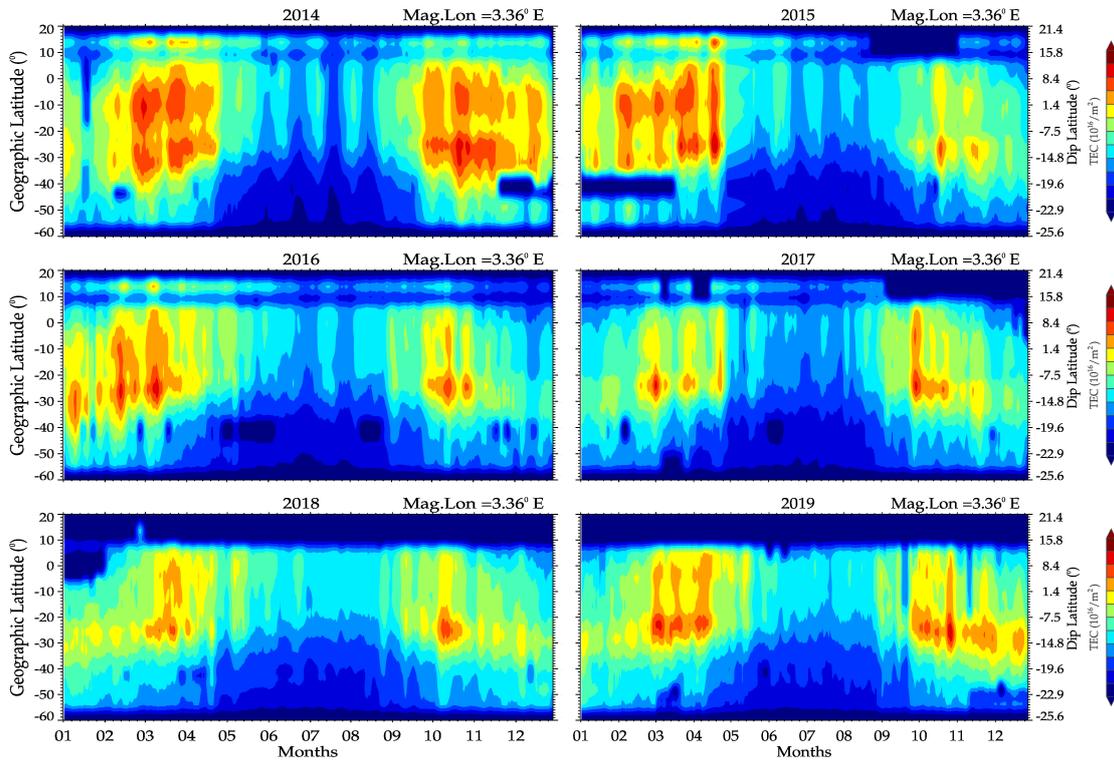
Figure A.3 - Same as Figure A.2 but for Magnetic Meridian 11.99°E sector.
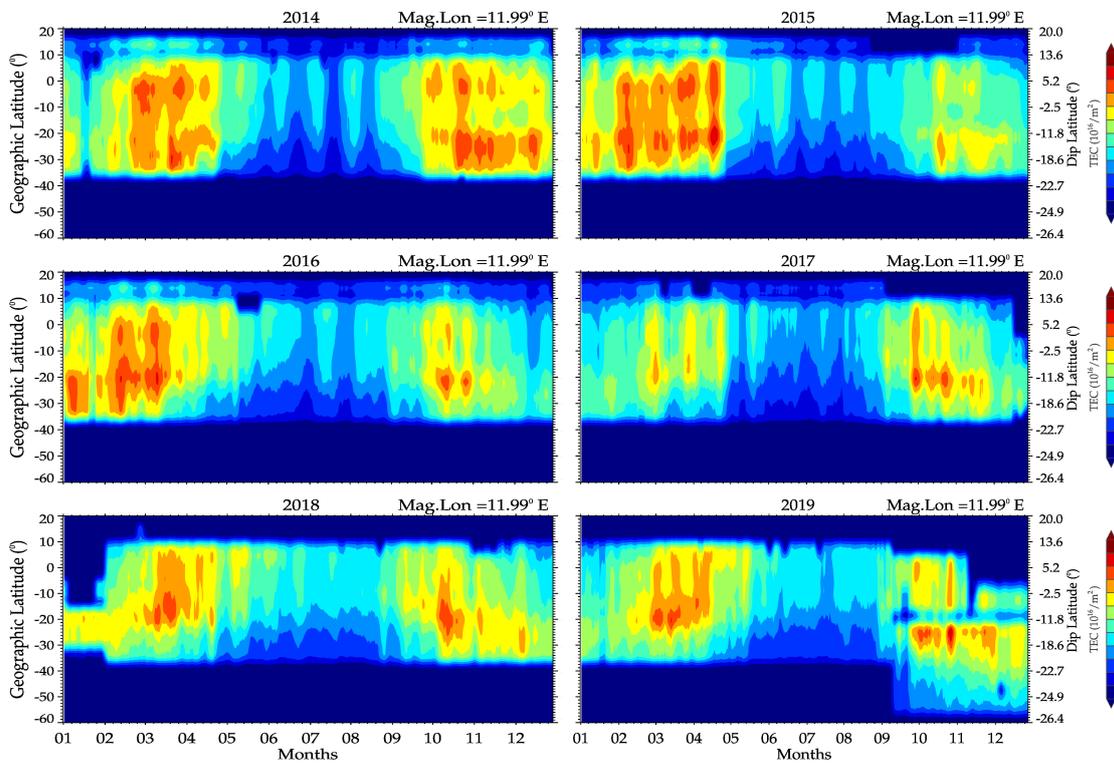
Figure A.4 - Same as Figure A.3 but for Magnetic Meridian 16.61°E sector.
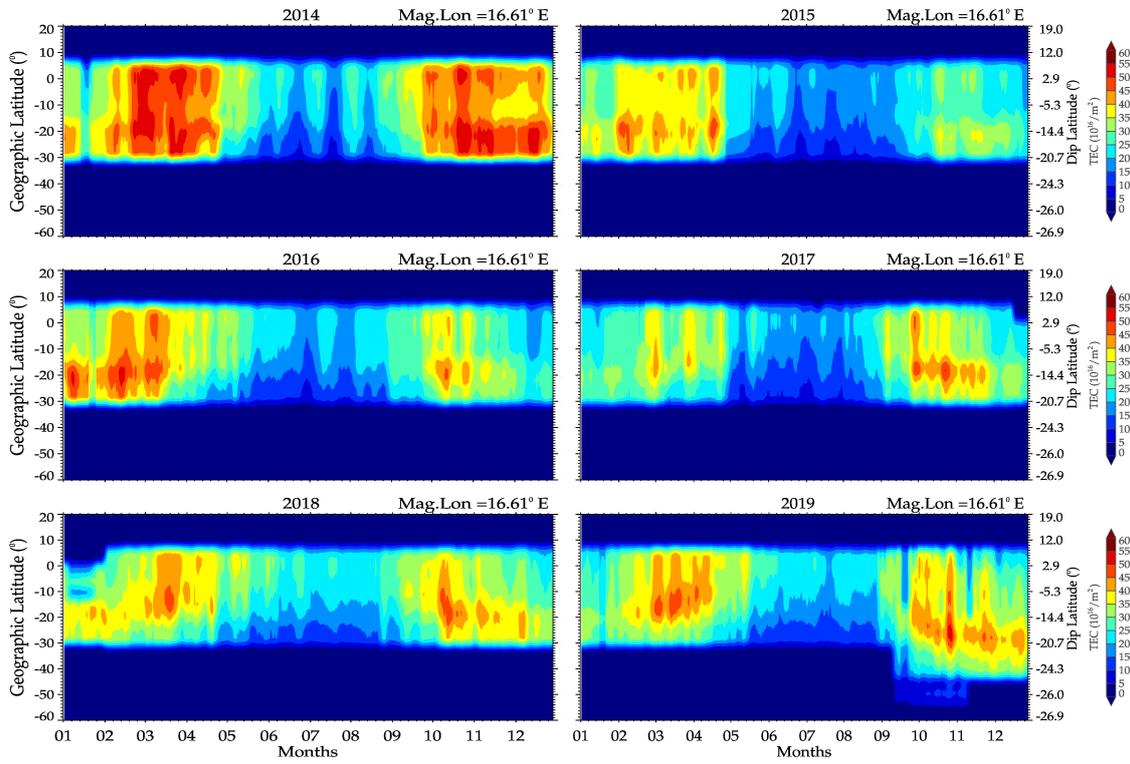
Figure A.5 - Same as Figure A.4 but for Magnetic Meridian 21.50°E sector.
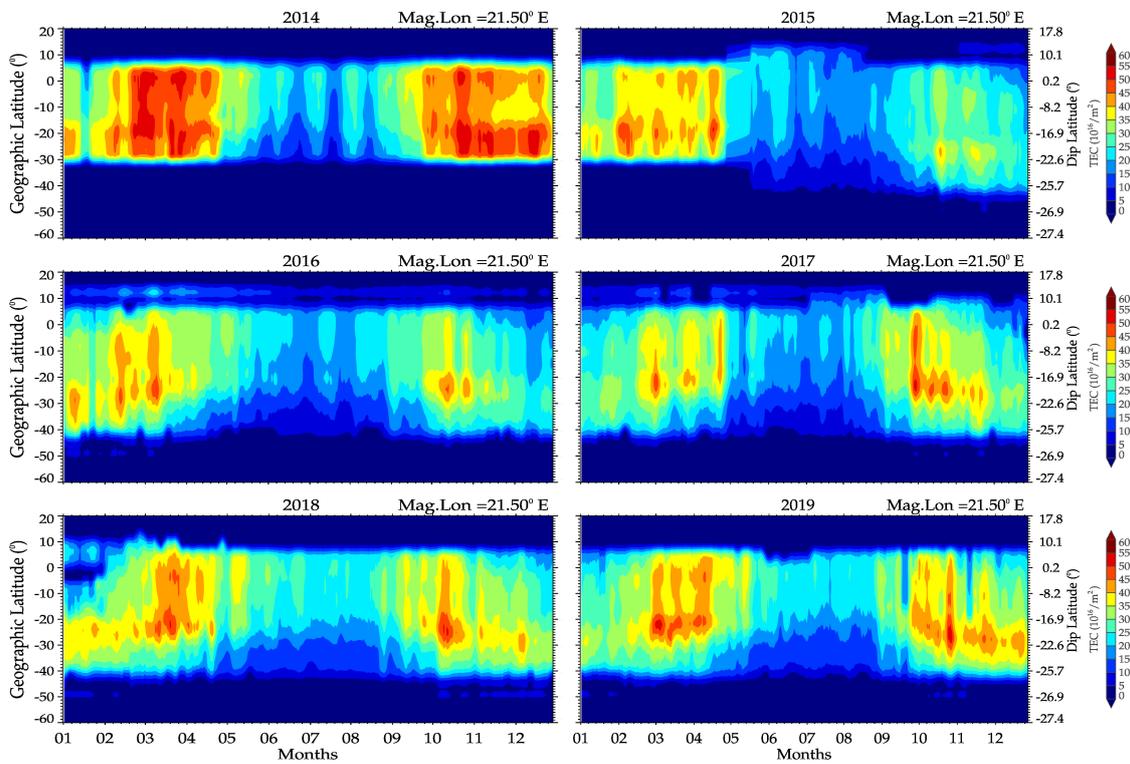
Figure A.6 - Same as Figure A.5 but for Magnetic Meridian 26.70°E sector.
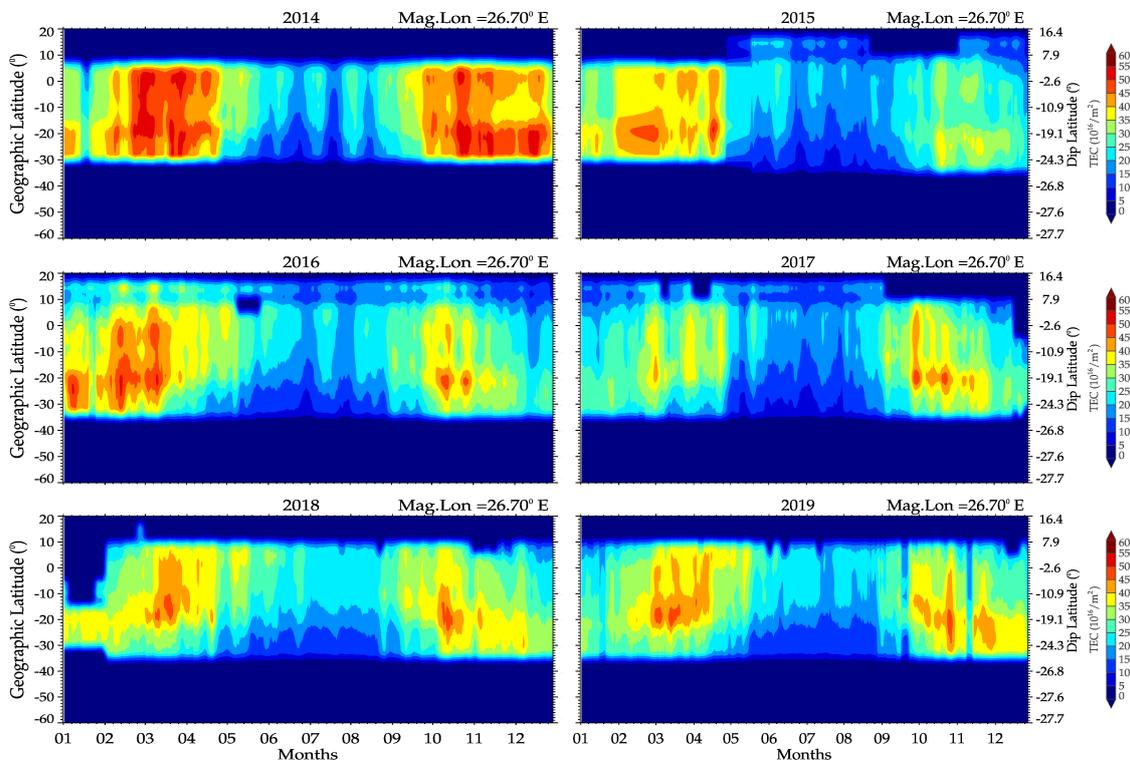
PUBLICAÇÕES TÉCNICO-CIENTÍFICAS EDITADAS PELO INPE

Teses e Dissertações (TDI)

Teses e Dissertações apresentadas nos Cursos de Pós-Graduação do INPE.

Notas Técnico-Científicas (NTC)

Incluem resultados preliminares de pesquisa, descrição de equipamentos, descrição e ou documentação de programas de computador, descrição de sistemas e experimentos, apresentação de testes, dados, atlas, e documentação de projetos de engenharia.

Propostas e Relatórios de Projetos (PRP)

São propostas de projetos técnico-científicos e relatórios de acompanhamento de projetos, atividades e convênios.

Publicações Seriadas

São os seriados técnico-científicos: boletins, periódicos, anuários e anais de eventos (simpósios e congressos). Constam destas publicações o Internacional Standard Serial Number (ISSN), que é um código único e definitivo para identificação de títulos de seriados.

Pré-publicações (PRE)

Todos os artigos publicados em periódicos, anais e como capítulos de livros.

Manuais Técnicos (MAN)

São publicações de caráter técnico que incluem normas, procedimentos, instruções e orientações.

Relatórios de Pesquisa (RPQ)

Reportam resultados ou progressos de pesquisas tanto de natureza técnica quanto científica, cujo nível seja compatível com o de uma publicação em periódico nacional ou internacional.

Publicações Didáticas (PUD)

Incluem apostilas, notas de aula e manuais didáticos.

Programas de Computador (PDC)

São a seqüência de instruções ou códigos, expressos em uma linguagem de programação compilada ou interpretada, a ser executada por um computador para alcançar um determinado objetivo. Aceitam-se tanto programas fonte quanto os executáveis.